Role Of Structure In Magnetic And Topological Transitions

A thesis submitted for the degree of
Doctor of Philosophy (Science)
in
Physics (Theoretical)
by

Prasun Boyal

Department of Physics
University of Calcutta
2024

To my parents, for this thesis is a testament to your sacrifices.

Acknowledgements

I would like to express my sincere gratitude to my supervisor, Prof. Priya Mahadevan, for her invaluable guidance and support throughout my PhD journey. Her expertise was instrumental in shaping my thesis and ensuring its quality. She consistently provided insightful feedback, encouraged me to challenge my assumptions, and taught me ask sharp questions regarding my research. I am particularly grateful to her for being patient with me and allowing me to choose my projects and helping me with personal situations. This thesis would not have been possible without her dedicated mentorship. I also thank Prof. D D Sarma for his valuable inputs in different projects carried out in this thesis. I would also take this opportunity to thank my thesis committee members Prof. Manoranjan Kumar and Atin Pal and Bhavtosh Bansal for their valuable feedback and fruitful discussions.

I consider myself lucky to be able to learn from Dr. Poonam Kumari, who had given special effort to make sure that I become thoroughly familiar with different techniques that are to be later used in this thesis. I acknowledge fruitful discussions with other seniors group members Sisir Kumar Pandey, Sagar Sarkar, Sumanti Patra and Joydeep Chatterjee. I also thank my colleague and juniors within the group Debayan Mondal, Shivam Mishra, Krishnendu Patra, Shinjini Paul, Sanuja Khuntia, Shivam Jani, Madhurita Das and Maitrayee Barman for making themselves available for discussion on various topics and helping me with different academic and administrative works. I also acknowledge the help from post doctoral fellows and project students Deepika Srivastava, Surinder Kumar, Komal Singh, K.P. Athira, Priyanka Garg, Sanjukta Paul, Vijoy N and Gargee Bhattacharyya. A special appreciation is in order for Krishnendu Patra for being the partner in coding for years and helping me connect to my desktop remotely during Covid pandemic, an matter of utmost importance for completion of my work.

Spending almost 6 years in SNBNCBS would not have been possible without the warm company of my friends with whom I had the pleasure of sharing office space. In this regard, a sincere gratitude is due towards Premashish Kumar, Tanmoy Chakraborty, Krishnendu Sinha, Dibyendu Maity, Susmita Changdar, Amit Kumawat and Shobhan Dev Mondal. I thank Premashish for being the constant source of trivia on both professional and general affairs. He ensured that I remain updated about the contemporary events while being busy with my work. His attitude towards solving an scientific problem has been a constant source of perseverance for me. Tanmoy deserves a special thanks for his help with learning

different simulation techniques. Krishnendu and Dibyendu made themselves available for any technical problem regarding Linux operating system. I also thank my collaborators, Prof. Atin Pal, Rafiqul Alam, Prof. Prabhat Mondal, Afsar Ahmed and Prof. Indranil Das for their feedback and allowing me to work independently in their projects.

Finally, I am grateful to my parents for their immense struggle to make me a physicist. Without their countless sacrifices and determination I would never be able to continue this long journey. Looking back now, It was their smiling faces in the face of adverse situations, that kept me going during this long journey. I also remember my late Uncle and late grand father for giving me the courage to start the journey of being a researcher. I also thank my paternal grandmother for her constant support both financially and mentally that helped me going. This acknowledgement would be incomplete without mentioning my maternal grandparents who had taught me the value of simplicity in life, a remarkable lesson helping me through different situations in life. I also thank my wife Ananya for being the constant motivator and not letting me procrastinate with the thesis. She made the writing process faster by making many of the figures and tables included in this thesis. I must also thank her for agreeing to be the unpaid proofreader.

Last but not the least, a cordial thanks to all the caffeine that kept me wake to finish the writing!

Abstract

Classification of different materials depending on their electronic and magnetic properties has always been the central task in material science. Recent developments suggest a new classification scheme depending on some topological invariants that can be defined for a particular electronic structure in connection with the underlying crystal symmetries. In this thesis, using both *ab initio* calculation and model Hamiltonian, the role of the structure in 2D, layered quasi 2D and 3D crystals on their electronic and magnetic properties have been studied. The monolayer Mo and W based transition metal dichalcogenides have been studied in various structural configuration. In the most stable 1H polymorph, these are direct bandgap semiconductors where the gap is believed to be between d orbitals of the metal, originating from crystal field effects. However, our calculation shows that the indirect hopping via p states plays a very crucial role in opening the insulating gap. Next, the 1T and 1T' phase of these material have been studied. The instability in the 1T phase has been understood as the competition between direct and indirect hopping of d electrons, and it has demonstrated how the structural distortions make the 1T' phase a topologically non-trivial quantum spin hall insulator. Next, moving onto, a semi-Dirac metal, $LaAgSb_2$, we have shown that the material has a potentially exfoliable layered structure at high temperature. We have find that due to the onset of charge density wave, the material becomes chiral in low temperature. This structural difference further explains the sign reversal of the planer hall signal as measured in the experiments for this material. Next, moving onto 3D materials, the metal insulator transitions and its connection the magnetic ordering in $NaOsO_3$ has been studied. Using pressure to tune the structure, it is shown that the G type anti-ferromagnetism in $NaOsO_3$ is very robust and thereby making the pressure coefficient of the bandgap small by order of magnitude than other materials. It is also found that the long range antiferromagnetic ordering is much more robust and survives deep into the metallic phase. The unusual magneto-electric transport in the doped Heusler material $Ru_2Fe_{0.6}Mn_{0.4}Ge$. By performing *ab-initio* calculations, canted magnetic ground states was found where the moment on the Mn atoms makes 165° angle with the moment on the Fe atoms. Further, the anomalous hall conductivity has been calculated which matches well with experiments.

List of Publication

1. Detection of Nontrivial Topology Driven by Charge Density Wave in a Semi-Dirac Metal.
   R. Alam*, P. Boyal*, S. Roy, R. Singha, B. Pal, R. Pal, P. Mandal, P. Mahadevan, A. N. Pal
   Adv. Funct. Mater. 2023, 33, 2306751.
   * *equal contribution*

2. Electric field induced metal semiconductor transitions in twisted bilayers of WSe_2
   Sumanti Patra, Prasun Boyal, and Priya Mahadevan
   Phys. Rev. B 107, L041104

Manuscript under Preparation

- "Robust antiferromagnetic ordering under pressure in a Slater insulator" (with Priya Mahadevan).
- "Topological insulating phase in 1T′ MX_2(M=Mo,W;X=S,Se,Te) revisited" (with Poonam Kumari and Priya Mahadevan)
- "Role of indirect hopping via chalcogen p states on the insulating gap of Mo and W based TMDCs in hexagonal polymorph." (with Priya Mahadevan).

Contents

List of Figures

List of Tables

Part I

Preliminaries

CHAPTER 1

Introduction

"Not only the universe is stranger than we think, It is stranger than we can think"

Werner Heisenberg

1.1 Historical Perspective

The physical properties of materials have been a topic of scientific inquiry for centuries. The nature of these studies had gone through a significant transition from being empirical and phenomenological to becoming more fundamental and microscopic since the middle of the last century as the understanding of the interactions between constituent particles became clearer with the advancement of quantum mechanics. These solids are formed from densely packed atoms, in which the valence electrons of these atoms interacts strongly among them. Depending on the constituent elements and the conditions in which the solids form, different geometric arrangement of the atoms, called crystals, are possible. The crystal structure heavily influences different properties of materials by dictating the interactions between electrons. With further development of various experimental techniques to study these crystals, like electron diffraction, neutron diffraction, x-ray crystallography etc., the basic understand-

ing of mechanical, thermal, electronic, optical, magnetic properties becomes more lucid.

Another crucial aspect that influences the properties of solids is the size of the crystal structure. Crystals, which are periodic in all three directions are conventional 3D materials, while if the size of the crystal is confined in one direction the resulting materials have sheet like structure with periodicity in two directions and called 2D materials. Similarly, restricting the crystal in two direction, one obtain ribbon like 1D materials. Even, zero dimensional material can exist where the size of the material is in the 1-100 nanometer range. Quantum dots, nanoparticles, fullerene, etc. are few examples of such 0D materials. Historically, application of three dimensional (3D) materials with various electronic and magnetic properties in different types of devices had started much earlier than flat two dimensional (2D) materials. This is because more than ninety years ago, Peierls[1] and Landau[2] argued that completely flat two dimensional (2D) crystals are not thermodynamically stable and therefore would not exist in any finite temperature. It was proved that thermal fluctuations in these low dimensional lattices must have a divergent part that leads to displacements of atoms comparable to interatomic distances at any finite temperature[3]. Mermin extended these analysis [4] and put the ideas into solid footing. A series of experimental observations following these analysis strongly supported the impossibility of completely flat 2D lattices. Therefore, for a long time, 2D materials were considered to be limiting part of larger 3D structures, usually grown epitaxially on top of some single crystals matching lattice parameters [5, 6].

However, 2D materials had been an integral part of theoretical studies for a long time [7, 8, 9]. For example, it was found that

graphene, a 2D monolayer of closely packed carbon atoms could be a building block of different dimensional material. Graphene sheet could be wrapped into 0D fullerene, rolled into 1D nanotube or stacked into 3D graphite [10]. Therefore these honeycomb lattices had been studied theoretically and widely used for describing properties of other geometric structures. In the eighties, it was shown that the 2D honeycomb lattice provides a condensed matter analogue of 2+1 dimensional quantum electrodynamics [11, 12, 13]. The possibility of massless Dirac electrons within these honeycomb lattice led scientists to use it as a toy model to demonstrate new interesting physics which had so far been unnoticed in the conventional 3D materials. However, due to the absence of material realization of 2D lattices, these had been termed as merely "academic materials"[12].

The scenario changed drastically after the discovery of free standing Graphene by Scotch tape method[14]. Since then a bunch of atomically thin 2D materials have been isolated [15] from bulk crystal as other techniques to isolate monolayers from bulk materials like chemical vapor deposition, epitaxial growth and mechanical exfoliation methods developed.Consequently, the rich physics of low dimensional electron system became reality and a new era had begun where these newly found 2D materials paved the way to manipulate spin and orbital moment of electrons in an unprecedented way. This is particularly interesting as these new exotic properties results from the 2D crystal structure while the constituent elements remained the same.

Although graphene have attracted lot of interest, lack of bandgap in graphene made researchers look for other semiconducting 2D material. Transition metal dichalcogenides (TMDCs), which are of the type MX_2, where M is a transition metal atom (such as Mo or W)

and X is a chalcogen atom (such as S, Se or Te), provided a promising alternative. While having atomic scale thickness comparable to graphene, these materials also have direct bandgap making them useful for semiconductor application. This, along with their strong spin-orbit coupling and favorable electronic and mechanical properties, makes them ideal candidates for both scientific exploration and next-generation electronics. Additionally, intriguing phenomena like charge density waves, superconductivity, and topological phases have been observed within different members of this class of materials. Moreover, these materials can exist in multiple structural forms, leading to diverse electronic behaviors even within the same material. This versatility opens the door for further innovation in device design.

The central aim of this thesis is to understand how different electronic, topological and magnetic properties arise in materials with different crystal structure but similar constituent elements. We have studied different materials with both two and three dimensional crystals and identified the crucial role played by the crystal structure in determining their ground states properties. In the following sections, these materials with their interesting properties are discussed briefly.

1.2 Physics of Mo and W based TMDCs

In this thesis, the 2D materials studied, belongs to the family of Mo or W based TMDCs. These materials had a very long and fruitful history of their own. Their bulk structure was first determined long back by Linus Pauling in 1923 [16]. They were found to be layered materials where successive layers were stacked with weak Van der Waals forces. By the late 1960s, around 60 TMDCs were known, at least 40 of them with a layered structure[17]. The first reports on

the use of adhesive tapes for producing ultra thin MoS_2 layers, by Robert Frindt [18], dated back to 1963, and the production of suspended single layer MoS_2 were first achieved in 1986 [19]. However, as mentioned before, with the discovery of graphene, study of these materials saw an upsurge and many interesting properties involving spin and orbital degree of freedom had been found since then.

1.2.1 Spin Valley Coupling

The properties of the monolayers of these material changes drastically from the bulk crystals. A prototypical member of this class of material, MoS_2, is an indirect bandgap semiconductor in the bulk, while the hexagonal polymorphic monolayer (1H) is a direct bandgap material with the gap falling in the visible spectrum range making it suitable for optoelectronic devices. In monolayer MoS_2, the conduction band minimum and valence band maximum are at the corner of the hexagonal 2D Brillouin zone, known as K points [20, 21, 22]. Like graphene, the low energy carriers in these materials can also have binary index due to two inequivalent valleys at K and -K. The valley index is expected to be robust against scattering due to long wave length phonon or smooth deformation.

1H MoS_2 differs from graphene in two crucial aspects. Firstly, the inversion symmetry is explicitly broken in the monolayer MoS_2, which is otherwise present in graphene, or even in the bulk structure of MoS_2 as shown in Fig. 1.1a. Consequently, the valley Hall effect, which has earlier been shown to arise in a graphene like lattice with staggered potential [24], was also expected to be present in 1H MoS_2. Additionally, broken inversion symmetry also causes valley dependent optical selection rules for inter band transitions at K points [25]. Secondly, unlike graphene MoS_2 has a strong spin orbit coupling (SOC) due to the d orbitals of the transition metal

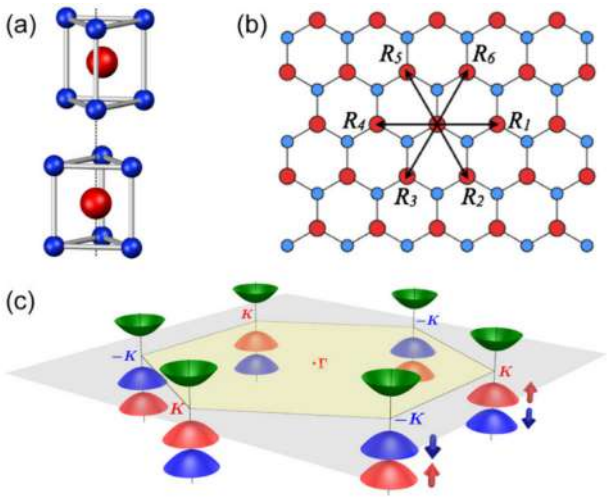

Figure 1.1: (a) Inversion symmetry in 2H bulk MoS_2 with two units of monolayer MoS_2 each lacking point of inversion individually. (b) MoS_2 monolayer viewed from c direction with the nearest neighbor Mo atoms indicated by connecting vectors, R_i (c) Schematic spin spilt VBM and CBM at K and -K. [Reproduced from [23]]

atoms. This provides a platform to study spin physics and make this material suitable for spintronics applications.

Using these ideas, Di Xiao et. al [23] have shown that 1H MoS_2 and other group VI dichalcogenides provide a platform to study coupled spin valley physics. It was shown that the conduction and valence band at K points are well described by massive Dirac fermions and time reversal symmetry invokes that the spin splitting at different valleys must be opposite (see Fig. 1.1c). Additionally, for these materials the valence band exhibit strong spin valley coupling leading to several major outcomes. First, the valley Hall effect arises in addition to a spin Hall effect for both electron and hole doping [26, 27, 28, 29]. Second, due to the valley contrasting spin splitting of the valence band, one finds long spin and valley lifetimes both in the bulk and on the boundary as the flip of individual index alone is prohibited. Third, the optical selection rules depends on both valley

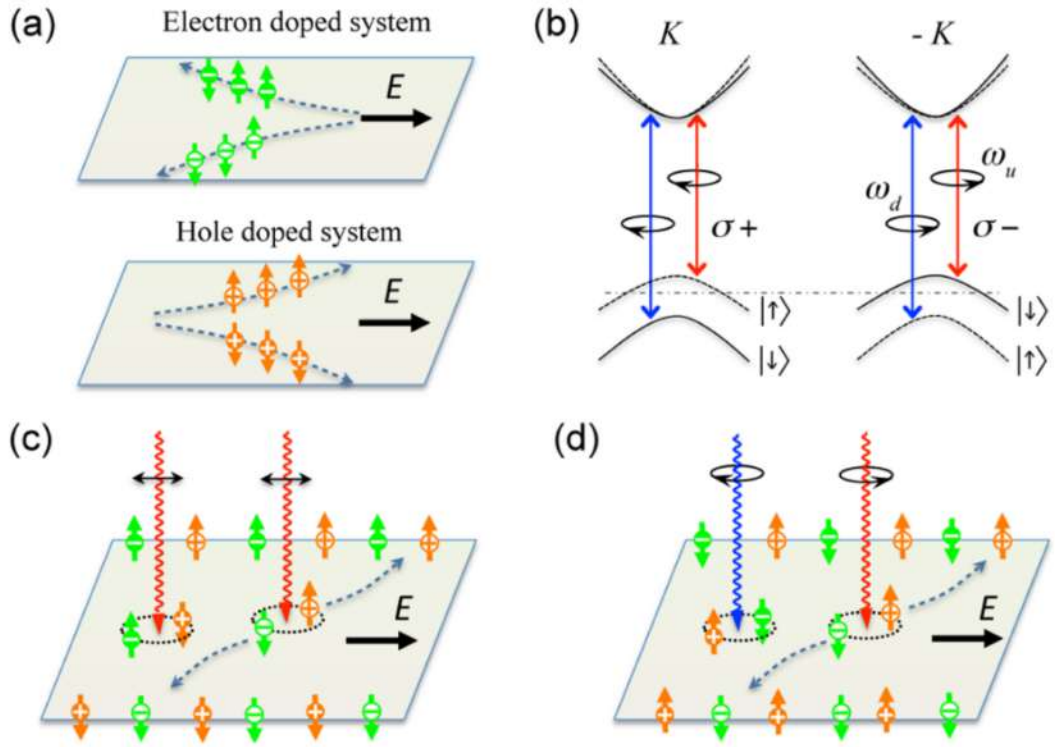

Figure 1.2: Coupled spin and valley physics in monolayer group VI dichalcogenides. The electrons and holes in valley K are denoted by white '-' and '+' symbol respectively in dark circles and their counterparts in valley -K are denoted by inverse color. (a) Schematic of valley and spin Hall effects in electron and hole-doped systems. (b) Valley and spin optical transition selection rules. ω_u and ω_d are, respectively, the transition frequencies from the two split valence-band tops to the conduction band bottom. (c) Spin and valley Hall effects of electrons and holes excited by linearly polarized optical field with frequency ω_u. (d) Spin and valley Hall effects of electrons and holes excited by two-color optical fields with frequencies ω_u and ω_d and opposite circular polarization. [Reproduced from [23]]

and spin index. As a result low energy carriers with different spin and valley indices can be selectively excited by optical fields of different frequencies and circular polarization (see Fig. 1.2). These unique effects suggest that group VI dichalcogenides have great potential in integrated valleytronic and spintronic applications.

1.2.2 Orbital Hall Effect

Historically, the first theoretical study of orbital Hall effect (OHE) was performed on 3D metals [30, 31, 32], by focusing on how orbital texture in different materials respond to applied electric field [33, 34, 35]. Later, signatures of OHE have been demonstrated by experimental measurements of orbital torque [36, 37]. Additionally, direct measurement of OHE [38] in recent times allows for rapid development of the field of orbitronics [39, 40, 41]

Although, the study of modern orbital physics started with 3D metals, later on 2D materials have become a promising platform to study various physical phenomena related to orbital moment [42, 43, 44, 45, 46, 47]. Nontrivial orbital texture giving rise to OHE has been shown to exist in many 2D multiorbital materials both theoretically [48, 49, 50, 51] and experimentally [52, 53].

Within various 2D materials, the family of group-VI dichalcogenides in their hexagonal polymorph has attracted particular interest. In these materials, the orbital angular moment can be described well by the low energy states near the K valleys. Additionally, strong OHE had been shown to exist [42, 54, 55] inside the insulating gap [49, 50] along with the possibility of an well defined orbital Chern number [56].

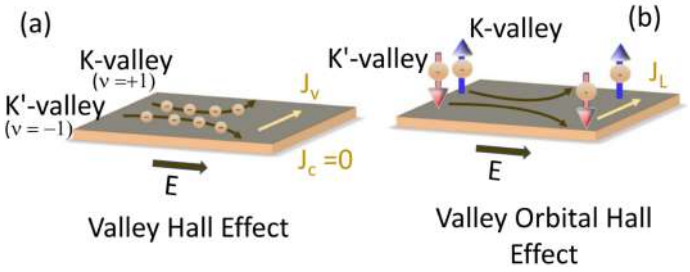

Figure 1.3: (a) valley and (b) valley-orbital Hall effect. The larger arrows denote the component of the orbital moment m_z. The flow of electrons with contrasting valley indices and opposite orbital angular momenta has been shown. Net transverse charge current, $J_c = 0$ but the orbital angular momentum current J_L is finite for the intrinsic system. [Reproduced from [57]]

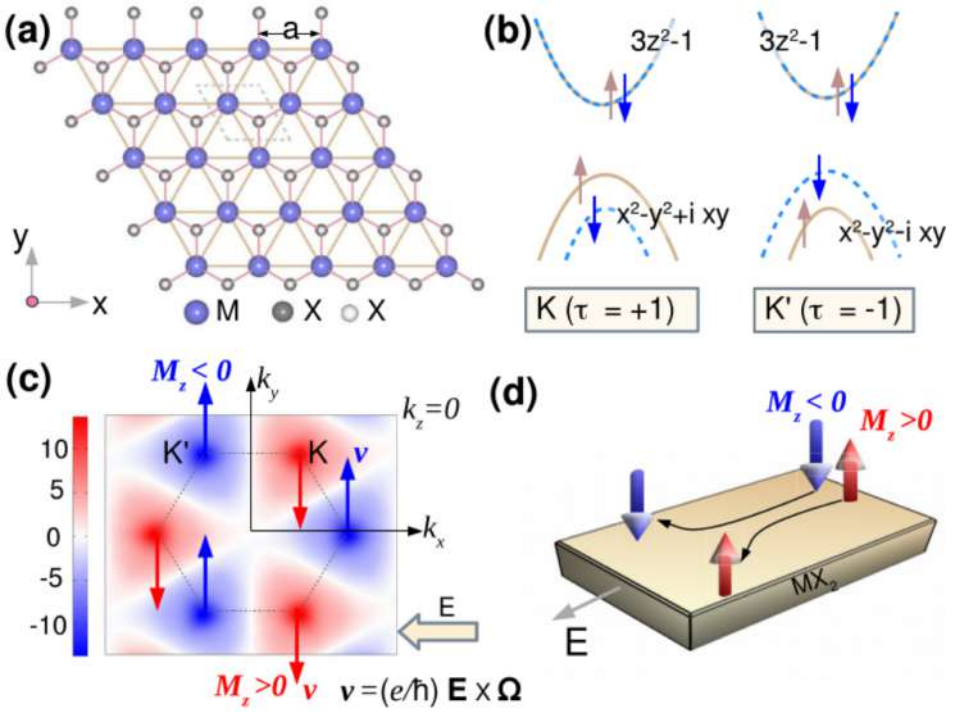

Figure 1.4: Illustration of OHE in monolayer MX_2. (a) Crystal structure (b) The valley coupled spin and orbital characters depicted in the band structure. (c) The orbital moment and the anomalous velocity originating from Berry curvature 2Din the Brillouin zone (d) Transverse flow of orbital moments gives rise to OHE. [Reproduced from [54]]

It was further shown that non-centrosymmetric monolayer TMDCs, gives rise to robust intrinsic orbital moment in the momentum space even in the absence of spin orbit coupling [55]. Calculation of orbital Berry curvature within an effective $k \cdot p$ Hamiltonian has revealed a large orbital Hall conductivity. Additionally, tuning of orbital Hall conductivity is possible by applying a transverse electric field [58, 59], which make these material suitable for direct experimental observation of OHE.

1.2.3 Why study 1H TMDCs again?

Both the spin-valley coupling and OHE in the monolayers of Mo and W based TMDCs have so far been described by an effective Hamiltonian constructed only with the d bands of the transition metal (see Fig. 1.1b and Fig. 1.4a) as described before. These effective Hamiltonian describe the low energy carriers only in the K and K' valleys. However, as the valence band edge at Γ point being energetically very close to the VBM at K point, it is naturally expected that description of low energy excitation will require a full understanding of the band gap throughout the Brillouin zone. Several attempts have been made, where seperate model Hamiltonians have been constructed to describe the low energy bands at different high symmetry points separately or third neighbor interactions between transition metal d states have been taken into consideration [60] to obtain a tight binding model to describe the dispersion of low energy bands throughout the Brillouin zone. However, these models do not clearly explain another complexity seen in these material which is the orbital character reversal of valence and conduction band between K and Γ point.

In our work, taking MoS_2 as a prototypical example of this class of materials, we have shown that constructing any model Hamiltonian

with only d states cannot describe the insulating gap in these materials. Further, we have identified the importance of the hopping of d electrons via chalcogen p states at different k points. As a result a minimal tight binding Hamiltonian has been constructed with relevant d and p orbitals which capture both the insulating gap and the orbital character reversal of valence and conduction band between K and Γ point.

1.3 Topology in Condensed Matter Physics

In the 1980s, discovery of integer [61] and fractional [62] quantum Hall effects initiated a new paradigm of theoretical studies involving the geometric phase of electronic wave functions, which was otherwise considered to be irrelevant for the previous seventy years. The quantum Hall effect was seen in two dimensional electron gas on application of large perpendicular magnetic field. At large fields, bulk electrons form closed cyclotron orbits, while electrons near the boundary move through open orbits as shown in Fig. 1.5b. At low temperatures, as quantum effects become important, the bulk turns into an insulator due to the localisation of closed orbits while the open orbits along the edges produce extended one dimensional channels with a quantized conductance of $\frac{e^2}{h}$.

Although the bulk of the material in quantum Hall states was found to be a featureless insulator, different values of the Hall conductance were found to correspond to adiabatically disconnected ground states. Surprisingly, the quantization of the Hall conductance was found to be extremely robust under disorder. Later these two features became the defining property of topological quantum matter in which the bulk of the material is insulating while gapless boundary states are protected against perturbation. In the absence of local order

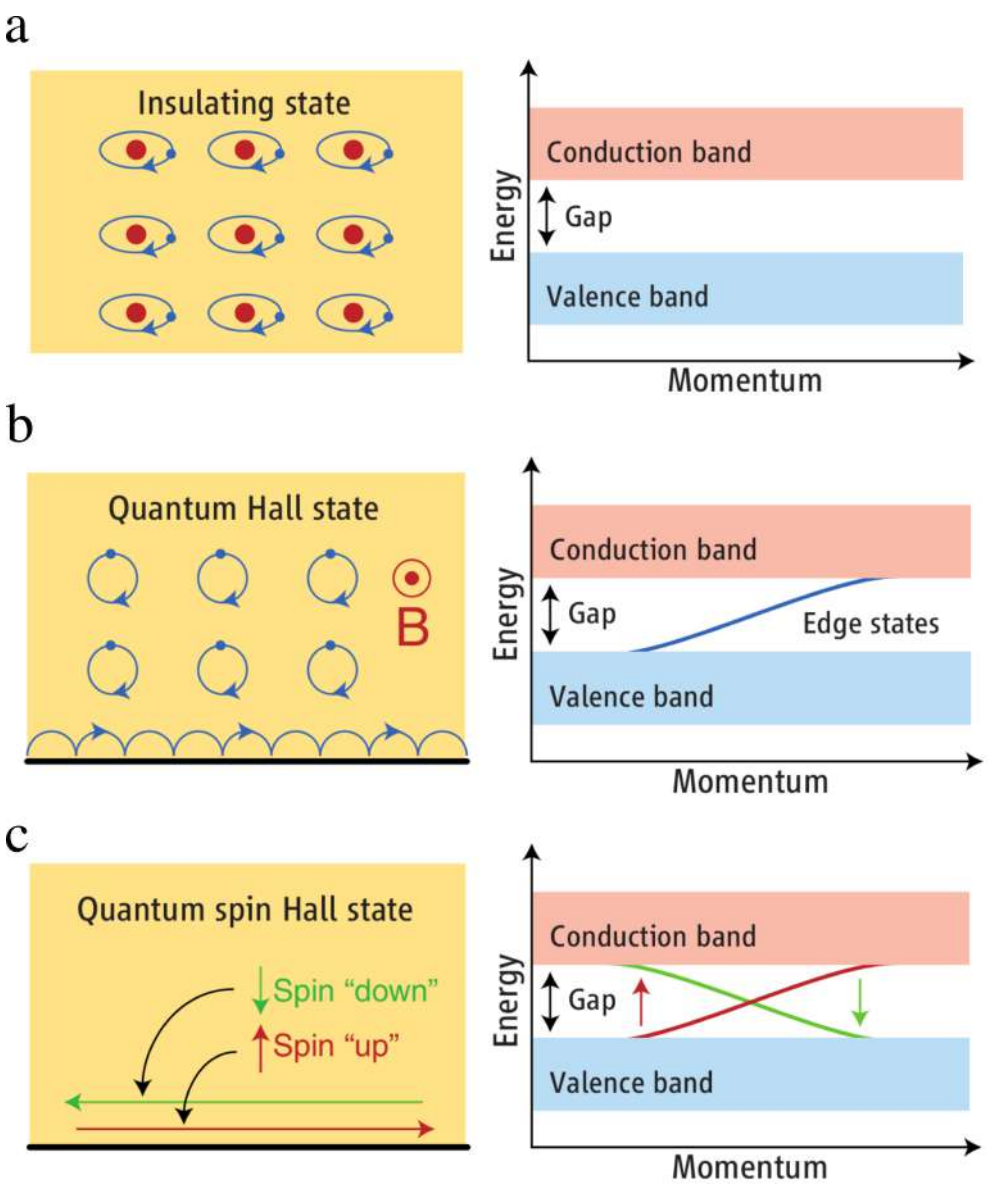

Figure 1.5: (a) Trivial atomic insulator where electrons are bound in localized orbitals (left) and have an energy gap (right) that isolate the filled valence band from the vacant conduction band. (b) A two-dimensional quantum Hall state. The bulk behaves likes insulator while the skipped orbit along the edge allows one way charge conduction in the presence of magnetic field. (c) The quantum spin Hall state at zero magnetic field. The bulk have energy gap while edge states allow spin filtered conduction. [reproduced from [63]]

parameter, this new phase of materials are characterized by global topological invariant like TKNN invariant [64] or Chern number [65].

Around 2005, a new topological state, namely quantum spin Hall (QSH) insulating phase were predicted theoretically [66, 67] and then discovered experimentally in HgTe quantum wells [68]. These new states have some qualitative differences from the above mentioned quantum Hall states. The spin Hall effect can be understood as a transverse spin current flow in response to an electric field. Unlike, quantum Hall states that breaks time reversal symmetry due to applied magnetic field, QSH state does not require magnetic field and therefore does not break time reversal symmetry. From this perspective, the QSH phase can be thought as two replica of the quantum Hall state with opposite Hall conductance where the role of the magnetic field in quantum Hall state is played by the spin orbit coupling in the QSH phase.

However, as the transverse charge conductance is zero in QSH insulator, the TKNN or Chern number mentioned above, does not classify QSH state. It was shown that the proper topological invariant number can take only two values, zero or one, where zero correspond to trivial state while one corresponds to topologically nontrivial QSH insulator [69, 70]. This topological invariant, called Z_2, physically describes number of gapless edge states modulo two.

1.3.1 Topological Insulating Phase in TMDCs

Mo and W based TMDCs in their distorted octahedral polymorphic structure, namely 1T' phase, are example of the QSH phase discussed above. Qian et al. [71] predicted that all six material belonging to this class are large gap QSH insulator. It was found that at the Γ point of the 2D Brillouin zone, the chalcogen p states contribute

to the CBM while the VBM is contributed by the metal d states. Additionally, in the vicinity of the Γ, a linear crossing between VBM and CBM occurs. Strong spin orbit interactions of the d electrons of the metal opens up a fundamental bulk gap at the crossing point. Slab calculation have revealed gapless edge states and consequently a Dirac cone protected by time reversal symmetry is found to be in between the fundamental gap (See Fig. 1.6).

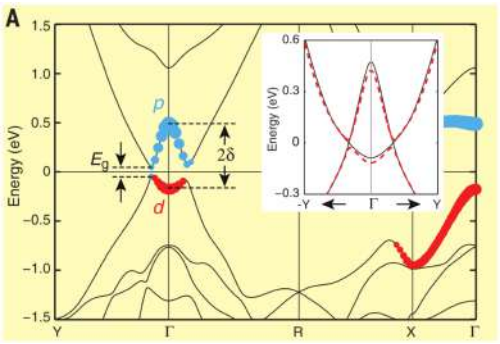

Figure 1.6: Band structure of 1T' MoS_2. The fundamental gap is E_g and the inverted gap is 2δ. The inset shows that spin orbit coupling opens the fundamental gap.(Reproduced from [71])

In our work, we have understood the origin of the unusual inverted gap between chalcogen p and metal d states and showed that this reversal is a common feature in various polymorphs. We have then studied the unstable 1T polymorph and discussed why it readily distorts into the 1T' phase. Then studying the electronic band structures in various polymorphs, we have understood why 1H and 1T polymorphs are not QSH insulators in spite of having inverted chalcogen p and metal d bands at Γ point. Additionally, the origin of insulating bulk and nontrivial Z_2 state in the 1T' phase have been understood by correlating the changes in the electronic band structure with the structural distortions as these materials distort from 1T to 1T' polymorph.

1.4 Topological States in Quasi 2D Materials

Topological quantum state in quasi 2D materials is an emerging field in recent times [72]. Quasi two dimensional can be fabricated in various ways. Thin films of conventional 3D materials, trapped electron gas at the interface of metal oxide semiconductors or electrons within a semiconducting quantum well could considered as examples of quasi two dimensional systems. However, recently another class of material, namely square net materials, have emerged as a suitable quasi two dimensional materials to study a different type of non trivial topology, namely topological semi metal (TSM) [73]. These materials as the name suggests are formed by stacking square networks of transition metal or main group elements with large rare earth element intercalated between these networks. The square networks, referred to as the 4^4 net in crystallography literature [74], are side centered meaning that they contain two atoms per unit cell like graphene.

The quasi 2D nature of these materials can be described in terms of a tolerance factor (t) [75], defined to be the ratio of smallest distance between two atoms within the network and the smallest distance between rare earth element to the network (see Fig. 1.7). Then for $t < 1$, the two dimensional square networks can be considered as isolated layers and the system can be described as quasi-2D material while for $t > 1$ the material becomes three dimensional.

The interest in these square net materials is in the fact that they feature hypervalent bonds causing half filled band as the s and p_z bands will be filled while the in plane p_x and p_y bands are unfilled. Additionally, the in plane p orbitals are forced to be degenerate at different high symmetry points . It was shown that these features in combination with the fact that the square network contains two

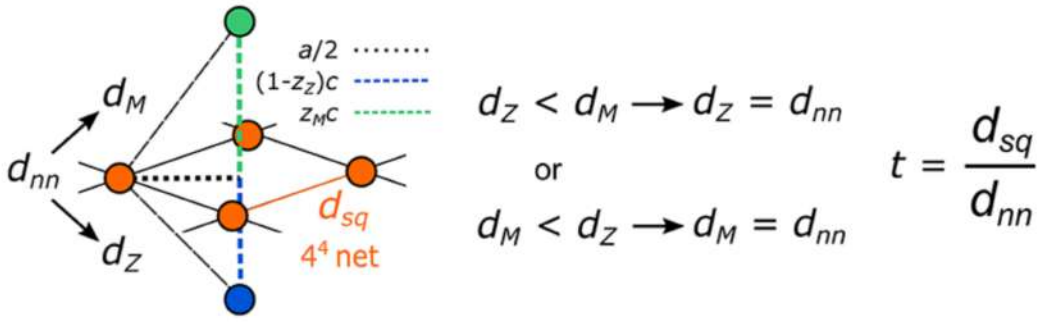

Figure 1.7: Schematic representation of the tolerance factor, $t = d_{sq}/d_{nn}$ and the definition of d_{nn} as the smaller of the two distances d_M and d_Z (Reproduced from [75])

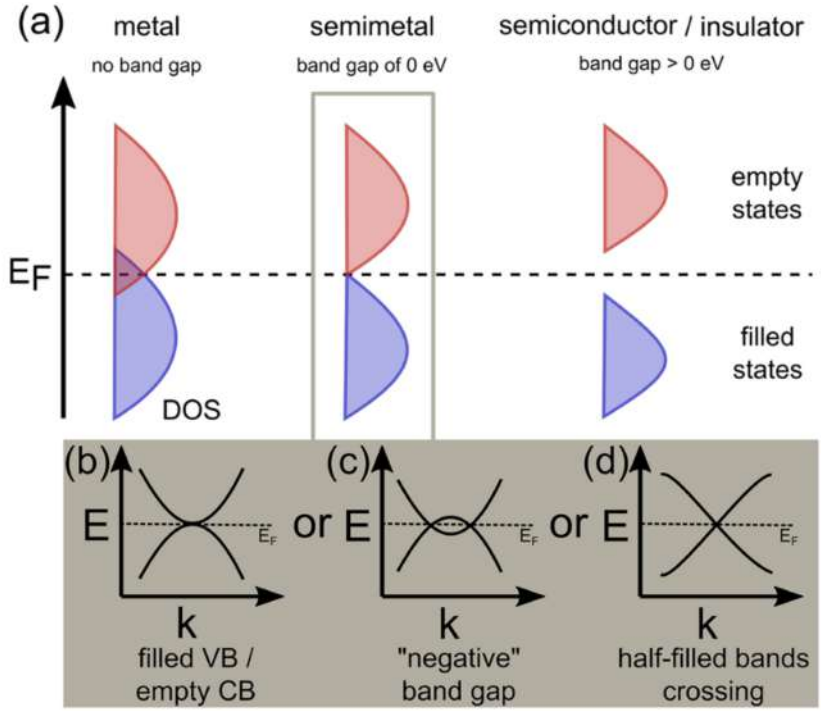

Figure 1.8: (a)Schematic representation of metal, semi metal and insulator. The bottom panel shows different types of band structure leading to semi metallic behavior: (b) touching filled valence band (VB) and empty conduction band (CB), (c) overlapping bands, and (d) crossing of half-filled bands. (b) (Reproduced from [75])

atoms per unit cell are sufficient to give rise to topological semi metallic (TSM) state [75].

A semi metal can be thought of as an intermediate state between metal and semi conductor. These are zero bandgap material but density of states vanishes at the Fermi energy. This may occur when completely occupied and unoccupied bands touch or overlap (see Fig. 1.8b or c). Another way to obtain semi metallic states is when the valence band is half filled (see Fig. 1.8d). In this case, the Fermi level cuts through a single node of bands and consequently the Fermi surface is point shaped. Presence of such node, known as Dirac (or Weyl) node, makes the band topology non trivial.

In our work, we have considered $LaAgSb_2$, a member of this class of materials with a tolerance factor of 0.91. This material hosts multiple Dirac cones near Fermi levels. Additionally, multiple charge density waves (CDW) transitions, one at 210 K along a direction and another along c direction at 186 K has been observed in this material [76]. Although both the CDW states are incommensurate, the second CDW undergoes a transition at 164 K to a commensurate state with a periodicity of 6 unit cells along the c direction. We have discussed the origin of this structural distortion. Optimizing the structure within first-principle calculations, we have further shown that an unusual chiral metallic phase exists at low temperatures in which inversion symmetry is broken.

We have studied the effect of the structural modulation on the electronic structure as well. Planar Hall signal have been proven to be an useful experimental technique to probe the band topology in these materials. Using experimental planar Hall data of single

crystalline $LaAgSb_2$[1], we have shown that at high temperatures, the anisotropic Dirac cone cause negative amplitude planar Hall signal while at low temperature due to strong Berry curvature the system shows enhanced positive amplitude planar Hall signal through chiral anomaly.

1.5 Metal Insulator Transitions and Magnetism

The materials discussed so far does not show any spontaneous magnetism. In the last part of this thesis, we are concerned with magnetic materials. Transition metal oxides have been proven to be an important class of materials in the context of magnetism and the effect of magnetic ordering on electronic properties. Apart from conventional ferromagnetic or anti ferromagnetic ordering of localized spin moments, this class of materials also exhibit various "exotic" magnetic phenomena like spin glass phase, noncollinear spin spirals [78], skyrmions [79], spontaneous magnetic reversal , exchange bias [80] etc.

In 1950, Anderson [81] showed that superexchange, an indirect exchange between neighboring magnetic moments due to virtual electron hopping via the non magnetic anions, favours antiferromagnetic ordering in these materials [82]. Further development of Goodenough-Kanamori rules [83, 84] explained different magnetic states depending on the structure geometry and the orbitals involved in superexchange or double exchange [85, 86].

The electronic structure in these materials can be described by Hubbard Hamiltonian [87], written in the second quantization nota-

[1]Performed by R. Alam et al. [77]

tion as,

$$\mathcal{H}_{Hubbard} = -t \sum_{\langle i,j \rangle} \sum_{\sigma} \left(\hat{c}^{\dagger}_{i\sigma} \hat{c}_{j\sigma} + \hat{c}^{\dagger}_{j\sigma} \hat{c}_{i\sigma} \right) + U \sum_{i} \hat{n}_{i\uparrow} \hat{n}_{i\downarrow} \tag{1.1}$$

where $\{i, j\}$ are different lattice site, σ is the spin index running over $\{\uparrow, \downarrow\}$, $\hat{c}^{\dagger}$ and $\hat{c}$ are the creation and annihilation operators. The spin density operator $\hat{n}_{i\sigma}$ at site i and spin σ is given by, $\hat{c}^{\dagger}_{i\sigma} \hat{c}_{i\sigma}$. Both the parameters t and U are taken to be positive for electronic systems.

The first term in the Hamiltonian 1.1, represent the tendency of delocalization of electrons via hopping from site i to site j. Consequently, larger value of the hopping amplitude, t, corresponds to the larger bandwidth(W). The second term represents the electron-electron interactions, approximated here only by Coulomb interactions. For stronger U values the electrons tend to localise at the lattice sites. Therefore, for a system with larger value of U, one may find insulating state even with partially filled d bands. Such materials are known as Mott-Hubbard insulators [88, 89, 90]. Interestingly, Mott argued that the onset of insulating state does not depend on the magnetism of the material.

In 1951 Slater provided another mechanism for metal insulator transitions [91]. In this case, the insulating gap was ascribed to antiferromagnetic long-range ordering. As shown in Fig. 1.9, in the magnetically ordered phase, neighboring sites experience different potentials. This opens up a gap at the magnetic Brillouin zone boundary. Consequently, the materials transform from a metallic paramagnetic state to antiferromagnetic insulator.

In our work, we have considered,$NaOsO_3$, a $5d$ transition metal oxide which shows a simultaneous metal insulator transition and onset

of antiferromagnetic ordering at 410 K [92, 93]. As onsite Coulomb interaction is weaker in this material due to extended nature of $5d$ orbitals, $NaOsO_3$ is considered to be material realisation of the Slater mechanism. Motivated by recent pressure dependent study [94], we have studied the evolution of the electronic band structure and the magnetism in this material as a function of applied pressure. We have find that the magnetic ordering is very robust under pressure. The reason for this has been traced to the structural changes of the material under pressure.

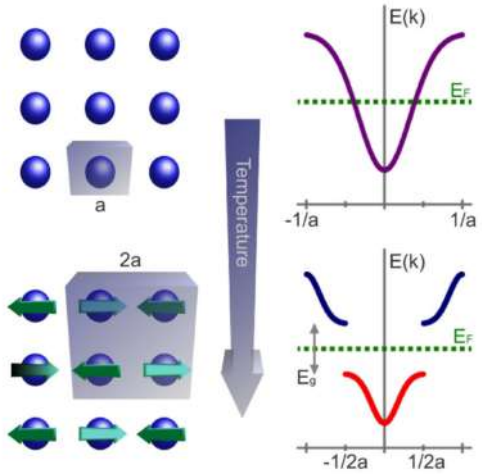

Figure 1.9: Slater mechanism for metal insulator transition. In left, the antiferromagnetic ordering doubles the original unit cell. In right, schematic band structure shows that opposite potential on each neighboring ion opens a gap at magnetic Brillouin zone boundary. (Reproduced from [93])

1.6 Outline of The Thesis

The focus of the work carried out in this thesis is on the relation between different electronic, topological and magnetic ground states in materials with the crystal structure. We have studied various systems ranging from atomically thin 2D materials to layered quasi

2D materials to 3D perovskite oxide and Heusler compounds. The thesis is divided into different parts as mentioned below.

In chapter 2, the background of various techniques used in the work performed in the thesis have been discussed. The electronic structure of different materials have been investigated theoretically using density functional theory. In some instances these *ab initio* results are complemented by model Hamiltonian calculations. Both these techniques have been discussed in detail. Different techniques to perform calculations on magnetic materials and determination of topological invariant have been discussed.

In chapter 3, the monolayer of Mo and W based transition metal dichalcogenides (TMDCs) in their most stable structural configuration, namely hexagonal (1H) polymorph, have been studied. These are known to be semiconducting with a direct bandgap at K point of the 2D hexagonal Brillouin zone. This can be understood as an effect of the crystal field splitting of the d orbitals of the transition metal atoms, which predicts a bandgap between the occupied d_{z^2} orbital and unoccupied $d_{x^2-y^2}$ and d_{xy} orbitals. However, through calculation of orbital character of the eigenstates we are going to show that the orbital character of valence band maximum and conduction band minimum at K point reverses from the crystal field behaviour while at the Γ the orbital character of valence band top and conduction band bottom is same as dictated by the crystal field effects. This level reversal is unusual as the gap between conduction and valence band in these materials is quite large everywhere in the Brillouin zone. We shall further show that any tight binding model constructed with only relevant d bands of the transition metal, as have been employed in various previous studies [60], fails to correctly describe the insulating gap everywhere in the Brillouin zone along with the orbital character

reversal of valence band top and conduction band bottom between Γ and K. Identifying two possible pathways for the d electrons of adjacent metal atoms to interact, one is direct hopping between d states of metal atoms and another is indirect hopping via the chalcogen p states, we have included the in-plane p orbitals of the chalcogen and thereby successfully constructed a minimal tight binding Hamiltonian with 7 basis states that captures both the band gap everywhere in the Brillouin zone and the orbital character reversal at Γ and K.

In chapter 4 we have discussed the 1T and 1T' polymorph of these monolayer TMDCs. The 1T polymoprh is metallic and unstable. Since, The bond length between metal and chalcogen are similar in 1H and 1T polymorph, the change in electronic properties is due to the different crystal field effects arises from different chalcogen environments in these polymorphs. In the 1T phase, octahedral crystal field effects makes the t_{2g} orbitals partially filled and thereby makes this polymorph a metal. We shall show that the inverted bandgap between chalcogen p states and transition metal d states at Γ is present in both 1H and 1T polymorph as the orbital energy difference $\Delta = \epsilon_d - \epsilon_p$ acquires a k dependence due to significant interactions between adjacent transition metals as well as interactions between neighboring chalcogen atoms. However the 1H structure has band extrema at K point and therefore the inverted gap at Γ does not make it a suitable candidate for QSH insulator. The 1T phase is also not a topological insulator due to several other trivial bands crossing the Fermi energy across the Brillouin zone that makes it metallic. The origin of the structural instability in 1T polymorph has been discussed next, by analysing the band dispersions near Fermi energy. It is shown that the two possible pathways of hopping of d electrons compete with each other leading to the smaller bandwidth. Consequently, the system forms dimers between metal atom enhancing the

direct hopping of d electrons between adjacent transition metals. We have next discussed the role of the structural distortion in bringing about the QSH insulating state.

In chapter 5 we study a quasi 2D material $LaAgSb_2$, that host multiple charge density waves (CDW) transitions, one at 210 K along a direction and another along c direction at 186 K. Although both the CDW states are incommensurate, the second CDW undergoes a transition at 164 K to a commensurate state with a periodicity of 6 unit cells along the c direction. Thus this material provide an example where the crystal structure gets modified as temperature is lowered. We have discussed what causes this structural distortion. Optimizing the structure within first-principle calculations, we shall show that an unusual chiral metallic phase exists at low temperatures in which inversion symmetry is also broken. We shall then discuss the effect of this structural modulation at low temperatures on the electronic structure.

In chapter 6, we have used the above mentioned CDW modulated chiral structure of $LaAgSb_2$ at low temperatures, to understand the planar Hall signal in this material. Our collaborators had found in magneto transport experiments performed on the single crystal of $LaAgSb_2$ that planar hall signal is finite at both high and low temperatures although the amplitude reverses sign at the CDW transition point. We shall use the low temperature CDW modulated and high temperature normal metallic structure to understand the sign change in the planar hall signal as the system goes through the CDW transition.

In chapter 7 we have studied a 3D perovskite oxide, $NaOsO_3$, which is known to be a Slater insulator where the insulating state appears

when long range antiferromagnetic ordering sets in [91]. A smaller on-site Coulomb interaction strength as well as weaker electron phonon effects, makes $NaOsO_3$ a rare example of a Slater insulator [92, 93]. $NaOsO_3$ is known to be an insulator with a small band gap of 0.1 eV [95], favoring a G-type antiferromagnetic state below 410 K. However no abrupt change in crystal structure has been observed in this material across the transition. In our study, we have examined the pressure dependence of the electronic structure, as well its evolution under pressure within ab-initio electronic structure calculations. The pressure coefficient of the band gap has been found to be unusually small. We have discussed the reason for such robustness of insulating ground state by studying the magnetism in this material as a function of applied pressure. The structural parameters at various pressure have been discussed and the reason for robust anti ferromagnetic ordering has been described.

In chapter 8 we have discussed interesting magnetic and topological properties of a doped Heusler compound, $Ru_2Fe_xMg_{1-x}Ge$ by specifically focusing on the $x = 0.5$ limit. We shall show the existence Weyl nodes near the Fermi energy. We have then calculated the intrinsic anomalous hall conductivity of this material which matched well with the experiments performed by our collaborators. Additionally, magneto-transport experiments had revealed that the magnetoresistence show inverted behaviour below 175 K. We shall discuss the origin of this inverted behaviour by calculating the clustering energy for Mn domains and the exchange interactions between Fe-Fe, Fe-Mn and Mn-Mn neighboring atom pairs.

Finally, in chapter 9 the key findings of this thesis has been listed along with some of the ideas that have emerged during these studies and can be explored in future theoretical and experimental studies.

Bibliography

[1] R. Peierls. Quelques proprietes typiques des corps solides. *Annales de l'institut Henri Poincaré*, 5(3):177–222, 1935.

[2] L. D. Landau. Zur theorie der phasenumwandlungen ii. *Phys. Z. Sowjetunion*, 11:26–35, 1937.

[3] L. D. Landau and E. M. Lifshitz. *Statistical Physics, Part I.* Pergamon Press, Oxford, 1980.

[4] N. D. Mermin. Crystalline order in two dimensions. *Phys. Rev.*, 176:250–254, Dec 1968.

[5] J A Venables, G D T Spiller, and M Hanbucken. Nucleation and growth of thin films. *Reports on Progress in Physics*, 47(4):399, apr 1984.

[6] J.W. Evans, P.A. Thiel, and M.C. Bartelt. Morphological evolution during epitaxial thin film growth: Formation of 2d islands and 3d mounds. *Surface Science Reports*, 61(1):1–128, 2006.

[7] P. R. Wallace. The band theory of graphite. *Phys. Rev.*, 71:622–634, May 1947.

[8] J. W. McClure. Diamagnetism of graphite. *Phys. Rev.*, 104:666–671, Nov 1956.

[9] J. C. Slonczewski and P. R. Weiss. Band structure of graphite. *Phys. Rev.*, 109:272–279, Jan 1958.

[10] A. K. Geim and K. S. Novoselov. The rise of graphene. *Nature materials*, 6(3):183–191, 2007.

[11] Eduardo Fradkin. Critical behavior of disordered degenerate semiconductors. ii. spectrum and transport properties in mean-field theory. *Phys. Rev. B*, 33:3263–3268, Mar 1986.

[12] Gordon W. Semenoff. Condensed-matter simulation of a three-dimensional anomaly. *Phys. Rev. Lett.*, 53:2449–2452, Dec 1984.

[13] F. D. M. Haldane. Model for a quantum hall effect without landau levels: Condensed-matter realization of the "parity anomaly". *Phys. Rev. Lett.*, 61:2015–2018, Oct 1988.

[14] K. S. Novoselov, A. K. Geim, et al. Electric field effect in atomically thin carbon films. *Science*, 306(5696):666–669, 2004.

[15] K. S. Novoselov et al. Two-dimensional atomic crystals. *Proceedings of the National Academy of Sciences*, 102(30):10451–10453, 2005.

[16] Roscoe G. Dickinson and Linus Pauling. The crystal structure of molybdenite. *Journal of the American Chemical Society*, 45(6):1466–1471, 1923.

[17] J.A. Wilson and A.D. Yoffe. The transition metal dichalcogenides discussion and interpretation of the observed optical, electrical and structural properties. *Advances in Physics*, 18(73):193–335, 1969.

[18] R. F. Frindt, A. D. Yoffe, and Frank Philip Bowden. Physical properties of layer structures : optical properties and photoconductivity of thin crystals of molybdenum disulphide. *Proceedings of the Royal Society of London. Series A. Mathematical and Physical Sciences*, 273(1352):69–83, 1963.

[19] Per Joensen, R.F. Frindt, and S.Roy Morrison. Single-layer mos2. *Materials Research Bulletin*, 21(4):457–461, 1986.

[20] Tianshu Li and Giulia Galli. Electronic properties of mos2 nanoparticles. *The Journal of Physical Chemistry C*, 111(44):16192–16196, 2007.

[21] S. Lebègue and O. Eriksson. Electronic structure of two-dimensional crystals from ab initio theory. *Phys. Rev. B*, 79:115409, Mar 2009.

[22] Z. Y. Zhu, Y. C. Cheng, and U. Schwingenschlögl. Giant spin-orbit-induced spin splitting in two-dimensional transition-metal dichalcogenide semiconductors. *Phys. Rev. B*, 84:153402, Oct 2011.

[23] Di Xiao, Gui-Bin Liu, Wanxiang Feng, Xiaodong Xu, and Wang Yao. Coupled spin and valley physics in monolayers of mos_2 and other group-vi dichalcogenides. *Phys. Rev. Lett.*, 108:196802, May 2012.

[24] Di Xiao, Wang Yao, and Qian Niu. Valley-contrasting physics in graphene: Magnetic moment and topological transport. *Phys. Rev. Lett.*, 99:236809, Dec 2007.

[25] Wang Yao, Di Xiao, and Qian Niu. Valley-dependent optoelectronics from inversion symmetry breaking. *Phys. Rev. B*, 77:235406, Jun 2008.

[26] Shuichi Murakami, Naoto Nagaosa, and Shou-Cheng Zhang. Dissipationless quantum spin current at room temperature. *Science*, 301(5638):1348–1351, 2003.

[27] Jairo Sinova, Dimitrie Culcer, Q. Niu, N. A. Sinitsyn, T. Jungwirth, and A. H. MacDonald. Universal intrinsic spin hall effect. *Phys. Rev. Lett.*, 92:126603, Mar 2004.

[28] Y. K. Kato, R. C. Myers, A. C. Gossard, and D. D. Awschalom. Observation of the spin hall effect in semiconductors. *Science*, 306(5703):1910–1913, 2004.

[29] J. Wunderlich, B. Kaestner, J. Sinova, and T. Jungwirth. Experimental observation of the spin-hall effect in a two-dimensional

spin-orbit coupled semiconductor system. *Phys. Rev. Lett.*, 94:047204, Feb 2005.

[30] H. Kontani, T. Tanaka, D. S. Hirashima, K. Yamada, and J. Inoue. Giant intrinsic spin and orbital hall effects in sr_2mo_4 (m = Ru, rh, mo). *Phys. Rev. Lett.*, 100:096601, Mar 2008.

[31] T. Tanaka, H. Kontani, M. Naito, T. Naito, D. S. Hirashima, K. Yamada, and J. Inoue. Intrinsic spin hall effect and orbital hall effect in $4d$ and $5d$ transition metals. *Phys. Rev. B*, 77:165117, Apr 2008.

[32] H. Kontani, T. Tanaka, D. S. Hirashima, K. Yamada, and J. Inoue. Giant intrinsic spin and orbital hall effects in sr_2mo_4 (m = Ru, rh, mo). *Phys. Rev. Lett.*, 100:096601, Mar 2008.

[33] Dongwook Go, Daegeun Jo, Changyoung Kim, and Hyun-Woo Lee. Intrinsic spin and orbital hall effects from orbital texture. *Phys. Rev. Lett.*, 121:086602, Aug 2018.

[34] Daegeun Jo, Dongwook Go, and Hyun-Woo Lee. Gigantic intrinsic orbital hall effects in weakly spin-orbit coupled metals. *Phys. Rev. B*, 98:214405, Dec 2018.

[35] Insu Baek and Hyun-Woo Lee. Negative intrinsic orbital hall effect in group xiv materials. *Phys. Rev. B*, 104:245204, Dec 2021.

[36] Z. C. Zheng, Q. X. Guo, D. Jo, D. Go, L. H. Wang, H. C. Chen, W. Yin, X. M. Wang, G. H. Yu, W. He, H.-W. Lee, J. Teng, and T. Zhu. Magnetization switching driven by current-induced torque from weakly spin-orbit coupled zr. *Phys. Rev. Res.*, 2:013127, Feb 2020.

[37] Shilei Ding, Andrew Ross, Dongwook Go, Lorenzo Baldrati, Zengyao Ren, Frank Freimuth, Sven Becker, Fabian Kammerbauer, Jinbo Yang, Gerhard Jakob, Yuriy Mokrousov, and Mathias Kläui. Harnessing orbital-to-spin conversion of interfacial orbital currents for efficient spin-orbit torques. *Phys. Rev. Lett.*, 125:177201, Oct 2020.

[38] YG. Choi, D. Jo, KH. Ko, et al. Observation of the orbital hall effect in a light metal ti. *Nature , 52–56 (2023)*, 619:52–56, Jul 2023.

[39] Dongwook Go, Daegeun Jo, Tenghua Gao, Kazuya Ando, Stefan Blügel, Hyun-Woo Lee, and Yuriy Mokrousov. Orbital rashba effect in a surface-oxidized cu film. *Phys. Rev. B*, 103:L121113, Mar 2021.

[40] Dongwook Go, Daegeun Jo, Hyun-Woo Lee, Mathias Kläui, and Yuriy Mokrousov. Orbitronics: Orbital currents in solids. *Europhysics Letters*, 135(3):37001, sep 2021.

[41] Sungjoon Park and Bohm-Jung Yang. Phonon angular momentum hall effect. *Nano Letters*, 20(10):7694–7699, 2020. PMID: 32955897.

[42] Fei Xue, Vivek Amin, and Paul M. Haney. Imaging the valley and orbital hall effect in monolayer mos_2. *Phys. Rev. B*, 102:161103, Oct 2020.

[43] Cong Xiao, Huiying Liu, Jianzhou Zhao, Shengyuan A. Yang, and Qian Niu. Thermoelectric generation of orbital magnetization in metals. *Phys. Rev. B*, 103:045401, Jan 2021.

[44] Cong Xiao, Yafei Ren, and Bangguo Xiong. Adiabatically induced orbital magnetization. *Phys. Rev. B*, 103:115432, Mar 2021.

[45] Võ Tien Phong, Zachariah Addison, Seongjin Ahn, Hongki Min, Ritesh Agarwal, and E. J. Mele. Optically controlled orbitronics on a triangular lattice. *Phys. Rev. Lett.*, 123:236403, Dec 2019.

[46] Tarik P. Cysne, Filipe S. M. Guimarães, Luis M. Canonico, Tatiana G. Rappoport, and R. B. Muniz. Orbital magnetoelectric effect in zigzag nanoribbons of p-band systems. *Phys. Rev. B*, 104:165403, Oct 2021.

[47] Satoru Hayami, Hiroaki Kusunose, and Yukitoshi Motome. Emergent spin-valley-orbital physics by spontaneous parity breaking. *Journal of Physics: Condensed Matter*, 28(39):395601, aug 2016.

[48] Luis M. Canonico, Tatiana G. Rappoport, and R. B. Muniz. Spin and charge transport of multiorbital quantum spin hall insulators. *Phys. Rev. Lett.*, 122:196601, May 2019.

[49] Luis M. Canonico, Tarik P. Cysne, Tatiana G. Rappoport, and R. B. Muniz. Two-dimensional orbital hall insulators. *Phys. Rev. B*, 101:075429, Feb 2020.

[50] Luis M. Canonico, Tarik P. Cysne, Alejandro Molina-Sanchez, R. B. Muniz, and Tatiana G. Rappoport. Orbital hall insulating phase in transition metal dichalcogenide monolayers. *Phys. Rev. B*, 101:161409, Apr 2020.

[51] F. Crasto de Lima, G. J. Ferreira, and R. H. Miwa. Orbital pseudospin-momentum locking in two-dimensional chiral borophene. *Nano Letters*, 19(9):6564–6568, 2019. PMID: 31424949.

[52] S. Beaulieu, J. Schusser, S. Dong, M. Schüler, T. Pincelli, M. Dendzik, J. Maklar, A. Neef, H. Ebert, K. Hricovini, M. Wolf,

J. Braun, L. Rettig, J. Minár, and R. Ernstorfer. Revealing hidden orbital pseudospin texture with time-reversal dichroism in photoelectron angular distributions. *Phys. Rev. Lett.*, 125:216404, Nov 2020.

[53] Michael Schüler, Tommaso Pincelli, Shuo Dong, Thomas P. Devereaux, Martin Wolf, Laurenz Rettig, Ralph Ernstorfer, and Samuel Beaulieu. Polarization-modulated angle-resolved photoemission spectroscopy: Toward circular dichroism without circular photons and bloch wave-function reconstruction. *Phys. Rev. X*, 12:011019, Jan 2022.

[54] Sayantika Bhowal and S. Satpathy. Intrinsic orbital moment and prediction of a large orbital hall effect in two-dimensional transition metal dichalcogenides. *Phys. Rev. B*, 101:121112, Mar 2020.

[55] Sayantika Bhowal and S. Satpathy. Intrinsic orbital and spin hall effects in monolayer transition metal dichalcogenides. *Phys. Rev. B*, 102:035409, Jul 2020.

[56] Tarik P. Cysne et al. Disentangling orbital and valley hall effects in bilayers of transition metal dichalcogenides. *Phys. Rev. Lett.*, 126:056601, Feb 2021.

[57] Sayantika Bhowal and Giovanni Vignale. Orbital hall effect as an alternative to valley hall effect in gapped graphene. *Phys. Rev. B*, 103:195309, May 2021.

[58] D. Go, JP. Hanke, P. Buhl, et al. Toward surface orbitronics: giant orbital magnetism from the orbital rashba effect at the surface of sp-metals. *Sci Rep*, 7:46742, 2017.

[59] S. Bhowal and S. Satpathy. Electric field tuning of the anomalous hall effect at oxide interfaces. *npj Comput. Mater*, 5:61, 2019.

[60] Gui-Bin Liu et al. Three-band tight-binding model for monolayers of group-vib transition metal dichalcogenides. *Phys. Rev. B*, 88:085433, Aug 2013.

[61] K. v. Klitzing, G. Dorda, and M. Pepper. New method for high-accuracy determination of the fine-structure constant based on quantized hall resistance. *Phys. Rev. Lett.*, 45:494–497, Aug 1980.

[62] D. C. Tsui, H. L. Stormer, and A. C. Gossard. Two-dimensional magnetotransport in the extreme quantum limit. *Phys. Rev. Lett.*, 48:1559–1562, May 1982.

[63] Charles L. Kane and Eugene J. Mele. A new spin on the insulating state. *Science*, 314(5806):1692–1693, 2006.

[64] D. J. Thouless, M. Kohmoto, M. P. Nightingale, and M. den Nijs. Quantized hall conductance in a two-dimensional periodic potential. *Phys. Rev. Lett.*, 49:405–408, Aug 1982.

[65] Barry Simon. Holonomy, the quantum adiabatic theorem, and berry's phase. *Phys. Rev. Lett.*, 51:2167–2170, Dec 1983.

[66] C. L. Kane and E. J. Mele. Quantum spin hall effect in graphene. *Phys. Rev. Lett.*, 95:226801, Nov 2005.

[67] B. Andrei Bernevig, Taylor L. Hughes, and Shou-Cheng Zhang. Quantum spin hall effect and topological phase transition in hgte quantum wells. *Science*, 314(5806):1757–1761, 2006.

[68] Markus König, Steffen Wiedmann, Christoph Brüne, Andreas Roth, Hartmut Buhmann, Laurens W. Molenkamp, Xiao-Liang Qi, and Shou-Cheng Zhang. Quantum spin hall insulator state in hgte quantum wells. *Science*, 318(5851):766–770, 2007.

[69] C. L. Kane and E. J. Mele. Z_2 topological order and the quantum spin hall effect. *Phys. Rev. Lett.*, 95:146802, Sep 2005.

[70] Xiao-Liang Qi, Taylor L. Hughes, and Shou-Cheng Zhang. Topological field theory of time-reversal invariant insulators. *Phys. Rev. B*, 78:195424, Nov 2008.

[71] Xiaofeng Qian et al. Quantum spin hall effect in two-dimensional transition metal dichalcogenides. *Science*, 346(6215):1344–1347, 2014.

[72] Huaqing Huang et al. Emerging topological states in quasi-two-dimensional materials. *WIREs Computational Molecular Science*, 7(4):e1296, 2019.

[73] Sebastian Klemenz, Shiming Lei, and Leslie M. Schoop. Topological semimetals in square-net materials. *Annual Review of Materials Research*, 49(Volume 49, 2019):185–206, 2019.

[74] Wolfgang Tremel and Roald Hoffmann. Square nets of main-group elements in solid-state materials. *Journal of the American Chemical Society*, 109(1):124–140, 1987.

[75] Sebastian Klemenz et al. The role of delocalized chemical bonding in square-net-based topological semimetals. *Journal of the American Chemical Society*, 142(13):6350–6359, 2020.

[76] C. Song et al. Charge-density-wave orderings in laagsb$_2$: an x-ray scattering study. *Phys. Rev. B*, 68:035113, Jul 2003.

[77] Rafiqul Alam, Prasun Boyal, et al. Detection of nontrivial topology driven by charge density wave in a semi-dirac metal. *Advanced Functional Materials*, 33(44):2306751, 2023.

[78] D. Khomskii. *Electronic Structure, Exchange and Magnetism in Oxides*, pages 89–116. Springer Berlin Heidelberg, Berlin, Heidelberg, 2001.

[79] Keng Yuan Meng et al. Observation of nanoscale skyrmions in sriro3/srruo3 bilayers. *Nano Letters*, 19(5):3169–3175, 2019.

[80] P. Wartewig et al. Magnetic properties of zn and ti substituted barium hexaferrite. *Journal of Magnetism and Magnetic Materials*, 192(1):83–99, 1999.

[81] P. W. Anderson. Antiferromagnetism. theory of superexchange interaction. *Phys. Rev.*, 79:350–356, Jul 1950.

[82] P. W. Anderson. New approach to the theory of superexchange interactions. *Phys. Rev.*, 115:2–13, Jul 1959.

[83] Junjiro Kanamori. Theory of the Magnetic Properties of Ferrous and Cobaltous Oxides. *Progress of Theoretical Physics*, 17(2):177–196, 02 1957.

[84] Junjiro Kanamori. Superexchange interaction and symmetry properties of electron orbitals. *Journal of Physics and Chemistry of Solids*, 10(2):87–98, 1959.

[85] John B. Goodenough. An interpretation of the magnetic properties of the perovskite type mixed crystals $\mathrm{la}_{1-x}\mathrm{sr}_x\mathrm{coo}_3$. *Journal of Physics and Chemistry of Solids*, 6(2):287–297, 1958.

[86] John B. Goodenough. Theory of the role of covalence in the perovskite type manganites $[\mathrm{La}, m(\mathrm{II})]\mathrm{Mno}_3$. *Phys. Rev.*, 100:564–573, Oct 1955.

[87] J. Hubbard and Brian Hilton Flowers. Electron correlations in narrow energy bands. *Proceedings of the Royal Society of London. Series A. Mathematical and Physical Sciences*, 276(1365):238–257, 1963.

[88] N. F. Mott. The transition to the metallic state. *The Philosophical Magazine: A Journal of Theoretical Experimental and Applied Physics*, 6(62):287–309, 1961.

[89] N F Mott and R Peierls. Discussion of the paper by de boer and verwey. *Proceedings of the Physical Society*, 49(4S):72, aug 1937.

[90] N F Mott. The basis of the electron theory of metals, with special reference to the transition metals. *Proceedings of the Physical Society. Section A*, 62(7):416, jul 1949.

[91] J. C. Slater. Magnetic effects and the hartree-fock equation. *Phys. Rev.*, 82:538–541, May 1951.

[92] Y. G. Shi et al. Continuous metal-insulator transition of the antiferromagnetic perovskite $naoso_3$. *Phys. Rev. B*, 80:161104, Oct 2009.

[93] S. Calder et al. Magnetically driven metal-insulator transition in $naoso_3$. *Phys. Rev. Lett.*, 108:257209, Jun 2012.

[94] R. Sereika, P. Liu, B. Kim, et al. Aberrant electronic and structural alterations in pressure tuned perovskite $naoso_3$. *npj Quantum Mater*, 5:66, 2020.

[95] I. Vecchio, A. Perucchi, Di Pietro P., et al. Magnetically driven metal-insulator transition in $naoso_3$. *Sci. Rep.*, 3:2990, Oct 2013.

CHAPTER 2

Methodology

"Everything should be made as simple as possible, but no simpler"

Albert Einstein

2.1 Many Body Hamiltonian

Macroscopic properties of solids depend on the interactions between its constituents. The primary force in play is the electrostatic force between electrons and nuclei. At this length scale, the theory for interactions between such charged particles is inherently quantum mechanical in nature and can be described by a time independent many body Schrödinger equation, $\mathcal{H}\Psi = E\Psi$, where Ψ is the many body wave function , E is the energy eigenvalue and $\mathcal{H}$ is the many body Hamiltonian expressed as,

$$\begin{aligned}\mathcal{H} = -\frac{\hbar^2}{2m_e}\sum_i \nabla_i^2 - \frac{\hbar^2}{2M_I}\sum_I \nabla_I^2 + \frac{1}{2}\sum_{i\neq j}\frac{e^2}{|r_i - r_j|} \\ + \frac{1}{2}\sum_{I\neq J}\frac{Z_I Z_J e^2}{|R_I - R_J|} - \sum_{i,I}\frac{Z_I e^2}{|R_i - r_i|}\end{aligned} \tag{2.1}$$

the indices $\{ij\}$ denotes the electrons in the system whereas the indices $\{IJ\}$ correspond to the nuclei present in the solid. r_i, m_e are

the position and mass of i^{th} electron respectively. R_I, Z_I and M_I are the position, atomic number and mass of the I^{th} nucleus. $\hbar$ is the Plank's constant. The first two terms in $\mathcal{H}$ denote the kinetic energy of the electrons and nuclei respectively. The third term indicates the electrostatic Coulomb repulsion between different electrons and the fourth term represents Coulomb repulsion between different nuclei. The final term is the Coulomb attraction between electrons and nuclei. Letting T represent the kinetic energy and V represent the potential energy, the Hamiltonian is written in a compact form as

$$\mathcal{H} = T_e(\mathbf{r}) + T_n(\mathbf{R}) + V_{ee}(\mathbf{r}) + V_{nn}(\mathbf{R}) + V_{en}(\mathbf{r}, \mathbf{R}) \tag{2.2}$$

Although the many-body Hamiltonian (2.2) can in principle be solved to get the many body wave function containing all the details and has been solved analytically for the simplest possible system Hydrogen atom, it is almost impossible to solve such a many body equation for the very large no. of particles one generally have to deal with while studying solids. In order to get insights of macroscopic details out of this microscopic Hamiltonian, it is often more useful to look at the behaviour of the electrons in the solid. Evidently approximations are needed to make use of the many-body Hamiltonian. In the following sections, few such approximations have been described.

2.2 Born-Oppenheimer Approximation

The Born-Oppenheimer approximation [1] is a simple yet very powerful tool that simplifies (2.2) greatly. Using the fact that the nuclei in a material are practically static compared to the electrons due to mass of electron being much smaller than that of the nuclei, the approximation is that the electron and nuclei degrees of freedom to be

decoupled from each other as follows,

$$\Psi_{ne}(\mathbf{r}, \mathbf{R}) = X_{ne}(\mathbf{R})\phi_e(\mathbf{r}, \mathbf{R}) \tag{2.3}$$

Where, $\Psi_{ne}(\mathbf{r}, \mathbf{R})$ is called the Born-Oppenheimer wave function. The vibrational part, $X_{ne}(R)$ depends on both electronic and nuclear quantum number and is a function of nuclei position only whereas the electronic part depends on electronic quantum number and function of both the nucleus and electron position. Physically, the electronic wave function reaches equilibrium much quickly and hence only the position of nuclei and not its motion influence the electronic states. Putting the Born-Oppenheimer ansatz into (2.2), the electronic Hamiltonian is obtained as,

$$\mathcal{H}^{elec}(\mathbf{r}, \mathbf{R}) = T_e(\mathbf{r}) + V_{en}(\mathbf{r}, \mathbf{R}) + V_{ee}(\mathbf{r}) \tag{2.4}$$

satisfying,

$$\mathcal{H}^{elec}(\mathbf{r}, \mathbf{R})\phi_e(\mathbf{r}, \mathbf{R}) = E_e(\mathbf{R})\phi_e(\mathbf{r}, \mathbf{R}) \tag{2.5}$$

where, $E_e(\mathbf{R})$ is the energy eigen values of the electronic Hamiltonian which combines with the repulsive Coulomb interaction between nuclei (V_{nn}), to form the potential energy function controlling the nuclear positions and consequently the Schrödinger equation of vibrational part will have the form,

$$(T_n(\mathbf{R}) + V_{nn}(\mathbf{R}) + E_e(\mathbf{R}))X_{ne}(\mathbf{R}) = E_{ne}X_{ne}(\mathbf{R}) \tag{2.6}$$

The electronic Hamiltonian (2.4) becomes the central focus for now. Although it is simplified as one does not need to worry about nuclear motion anymore, the eigenvalue equation (2.5) is still a many-body equation due to the presence of V_{ee} in (2.4). Furthermore, the many body electronic wave function one seeks to compute is 3N dimensional for N electrons in the system. One way to solve the many-body electronic Schrödinger equation is based on the expansion of

the wave-function in terms of Slater determinant[2]. The most simple method using this approach, Hartree-Fock method[3], dates back all the way to 1935. Although many more sophisticated approach, collectively known as post-Hartree-Fock method[4], have been developed since then, the problem of huge computational effort due to high number of coordinates (3N for N electrons) remains. This limits the application of these methods to atoms or molecules and makes it practically impossible to use these methods to larger and complex systems like bio-molecules or solids.

In the next section a different approach to the problem is described which not only reduce the number of variable in the problem but also makes the many body problem an effective single particle problem. This approach, known as density functional theory(DFT) [5], has been used on various materials in order to understand their electronic structure in this thesis.

2.3 Density Functional Theory

In 1964, Hohenberg and Kohn developed DFT with the aim to describe the ground state properties of the electronic Hamiltonian (2.5) without dealing with the complicated many-body wave function[6]. The fundamental proposition of DFT is that the electron density, defined as the probability of finding an electron in a specific location around an atom or molecule, contains all the information of the ground state energy and wave function. Electron density is an observable meaning it can be measured through experiments like electron diffraction [7]. Mathematically, density for an N-electron system can

be calculated from the normalized N-electron wave function,

$$n(\mathbf{r}_i) = N \int d^3\mathbf{r}_1 ... \int d^3\mathbf{r}_{i-1} \int d^3\mathbf{r}_{i+1} ... \int d^3\mathbf{r}_N |\Psi(\mathbf{r}_1, \mathbf{r}_2, ..., \mathbf{r}_i, ..., \mathbf{r}_N)|^2 \tag{2.7}$$

The immediate benefit of using DFT is that the electron density of a N-electron system is a function of only three coordinate variable unlike the many body wave function which is function of $3N$ variable for a material with N electrons. Furthermore, two theorems by Hohenberg and Kohn[6] maps the complicated many-body problem onto an effective mean-field single particle problem. This reduces complexity enormously and forms the backbone of the modern formulation of density functional theory.

2.3.1 Hohenberg-Kohn Theorems

***Theorem 1*:** *"the external potential $V_{ext}(\boldsymbol{r})$ is a unique functional of $n(\boldsymbol{r})$; since, in turn $V_{ext}(\boldsymbol{r})$ fixes $\mathcal{H}^{elec}$, the full many particle ground state is a unique functional of $n(\boldsymbol{r})$ "*

In simpler words, the ground state electron density of a system of interacting particles in an external potential $V_{ext}(\mathbf{r})$ is unique Or alternatively if two electron system are trapped in external potential V^1_{ext} and V^2_{ext} respectively and have same ground state electron density, then the potentials can differ at most by a constant.

Proof of Theorem 1: Assume, two different external potentials, $V_1(\mathbf{r})$ and $V_2(\mathbf{r})$ give rise to the same ground state density n(r) but different ground state wave function.

Let, Ψ_1 and Ψ_2 (where $\Psi_1 \neq \Psi_2$) be the the ground state wavefunction corresponding to $V^1_{ext}(\mathbf{r})$ and $V^2_{ext}(\mathbf{r})$ respectively. (Here we

have assumed that $V^1_{ext}(\mathbf{r})$and $V^2_{ext}(\mathbf{r})$) differ not just by a constant as the ground state wave functions would be same in that case.)

Since the ground state energy is the lowest energy for a system,

$$E_1 = \langle\Psi_1|\mathcal{H}_1|\Psi_1\rangle < \langle\Psi_2|\mathcal{H}_1|\Psi_2\rangle \tag{2.8}$$

$$E_2 = \langle\Psi_2|\mathcal{H}_2|\Psi_2\rangle < \langle\Psi_1|\mathcal{H}_2|\Psi_1\rangle \tag{2.9}$$

Write (2.8) as,

$$\begin{aligned} E_1 &< \langle\Psi_2|\mathcal{H}_1|\Psi_2\rangle \\ &= \langle\Psi_2|\mathcal{H}_2|\Psi_2\rangle + \langle\Psi_2|[\mathcal{H}_1 - \mathcal{H}_2]|\Psi_2\rangle \\ &= E_2 + \langle\Psi_2|[V^1_{ext} - V^2_{ext}]|\Psi_2\rangle \\ &= E_2 + \int [V^1_{ext} - V^2_{ext}]n(\mathbf{r})d\mathbf{r} \end{aligned} \tag{2.10}$$

Similarly from (2.9),

$$\begin{aligned} E_2 &< \langle\Psi_1|\mathcal{H}_2|\Psi_1\rangle \\ &= \langle\Psi_1|\mathcal{H}_1|\Psi_1\rangle + \langle\Psi_1|[\mathcal{H}_2 - \mathcal{H}_1]|\Psi_1\rangle \\ &= E_1 + \langle\Psi_1|[V^2_{ext} - V^1_{ext}]|\Psi_1\rangle \\ &= E_1 + \int [V^2_{ext} - V^1_{ext}]n(\mathbf{r})d\mathbf{r} \end{aligned} \tag{2.11}$$

Adding (2.10) and (2.11),

$$E_1 + E_2 < E_1 + E_2 \tag{2.12}$$

We have reached a clear contradiction here and thus proving the first theorem that there cannot be two different V_{ext} that yield the same ground state electron density, or, in other words, that the ground state density uniquely specifies the external potential V_{ext}.

Therefore, a given charge density uniquely fix external potential in the electronic Hamiltonian. Given the energy functional $E[n(\mathbf{r})]$, the second theorem tells us about how to obtain the ground state energy from this functional.

***Theorem 2*:** *"The global minimum of energy functional represents the true ground state energy and the electron density that minimizes this energy ($E[n(r)]$) is the ground state charge density of the system."*

This is the well known variational principle. This asserts that out of all possible electron density for a N- electron system, the ground state density is the one which gives minimum energy. However these theorems are just proof of existence of a unique map between the ground state density, $n_0(\mathbf{r})$ and the ground state energy $E_0 = E[n_0(\mathbf{r})]$. Unfortunately, the exact form of the functional is not fully known. In the following section, Kohn-Sham formulation is discussed which gives an way to make use of the theorems and find a way to map the original many particle problem onto an effective single particle problem.

2.3.2 Kohn Sham Formalism

For a set of N interacting electrons, in an external potential V_{ext} is due to the Coulomb attraction from "static" nuclei. The electronic Hamiltonian reads,

$$\mathcal{H} = T_e + V_{ee} + V_{ext} \tag{2.13}$$

Since, the complete ground state energy is a functional of the ground state electron density so must be its individual component,

$$E[n(\mathbf{r})] = T[n(\mathbf{r})] + E_{ee}[n(\mathbf{r})] + V_{ext}[n(\mathbf{r})] \tag{2.14}$$

It is convenient to separate the first two terms, Kinetic energy and electron-electron repulsion, not depending on the system, from the third term which is system specific depending on no. and position of the nuclei. The universal term not depending on the specifics of the system are therefore clubbed together into one functional denoted

as $F_{HK}[n(\mathbf{r})]$ and the third term is given by, $\int n(\mathbf{r})V_{ext}(\mathbf{r})d^3r$. The energy functional becomes,

$$E[n(\mathbf{r})] = F_{HK}[n(\mathbf{r})] + \int n(\mathbf{r})V_{ext}(\mathbf{r})d^3r \tag{2.15}$$

This innocent looking term $F_{HK}[n(r)]$, called Hohenberg-Kohn functional, is the holy grail of density functional theory. If the functional form were known exactly, the Schrödinger equation would be solve exactly. Furthermore, since the functional form is universal completely independent of system, it would have been same for the most simple system to gigantic molecules or solids. But, the explicit form of both these functional is not possible to determine. However, the classical Coulomb part from the latter can be extracted exactly.

$$\begin{aligned} E_{ee}[n(r)] &= \frac{1}{2}\int d\mathbf{r}_i \int d\mathbf{r}_j \frac{n(\mathbf{r}_i)n(\mathbf{r}_j)}{|\mathbf{r}_i - \mathbf{r}_j|} + \Delta E_{ee} \\ &= E_H[n(\mathbf{r})] + \Delta E_{ee} \end{aligned} \tag{2.16}$$

The first term, known as Hartree energy [8] ($E_H[n(\mathbf{r})]$) representing classical Coulomb repulsion between electrons. The second term in principle includes all other possible quantum mechanical interaction between electrons (self-interaction correction, exchange and Coulomb correlation). Writing the explicit functional form for kinetic energy functional $T[n(r)]$ for interacting electrons is impossible.

Kohn-Sham Orbitals

In the Kohn-Sham formalism, this term (ΔE_{ee}) is replaced by a hypothetical N-electron non-interacting system such that the electron density remains same as the interacting system. The electron density in terms of these hypothetical non-interacting single electron wave-

functions $\phi_i(\mathbf{r})$ known as Kohn-sham[9] orbitals is therefore given by,

$$n(\mathbf{r}) = \sum_{i=1}^{N} \phi_i^*(\mathbf{r})\phi_i(\mathbf{r}) \tag{2.17}$$

Before writing the Kinetic energy functional using these orbitals, it must be stress that these orbitals are purely mathematical construction and have no physical meaning. The kinetic energy of the N-electron interacting system is now written as the sum of kinetic energies of non-interacting electrons occupying Kohn-Sham orbitals and an extra correction term due to the interactions between electrons as follows .

$$\begin{aligned} T[n(\mathbf{r})] &= \sum_{i=1}^{N} \int \phi_i^*(\mathbf{r}) \Big[-\frac{\hbar^2}{2m}\nabla^2 \Big] \phi_i(\mathbf{r}) d^3\mathbf{r} + \Delta T_c \\ &= T_0[n(\mathbf{r})] + \Delta T_c \end{aligned} \tag{2.18}$$

From (2.16) and (2.18),

$$\begin{aligned} F_{HK}[n(\mathbf{r})] &= T_0[n(\mathbf{r})] + E_H[n(\mathbf{r})] + \Delta E_{ee} + \Delta T_c \\ &= T_0[n(\mathbf{r})] + E_H[n(\mathbf{r})] + E_{XC}[n(\mathbf{r})] \end{aligned} \tag{2.19}$$

Where, the last term clubs together the electron-electron interaction other than Coulomb repulsion and the correction in the kinetic energy due to interaction between electrons. Aptly this term is called the exchange-correlation functional. This makes the total energy functional in (2.15) to be,

$$E[n(\mathbf{r})] = T_0[n(\mathbf{r})] + \int n(\mathbf{r}) V_{ext}(\mathbf{r}) d^3r + E_H[n(\mathbf{r})] + E_{XC}[n(\mathbf{r})] \tag{2.20}$$

The functional form of the first and third term is given in the equation (2.18),(2.16) respectively. However, the functional form of the

last term is not known and can only be approximated using different techniques for practical purposes. These approximation will be discussed later on, but for the time being we focus on the minimization problem at hand. That is, minimizing the energy functional given by (2.15) and (2.19) to determine the ground state energy.

Minimization of Energy Functional

The aim is to find out Kohn-Sham orbitals,$\phi_i(\mathbf{r})$ which produce the density $n(\mathbf{r})$ that minimizes the functional in equation (2.20). Furthermore, the minimization is to be performed under the constraint,

$$N = \int n(\mathbf{r}) d^3\mathbf{r} \tag{2.21}$$

Or equivalently,

$$1 = \int \phi_i^*(\mathbf{r})\phi_i(\mathbf{r}) d\mathbf{r} \tag{2.22}$$

Which physically means that the number of electrons in the system, N remains conserved or the Kohn-Sham orbitals are orthonormal to each other.
The Lagrange functional of the minimization problem is,

$$\mathcal{L}[\{\phi_i\}] = E[\{\phi_i\}] - \sum_{i=1}^{N} \epsilon_i \left(\int \phi_i^*(\mathbf{r})\phi_i(\mathbf{r}) d\mathbf{r} - 1 \right) \tag{2.23}$$

The Lagrangian must be stationary with respect to variations of the orbitals $\phi_i(\mathbf{r})$ implying that the functional derivative is zero.

$$\frac{\delta \mathcal{L}}{\delta \phi_i^*(\mathbf{r})} = 0 \tag{2.24}$$

Let us calculate functional derivative of each term of equation (2.20) separately. First the variation of the kinetic term due to small

variation of the kohn sham orbital is given as,

$$\begin{aligned} \delta T_0 &= \sum_{j=1}^{N} \int \delta\phi_j^*(\boldsymbol{r}') \Big[-\frac{\hbar^2}{2m}\nabla^2 \Big] \phi_j(\boldsymbol{r}') d^3\boldsymbol{r}' \\ \implies \frac{\delta T_0}{\delta\phi_i(\boldsymbol{r}')} &= \sum_{j=1}^{N} \int \frac{\delta\phi_j^*(\boldsymbol{r}')}{\delta\phi_i(\boldsymbol{r}')} \Big[-\frac{\hbar^2}{2m}\nabla^2 \Big] \phi_j(\boldsymbol{r}') d^3\boldsymbol{r}' \\ &= \Big[-\frac{\hbar^2}{2m}\nabla^2 \Big] \phi_i(\mathbf{r}) \end{aligned} \tag{2.25}$$

The last line is obtained using the condition of orthonormality for Kohn-Sham orbitals given by,

$$\frac{\delta\phi_j(\boldsymbol{r}')}{\delta\phi_i(\boldsymbol{r}')} = \delta_{i,j}\delta(\boldsymbol{r}-\boldsymbol{r}') \tag{2.26}$$

Now, the variation of the second term will be given by,

$$\begin{aligned} \delta\left[\int n(\boldsymbol{r}) V_{ext}(\boldsymbol{r}) d^3\boldsymbol{r} \right] &= \delta \int n(\boldsymbol{r}) V_{ext}(\boldsymbol{r}) d^3\boldsymbol{r} \\ &= \delta \sum_{i=1}^{N} \int \phi_i^*(\boldsymbol{r}) V_{ext}(\boldsymbol{r}) \phi_i(\boldsymbol{r}) d^3\boldsymbol{r} \\ &= \sum_{i=1}^{N} \int \delta\phi_i^*(\boldsymbol{r}) V_{ext}(\boldsymbol{r}) \phi_i(\boldsymbol{r}) d^3\boldsymbol{r} \end{aligned} \tag{2.27}$$

Therefore the functional derivative will be given by,

$$\begin{aligned} \frac{\delta\Big[\int n(\mathbf{r}) V_{ext}(\mathbf{r}) d^3\mathbf{r} \Big]}{\delta\phi_i^*(\mathbf{r})} &= \sum_{j=1}^{N} \int \frac{\delta\phi_j^*(\mathbf{r}')}{\delta\phi_i^*(\mathbf{r})} V_{ext}(\mathbf{r}) \phi_j(\mathbf{r}') d^3\mathbf{r}' \\ &= \sum_{j=1}^{N} \int \delta_{i,j}\delta(\mathbf{r}-\mathbf{r}') V_{ext}(\mathbf{r}) \phi_j(\mathbf{r}') d^3\mathbf{r}' \\ &= V_{ext}(\mathbf{r})\phi_i(\mathbf{r}) \end{aligned} \tag{2.28}$$

Next, the variation of the Hartree term is evaluated using chain rule of functional derivative as follows,

$$\begin{aligned}\frac{\delta E_H[n(\mathbf{r})]}{\delta \phi_i^*(\mathbf{r})} &= \int \frac{\delta E_H[n(\mathbf{r})]}{\delta n(\mathbf{r}')} \frac{\delta n(\mathbf{r}')}{\delta \phi_i^*(\mathbf{r})} d^3\mathbf{r}' \\ &= \int \frac{\delta E_H[n(\mathbf{r})]}{\delta n(\mathbf{r}')} \delta(\mathbf{r}-\mathbf{r}')\phi_i(\mathbf{r}) d^3\mathbf{r}' \\ &= \frac{\delta E_H[n(\mathbf{r})]}{\delta n(\mathbf{r})} \phi_i(\mathbf{r}) \\ &= V_H[n(\mathbf{r})]\phi_i(\mathbf{r})\end{aligned} \tag{2.29}$$

In the last line the Hartree potential, defined by $V_H[n(\mathbf{r})] = \frac{\delta E_H[n(\mathbf{r})]}{\delta n(\mathbf{r})}$, has been introduced which itself is a functional of the density. Similarly, the variation of the exchange correlation energy term is obtained using chain rule as,

$$\begin{aligned}\frac{\delta E_{XC}[n(\mathbf{r})]}{\delta \phi_i^*(\mathbf{r})} &= \int \frac{\delta E_{XC}[n(\mathbf{r})]}{\delta n(\mathbf{r}')} \frac{\delta n(\mathbf{r}')}{\delta \phi_i^*(\mathbf{r})} d^3\mathbf{r}' \\ &= \int \frac{\delta E_{XC}[n(\mathbf{r})]}{\delta n(\mathbf{r}')} \delta(\mathbf{r}-\mathbf{r}')\phi_i(\mathbf{r}) d^3\mathbf{r}' \\ &= \frac{\delta E_{XC}[n(\mathbf{r})]}{\delta n(\mathbf{r})} \phi_i(\mathbf{r}) \\ &= V_{XC}[n(\mathbf{r})]\phi_i(\mathbf{r})\end{aligned} \tag{2.30}$$

Just as before, a new potential named exchange-correlation potential has been defined as $V_{XC}[n(\mathbf{r})] = \frac{\delta E_XC[n(\mathbf{r})]}{\delta n(\mathbf{r})}$

Combining all the terms from equation(2.25),(2.28),(2.29),(2.30), the stationary condition in (2.24) is written as,

$$\Big[-\frac{\hbar^2}{2m}\nabla^2 + V_{ext} + V_H + V_{XC} \Big] \phi_i(\mathbf{r}) = \epsilon_i \phi_i(\mathbf{r}) \tag{2.31}$$

Writing all the potential terms in a single term for compactness we have arrived at the celebrated Kohn-Sham eigenvalue equations,

$$\Big[-\frac{\hbar^2}{2m}\nabla^2 + V_{KS} \Big] \phi_i(\mathbf{r}) = \epsilon_i \phi_i(\mathbf{r}) \tag{2.32}$$

with the eigen functions and eigenvalues respectively being the hypothetical Kohn-Sham orbitals and the Lagrange multipliers. Equation (2.32) is set of effective single particle equations with an effective potential V_{KS}. Mathematically, the KS equations are a set of coupled self-consistent equations since the potential $V_H(\mathbf{r})$ and $V_{XC}(\mathbf{r})$ depends on all the occupied orbitals $\{\phi_i(\mathbf{r})\}$ through the density. Physically, equation (2.32) defines a hypothetical system of N non-interacting electrons with the crucial property, that the ground-state density $n(\mathbf{r})$ of this N non-interacting electron system in an effective external potential $V_{KS}(\mathbf{r})$ is same as the exact ground-state density $n_0(\mathbf{r})$ of the real physical system of N interacting electrons.

Two remarks about the effective Kohn Sham potential is appropriate here.

- The existence of the functional derivative $V_{XC} = \frac{\delta E_{XC}[n(\mathbf{r})]}{\delta n(\mathbf{r})}$ has been assumed without knowing the particular functional form. This assumption is not true for all densities, but can be shown to be always true for densities that are the ground-state densities of a non-interacting system with some local potential.

- The Kohn-Sham potential, V_{KS} is only defined up to an additive constant by virtue of first Hohenberg-Kohn theorem. The constant is chosen to make the potential vanish at infinity i.e. $\lim_{|r|\to\infty} V_{KS}(\mathbf{r}) = 0$

2.3.3 Iterative Scheme for Solving Kohn-Sham Equations

Since the Kohn-Sham equations are needed to be solved self consistently due to the fact that V_{KS} itself depend on the Kohn-Sham orbitals through density, iterative scheme has been developed to obtain the Kohn Sham orbitals which produce the ground state density. The iterative scheme is shown as a flowchart in Fig: 2.1. The iterative steps are as described below.

- Step 1 : An initial trial electron density density, $n(\mathbf{r})$ is provided.
- Step 2 : The trial electron density is used to construct Kohn-Sham potentials.
- Step 3 : The single particle Kohn-Sham equations are solved to obtain the eigen functions $\{\phi_i(\mathbf{r})\}$.
- Step 4 : From single particle eigen functions, electron density is calculated $n(\mathbf{r}) = \sum_{i=1}^{N} \phi_i^*(\mathbf{r})\phi_i(\mathbf{r})$.
- Step 5 : The calculated electron density is compared to the initial density. If they are not same upto a tolerance value, step 2 to step 4 is repeated using the calculated density as initial density for next step.

The iteration is continued till the calculated density in a cycle falls within a predefined tolerance value of the density that particular cycle was started with.

2.3.4 Approximations for Exchange-Correlation Functional

So far we have been able to map the problem of many body of N interacting electrons to a set of N non-interacting particles moving in an effective potential given by $V_{KS} = V_{ext} + V_H + V_{XC}$ with the condition that the ground state electron density is exactly same for

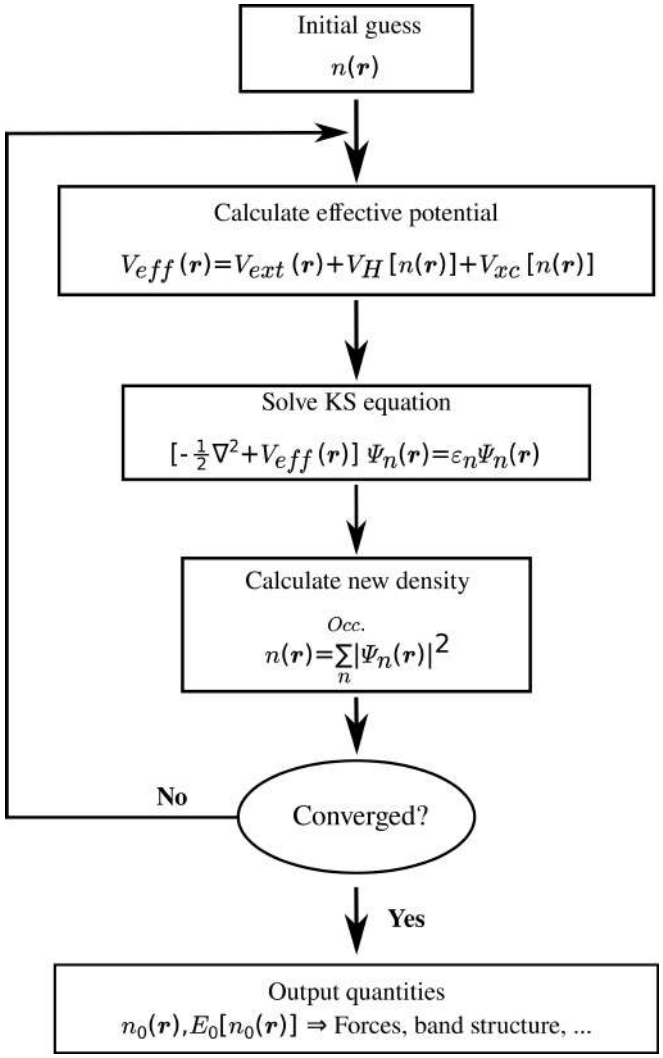

Figure 2.1: The flowchart of a typical DFT calculation. The steps are described in details in the text

both the cases. Furthermore, an iterative scheme has been laid out to solve the set of N non-interacting single particle Hamiltonian self consistently. Another point that needs to be stressed at this point is that the theory presented within the Kohn-Sham formulation to get the ground state density is exact till now and no approximation has been made once the electronic part was separated from the nuclear part using Born Oppenheimer approximation. However, the calculation of ground state density, although exact, is unfortunately impossible as nothing is known about the exact functional form of exchange correlation potential and consequently second step of the iterative scheme can not be performed at this stage. Therefore, one needs to approximate the functional form for the exchange correlation potential. Different approximations have been developed over time. Few among them, those have been used in this thesis, is discussed below.

Local Density Approximation (LDA)

The local-density approximation (LDA), first introduced by Kohn and Sham in their original work [6], considers that the exchange correlation depends only on the value of the electron density $n(\mathbf{r})$ at every point in space. LDA is commonly associated with functionals relying on the homogeneous electron gas (HEG) approximation, which are subsequently utilized in real-world scenarios involving molecules and solids. A local-density approximation for the exchange-correlation energy is given as,

$$E_{xc}^{LDA}[n(\mathbf{r})] = \int n(\mathbf{r})\epsilon_{xc}[n(\mathbf{r})]d\mathbf{r} \tag{2.33}$$

Where, ϵ_{xc} is the exchange-correlation energy per particle of a homogeneous electron gas of charge density $n(\mathbf{r})$.

The exchange-correlation energy is separated into exchange and correlation terms as follows,

$$E_{xc}^{LDA} = E_{x}^{LDA} + E_{c}^{LDA} \tag{2.34}$$

The exchange term is analytically available from the HEG but the correlation term needs to be approximated. The exchange term, sometimes called Dirac exchange [10] or Slater exchange[11] is given by,

$$E_{x}^{LDA}[n(\mathbf{r})] = -\frac{3}{4}\left(\frac{3}{\pi}\right)^{\frac{1}{3}} \int n(\mathbf{r})^{\frac{4}{3}} d\mathbf{r} \tag{2.35}$$

The exact form of the correlation term is again not known. However using perturbation theory, the high[12, 13, 14] and low density[15, 16] limits of correlation energy density that correspond to infinitely weak and infinitely strong correlation has been calculated. Although the intermediate range is obtained by interpolation and some early development had been made to this approach[17], after the advancement of modern computers the correlation energy density can be extracted much easily and accurately from quantum Monte Carlo simulation[18] of HEG.

The LDA assumes that the electron density is locally same as HEG everywhere. As a result, the LDA generally over-estimate the correlation energy but underestimate the exchange energy. These two effect compensate each other to some extent. However, to get a better description of the inhomogeneous systems which will be of practical use in this thesis, we need an approximation that also take the derivatives of the density into consideration. This type of approximations of exchange correlation functionals are described in the following sections.

Generalized Gradient Approximation (GGA)

The first approach to correct the limitations of LDA as mentioned above is expanding energy density as a functional of gradient of density as well. This allows corrections that are due to the changes in density away from the coordinate. The class of approximations that makes use of these expansions are known as generalized gradient approximations (GGA). The general form is given by,

$$E_{xc}^{GGA}[n(\mathbf{r})] = \int n(\mathbf{r})\epsilon_{xc}[n(\mathbf{r}), \nabla n(\mathbf{r})]d\mathbf{r} \tag{2.36}$$

As mentioned in LDA, the quality of GGA results also depends on error cancellation between exchange and correlation energy density. However, energy difference tend to be more accurate in calculations using GGA based functionals. Many many functional form based on GGA have been developed over the years mainly by semi-empirical fitting. Perdew and co-workers[19] initiated the most important work towards development of GGA functional . Ever since many improvement have been done. Some popular form of GGA functionals are Perdew and Wang [20], Becke-Lee-Yang-Par (B-LYP)[21, 22, 23] and Burke and Enzerhof (PBE) functionals[24].

2.4 Numerical Calculations Using DFT

In section 2.3.3 while describing an iterative scheme for Kohn-Sham formalism, a whole series of important details have been skipped. Few of them among many are,

- In step 5, how close should the calculated density to the input density before we consider them to be the same?
- What is a good way to update the trial electron density if the calculated density is "significantly" different?

- How should we define the initial density for a given solid?

In this section, some of these details are discussed which helps us to use DFT based calculations to obtain reliable physical information about a system without simply occupying unnecessary time in the computer. One of the key concept in this regard is "convergence". To understand this let us remember that the ground state density is obtained by solving a set of complex equations (2.17). To solve these differential equations in a computer, a series of numerical approximations is need to be made. For example, multidimensional integrals must be evaluated by taking sample values of the integrand on a finite size grid, any infinite series must be truncated at a finite value, and so on. Of course, in each numerical approximation, one can reach more and more close to the true analytic solution at the expense of computational resources. A "well-converged" numerical solution will be one that is accurate enough to describe the analytic solution of the mathematical equations posed by DFT given a specific exchange-correlation functional.

Of course, the numerical accuracy is different from physical accuracy. As the former only talks about how accurate the solutions to the DFT Kohn-Sham equations are while the later is concerned with the fact that the DFT equations are not same as the original Schrödinger equations due to approximations in the exchange correlation functional. However, the issue of the physical accuracy of DFT, although is of utmost important, is beyond the scope of this thesis. We discuss some practical issues with numerical convergence in this section.

2.4.1 Integration in Momentum Space

In a practical DFT calculation of solids, in which different atoms are arranged in an infinite periodic lattice, momentum space calculation

becomes very important. Very often to get any physical quantity from the calculation one needs to evaluate integrals of the form,

$$g = \frac{V_{cell}}{(2\pi)^3} \int_{BZ} g(\mathbf{k}) d\mathbf{k} \tag{2.37}$$

The integral in (2.37) is performed over the complete Brillouin zone, defined to be the Wigner-Seitz cell of the reciprocal space and the prefactor is the reciprocal of the volume of Brillouin zone. The numerical approximation to these integrals are performed using the well known Gaussian quadrature where the integrand, $g(\mathbf{k})$ in this case, is evaluated at finite no. of $\mathbf{k}$ points with appropriate weight. The most widely method of choosing $\mathbf{k}$ points and their weights were developed by Monkhorst and Pack back in 1976[25] To use this method, one only needs to specify no. of $\mathbf{k}$ points along each direction of reciprocal lattice vectors. As a rule of thumb, the no. of $\mathbf{k}$ points in different directions is decided according to the ratio of the length of reciprocal lattice vectors. Thus for a cubic lattice with all three lattice vector having same length one use $M \times M \times M$ grid of the Brillouin zone for some integer M.

Evidently, it is expected that the numerical accuracy will keep increasing as one increases M and at the limit $M \to \infty$ the numerical approximation will be same as analytically calculated value. In practise however a few calculations with different values of M are performed keeping other input parameters same and the change in total energy of the solid is compared. For a practical example, the DFT calculated energy of monolayer MoS_2 is plotted against the no. of divisions of the Brillouin zone along each reciprocal lattice vector in Fig: 2.2. For smaller number of K points, the total energy changes rapidly, but as $M \geq 5$ the change in energy is less than 0.3 meV implying the energy calculation has converged.

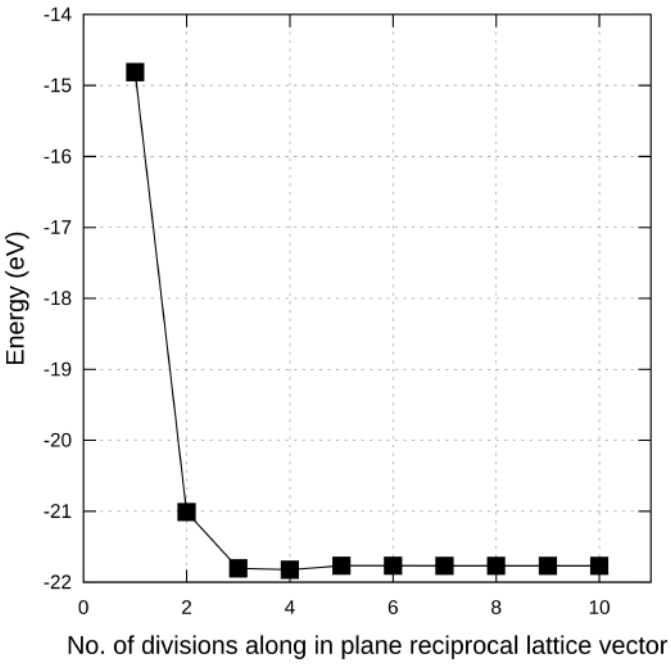

Figure 2.2: The Energy of mono-layer MoS_2 is calculated for different momentum space grid size. As the no. of division increases the calculation becomes well converged.

2.4.2 Discontinuity in Metallic Solids

A special treatment of integrals given by (2.37) is required while doing DFT calculations of Metal. In a metal, the Brillouin zone have regions separated by Fermi surface that are either occupied or unoccupied by electrons. The complication arises as the integrand in the integrals of type (2.37) are discontinuous at Fermi surface implying very high number of **k**-points are required for convergence. There are two different technique to handle this situations.

Smearing

One approach to deal with discontinuity of integrals given in (2.37) are known as smearing methods. The main idea is to force the integrand to be a continuous function by smearing out the unwanted discontinuity with some appropriate continuous function. One simple example of a smearing function could be the Fermi-Dirac function.

$$f(\frac{\mathbf{k}-\mathbf{k_0}}{\sigma}) = \frac{1}{e^{\frac{\mathbf{k}-\mathbf{k_0}}{\sigma}}+1} \tag{2.38}$$

The idea of smearing method is to multiply function of this type with integrals to make it smooth. Notice in the limit $\sigma \to 0$ the above function becomes a step function with it value being 1 for $\mathbf{k} > \mathbf{k_0}$ and 0 for $\mathbf{k} < \mathbf{k_0}$. The continuous function is then integrated and final result is obtained by extrapolating for no smearing (for the above example, it is $\sigma = 0$). In modern calculation, one widely used smearing method for metals was developed by Methfessel and Paxton [26]. However this is not recommended for insulators or semiconductor. Gaussian or Fermi-Dirac smearing is usually more preferred if a material have a bandgap.

Tetrahedron Method

In tetrahedron method the central idea is to define a set of tetrahedron using a discrete set of k points that fills the reciprocal space. The integrand is then interpolated at every point within each tetrahedron. This makes the integrand a simple function in the whole **k** space and the integral can be evaluated using the interpolated value entire space accurately. This method is very useful for calculating density of states or accurate energy from DFT calculations. A wide spread version using this method was developed by Blöchl [27] that include corrections to original linear interpolation.

2.4.3 Cut-off Energy for Plane Wave Basis

In a practical calculation, the Kohn Sham orbitals of equation (2.17) are written using a plane wave basis set as follows.

$$\phi_{\mathbf{k}}(\mathbf{r}) = \sum_{\mathbf{G}} C_{\mathbf{K}+\mathbf{G}} e^{i(\mathbf{k}+\mathbf{G}).\mathbf{r}} \tag{2.39}$$

Where **G** is a reciprocal vector with the form $\mathbf{G} = m_1\mathbf{b_1} + m_2\mathbf{b_2} + m_3\mathbf{b_3}$ where $\mathbf{b}_i$'s are the reciprocal cell lattice vectors and m_i's are all integers. The expansion in (2.39) is an infinite sum over all integer reciprocal vectors. To represent this series in a computer, it must be truncated at a certain point. The kinetic energy of each plane wave of the form $e^{i(\mathbf{k}+\mathbf{G}).\mathbf{r}}$ is given by,

$$E = \frac{\hbar^2}{2m}|\mathbf{k}+\mathbf{G}|^2 \tag{2.40}$$

Therefore as **G** increases, so does the kinetic energy of the plane waves, implying they become more and more rapidly oscillatory. This makes plane waves with very high kinetic energy less important. Therefore in a practical calculation, series like (2.39) is truncated

to include only terms with kinetic energies less than some predefined value ,

$$E_{cut} = \frac{\hbar^2}{2m} G_{cut}^2 \tag{2.41}$$

so that the infinite series in (2.39) is replaced by the following finite sum,

$$\phi_{\mathbf{k}}(\mathbf{r}) = \sum_{|\mathbf{G}+\mathbf{k}|<G_{cut}} C_{\mathbf{K}+\mathbf{G}} e^{i(\mathbf{k}+\mathbf{G}).\mathbf{r}} \tag{2.42}$$

In any DFT calculation one therefore needs to be supplied with the parameter the cutoff energy, E_{cut}. Of course, more the terms of the infinite series (2.39) that are kept in the truncated series (2.42), more accurate the results will be. It is recommended to determine the value of the cutoff energy, E_{cut} by observing the change in energy as this value is changing. One example is shown in the fig: 2.3 where E_{cut} of 700 eV the energy variation is negligible.

2.4.4 Projector Augmented Wave Approximation

In a DFT calculation of a real material the expansion of the core electronic states is computationally expensive as very large number of plane waves are require to include them due to high kinetic energy of core electrons. However from the physical point of view, the core electrons do not play active role in determining the properties of a materials as they are hardly effected by the surrounding environment of an atom. Therefore, instead of doing an all electron computation, it is much less burden on the computational resources to somehow consider the core states to be frozen and use an effective potential due to the repulsion of the core states on the valence electrons. This effective potential, known as pseudopotential, is shown schematically in fig: 2.4. A cutoff radius is defined so that the rapidly oscillating wave function of electrons less than this cutoff is smoothed out

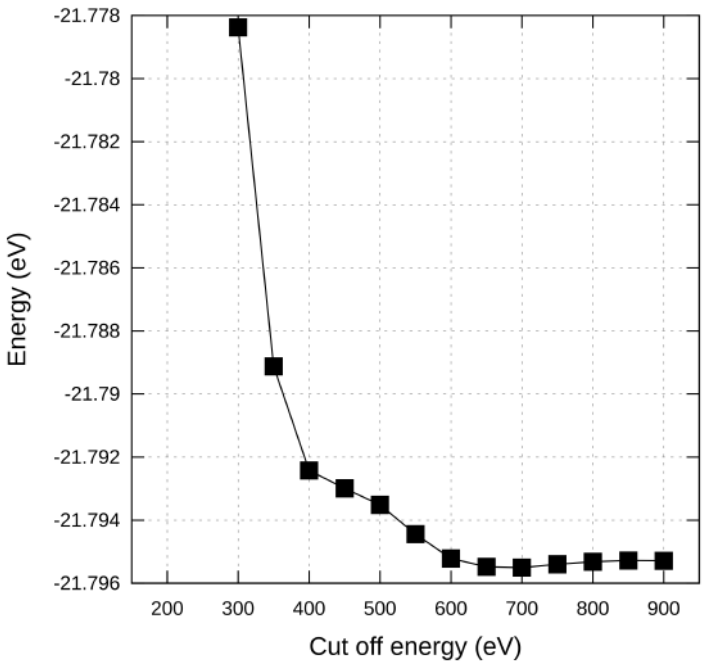

Figure 2.3: The energy of monolayer MoS_2 is shown for different values of the cut off energy. For a cut off energy of 700 eV or more the solution is well converged.

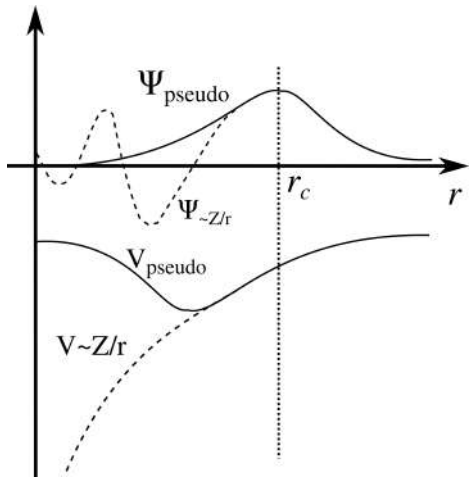

Figure 2.4: Comparison between true potential and a wave function of the core electron states trapped in the nuclear Coulomb potential (dashed line) to the smooth pseudo potential (solid lines). Above the cutoff radius r_c true potential and pseudopotentials match exactly.

depicting the core electrons to be frozen.

Another development within the frozen core approximation is called the projector augmented wave (PAW) method. It was introduced by Blöchl [28] and adapted later for plane wave DFT calculations by Kresse and Joubert [29]. In this method, all electron wave function is constructed using a combination of smooth functions extending throughout space and contributions from muffin tin orbitals around each atom[30]. Consequently, the total wave function is given as,

$$\psi_j^v(r) = \tilde{\psi}_j^v(r) + \sum_i (|\phi_i\rangle - |\tilde{\phi}_i\rangle)\langle p_i|\tilde{\phi}_j\rangle \tag{2.43}$$

Where, $\tilde{\psi}_j^v(r)$ are the valence wave functions, $|\phi_i\rangle$ are all-electron partial waves, $|\phi_i\rangle$ are pseudo partial waves and p_i's are set of projector operators satisfying, $\langle p_i|\tilde{\phi}_j\rangle = \delta_{i,j}$. The index i or j represents atomic sites. The all electron charge density is given for the wave function

(2.43),

$$n(\mathbf{r}) = \tilde{n}(\mathbf{r}) + n^1(\mathbf{r}) - \tilde{n}^1(\mathbf{r}) \tag{2.44}$$

With each term is defined as,

$$\begin{aligned}
\tilde{n}(\mathbf{r}) &= \sum_i f_i \left|\tilde{\psi}_i(\mathbf{r})\right|^2 \\
n^1(\mathbf{r}) &= \sum_i f_i \sum_{j,k} \left\langle \tilde{\psi}_i \mid \tilde{p}_j \right\rangle \phi_j(\mathbf{r})\phi_k(\mathbf{r}) \left\langle \tilde{p}_k \mid \tilde{\psi}_i \right\rangle \\
\tilde{n}^1(\mathbf{r}) &= \sum f_i \sum \left\langle \tilde{\psi}_i \mid \tilde{p}_j \right\rangle \tilde{\phi}_j(\mathbf{r})\tilde{\phi}_k(\mathbf{r}) \left\langle \tilde{p}_k \mid \tilde{\psi}_i \right\rangle
\end{aligned} \tag{2.45}$$

Where, $\tilde{n}(\mathbf{r})$ is the pseudo-charge density obtained from the pseudo-wave functions in plane wave basis. $n^1(\mathbf{r})$ and $\tilde{n}^1(\mathbf{r})$ are respectively the all electron and pseudo charge densities localized within the augmented sphere around each atom.

2.5 Model Hamiltonian

The density functional theory, formulated so far, have been proved to be immensely successful in describing real solids quite accurately. However, it is often the case in physics that the main interest lies not so much in the results of an accurate calculation, but in some simplified representation of the material that will furnish physical understanding of the system. In such a situation tight-binding methods described below will be used. Although not as accurate as DFT, one can arrive at physical understanding of a system with much less computation power.

2.5.1 Tight Binding Method

Consider a system consisting of atoms indexed by μ located at positions $\boldsymbol{\tau}_\mu$. The central ides is to choose atom-like orbitals $\varphi_{\mu\alpha}$

on site μ, and α runs over the orbitals on a given atom. These orbitals are generally be of the form of a radial function multiplied with appropriate spherical harmonics ($Y_{lm}(\theta, \phi)$). The basis consists of total number of orbitals, M is given by product of no. of atoms and orbitals at each site. Introducing a new index $j = \{\mu\alpha\}$ for all M localized orbitals, the trial wave function is written as

$$\psi_n(\mathbf{r}) = \sum_j C_{nj}\varphi_j\left(\mathbf{r} - \boldsymbol{\tau}_j\right) \tag{2.46}$$

where, C_{nj} is the expansion coefficients of the n^{th} eigen state on the j^{th} basis orbital. The objective is to determine these coefficients. Plugging this into the Schrödinger equation, $H\left|\psi_n\right\rangle = E_n\left|\psi_n\right\rangle$, the solutions are obtained by solving the equation,

$$\left(H - E_n S\right) C_n = 0 \tag{2.47}$$

where E_n is the eigen value associated with the n^{th} eigen state. The matrices H and S, given by,

$$\begin{aligned} H_{ij} &= \langle\varphi_i|H|\varphi_j\rangle \\ S_{ij} &= \langle\varphi_i \mid \varphi_j\rangle \end{aligned} \tag{2.48}$$

are $M \times M$ matrices and C_n is the M-component column vector consists of C_{nj}. The diagonal elements of the Hamiltonian matrix, H are called "site energies" denoting the energy of electron occupying that particular site while the off-diagonal terms are called "hopping matrix elements" denoting the hopping of intersite electrons. On the other hand the S matrix is called the "overlap matrix". Equation (2.48) is a general eigenvalue problem that can be solved using standard disorganization techniques. Using the solution C_{nj}, the wave function (2.46) can be obtained.

2.5.2 Periodicity of the Crystal

One approach to the tight binding model Hamiltonian is commonly known as the empirical tight binding, where the objective is to construct a model by focusing only on the basis orbitals, φ_j, required to describe the valence and low-lying conduction states of a solid. However, the orbitals are never explicitly constructed, but the Hamiltonian and overlap matrix in (2.48) are parametrized. Only nearest-neighbor (or depending on the requirement sometimes second neighbor) electron hopping is considered and the orbitals are chosen to be orthogonal to make the overlap matrix a unit matrix.

In a periodic 3D solid crystal, the atom-like orbitals are also indexed by lattice vector $\mathbf{R}$

$$\phi_{\mathbf{R}j}(\mathbf{r}) = \varphi_j\left(\mathbf{r} - \mathbf{R} - \boldsymbol{\tau}_j\right) \tag{2.49}$$

Where j runs over the M orbitals in the cell as before. The orbitals are assumed to follow orthonormality,

$$\langle \phi_{\mathbf{R}i} \mid \phi_{\mathbf{R}'j} \rangle = \delta_{\mathbf{R}\mathbf{R}'}\delta_{ij},$$

and notice that the position matrix will be form,

$$\langle \phi_{\mathbf{R}i} | \mathbf{r} | \phi_{\mathbf{R}'j} \rangle = \left(\mathbf{R} + \boldsymbol{\tau}_j\right)\delta_{\mathbf{R}\mathbf{R}'}\delta_{ij}.$$

The Hamiltonian matrix elements are defined via

$$H_{ij}(\mathbf{R}) = \langle \phi_{\mathbf{R}'i} | H | \phi_{\mathbf{R}'+\mathbf{R}'j} \rangle = \left\langle \phi_{\mathbf{0}i} | H | \phi_{\mathbf{R}_j} \right\rangle$$

where $\mathbf{R}$ now represents a relative lattice vector and the matrix elements represents a hopping from orbital j in cell $\mathbf{R}' + \mathbf{R}$ to orbital i in cell $\mathbf{R}'$ which is equivalent to the hopping from orbital j in cell $\mathbf{R}$ to orbital i in the home unit cell denoted by $\mathbf{R} = 0$.

2.5.3 Tight Binding Hamiltonian in Bloch Like Basis

The tight binding Hamiltonian can be transformed to a Bloch function basis and a corresponding momentum space matrix is obtained as follows.

The Block like basis is constructed as

$$|\chi_j^{\mathbf{k}}\rangle = \sum_{\mathbf{R}} e^{i\mathbf{k}.(\mathbf{R}+\boldsymbol{\tau}_j)} |\phi_{\mathbf{R}j}\rangle \tag{2.50}$$

The Bloch function is expanded as,

$$|\psi_{n\mathbf{k}}\rangle = \sum_j C_j^{n\mathbf{k}} |\chi_j^{\mathbf{k}}\rangle \tag{2.51}$$

and the Hamiltonian matrix, expressed in terms of the Bloch-like basis functions $\langle\chi_i^{\mathbf{k}}|H|\chi_j^{\mathbf{k}}\rangle$ is given by,

$$H_{ij}^{\mathbf{k}} = \sum_R e^{i\mathbf{k}.(\mathbf{R}+\boldsymbol{\tau}_j-\boldsymbol{\tau}_i)} H_{ij}(\mathbf{R}) \tag{2.52}$$

and in this case, the eigenvalue equation becomes,

$$H_{\mathbf{k}} C_{n\mathbf{k}} = E_{n\mathbf{k}} C_{n\mathbf{k}} \tag{2.53}$$

Standard numerical packages are employed to solve this eigenvalue problem to obtain the tight-binding solution for the energy eigenvalues and eigenvectors.

2.6 Wannier Functions

So far the electronic states in a periodic solid have been discussed in terms of Bloch states. However, an alternate viewpoint is to represent an electron band in a periodic solid by a lattice of real space functions that are defined to be the Fourier transformation of the extended Bloch states. These Fourier transforms of Bloch states, known as

Wannier functions [31], are well localised and form a complete basis just like the Bloch states themselves. Therefore, these functions are crucial to give a tight binding approximation for a material which then can be used to extract various observable.

Let, the energy band $E_n(\mathbf{k})$ introduced at (2.53) be a smooth and periodic function of $\mathbf{k}$ in 3D reciprocal space. Its Fourier transform to real space is defined by the following integral as

$$E_{n\mathbf{R}} = \frac{V_{cell}}{(2\pi)^3} \int_{BZ} e^{-i\mathbf{k}.\mathbf{R}} E_{nk} d\mathbf{k} \tag{2.54}$$

Since, $E_n(\mathbf{k})$ is smooth in reciprocal space, $E_n(\mathbf{R})$ is expected to be large only for a few lattice vectors $\mathbf{R}$ near the origin, and to decay rapidly with increasing $|\mathbf{R}|$. The inverse Fourier transformation can be defined as discrete sum over lattice vectors as,

$$E_{n\mathbf{k}} = \sum_{\mathbf{R}} e^{i\mathbf{k}.\mathbf{R}} E_{n\mathbf{R}} \tag{2.55}$$

Similarly, the Fourier transformation of the associated Bloch function given by

$$|w_{n\mathbf{R}}\rangle = \frac{V_{cell}}{(2\pi)^3} \int_{BZ} e^{-i\mathbf{k}.\mathbf{R}} |\psi_{n\mathbf{k}}\rangle d\mathbf{k} \tag{2.56}$$

This is considered to be the definition of the Wannier function associated with band indexed by n. The inverse Fourier transform will of course again be given by a discrete sum over real space lattice vector $\mathbf{R}$,

$$|\psi_{n\mathbf{k}}\rangle = \sum_{\mathbf{R}} e^{i\mathbf{k}.\mathbf{R}} |w_{n\mathbf{R}}\rangle \tag{2.57}$$

2.6.1 Properties of the Wannier Functions

A few important properties[32] of these Wannier functions are,

1. The Wannier functions are localized in real space, i.e.

$$|w_{n\mathbf{R}}(\mathbf{r})\rangle \to 0 \text{ as } |\mathbf{r}-\mathbf{R}| \text{ gets large .} \tag{2.58}$$

2. The Wannier functions are translational images of one another, i.e

$$|w_{n\mathbf{R}}(\mathbf{r})\rangle = |w_{n\mathbf{0}}(\mathbf{r}-\mathbf{R})\rangle \tag{2.59}$$

3. The Wannier functions are orthonormal and complete just like the Bloch states from which they are constructed from,

$$\begin{aligned} &\text{Orthonormality :} && \langle w_{n\mathbf{R}}|w_{n\mathbf{R}'}\rangle = \delta_{\mathbf{R}\mathbf{R}'} \\ &\text{Completeness :} && \frac{V_{cell}}{(2\pi)^3}\int_{BZ}|\psi_{n\mathbf{k}}\rangle\langle\psi_{n\mathbf{k}}|d\mathbf{k} = \sum_{\mathbf{R}}|w_{n\mathbf{R}}\rangle\langle w_{n\mathbf{R}}| \end{aligned} \tag{2.60}$$

4. The Hamiltonian matrix elements between different Wannier functions are band diagonal and the diagonal terms are Fourier transform of band energies defined in (2.54).

$$\langle w_{n\mathbf{0}}|H|w_{n\mathbf{R}}\rangle = E_{n\mathbf{R}} \tag{2.61}$$

2.6.2 Tight Binding Hamiltonian With Wannier Functions

Equation (2.61) is a remarkable property as it implies an exact tight binding representation of the bands $E_{n\mathbf{K}}$ is provided by the Wannier functions. This can be also understood from the fact that the tight binding Hamiltonian in k-space in equation (2.52)and the inverse Fourier transform in equation (2.55) are related by unitary transformation. Therefore, for a system with one orbital per unit cell, the onsite energy will be given by, $E_{n\mathbf{0}}$ and the hopping to its neighboring cell $\mathbf{R}$ will be given by $E_{n\mathbf{R}}$. As the Wannier functions are localized in real space, the hopping elements decay quickly so that the tight binding approximation can be is neighbours. The method to reproduce accurate band structures from a Wannierized tight-binding Hamiltonian is referred to as Wannier interpolation.

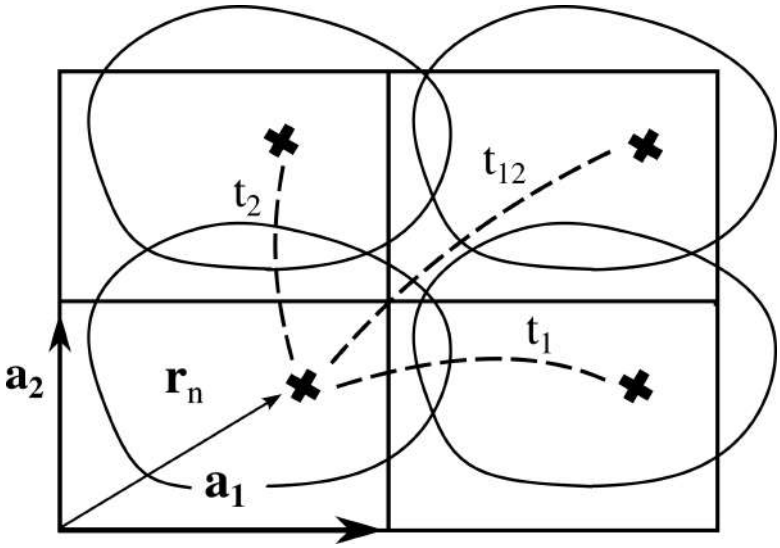

Figure 2.5: Schematic Sketch of four Wannier functions (irregular blobs) out of the infinite lattices for the single band n in 2D with lattice vectors $\boldsymbol{a_1}$ and $\boldsymbol{a_2}$. Cross marks are the Wannier centers in different unit cells. Dashed lines (t_1, t_2 and t_{12}) indicate the hopping between different unit cells of the corresponding tight-binding model

An example of the tight binding model produced by wannier functions is sketched for a 2D crystal in Fig 2.5 The position of the home unit cell ($\mathbf{R} = \mathbf{0}$) Wannier function center, $\overline{\mathbf{r}}_n$ is the cross at lower left cell. The periodic replicas of wannier functions in different unit cells along with the unit cells are also shown. The Hamiltonian matrix elements between Wannier functions are indicated as the dashed lines representing hopping between unit cells are sketched. The diagonal term in the Hamiltonian matrix is the onsite energy of the Wannier function given by $\langle w_{n\mathbf{0}}|H|w_{n\mathbf{0}}\rangle = E_{n\mathbf{0}}$ and the off-diagonal hopping terms shown will be, $t_1 = \langle w_{n\mathbf{0}}|H|w_{n\mathbf{a}_1}\rangle$, $t_2 = \langle w_{n\mathbf{0}}|H|w_{n\mathbf{a}_2}\rangle$ and $t_{12} = \langle w_{n\mathbf{0}}|H|w_{n,\mathbf{a}_1+\mathbf{a}_2}\rangle$. If these hopping terms are only dominant in a system, then the obtained matrix will describe the structure accurately enough. In any case, the more hopping term is included in the Hamiltonian, the more accurate the tight binding Hamiltonian will be.

2.7 Topological Invariants From Tight Binding

So far, density functional theory has been discussed which helps us obtain the ground state properties of a material within the Kohn-Sham formalism. Then, another approach has been discussed that allows us to parametrize the material into a model Hamiltonian to understand important physical properties without giving much attention to the microscopic details of the system. In this context, Wannier functions, introduced in section 2.6 become very useful to obtain a tight binding Hamiltonian of a system. In this section, we shall see how these Wannier functions, constructed by projection onto the Bloch states obtained from DFT calculations, will help us calculating topological invariants of a material. We begin the discussion by introducing some of these invariants. These quantities distinguish different topological classes of materials. Collectively these are named after Michel Berry following his work [33] on the importance of the extra phase acquired by electronic wave function due to any adiabatic transformation, which was otherwise ignored since the genesis of the quantum theory.

2.7.1 Berry Physics of Periodic Solids

For a periodic arrangement of atoms in a solid, the electrons move under the influence of lattice potential obeying same periodicity of the lattice. The wave functions of the electrons are called Bloch functions having the form,

$$|\Psi_{n\boldsymbol{k}}(\boldsymbol{r})\rangle = e^{i\boldsymbol{k}.\boldsymbol{r}}|u_{n\boldsymbol{k}}(\boldsymbol{r})\rangle \tag{2.62}$$

where, $\boldsymbol{k}$ is the crystal momentum, n is the band index of the function $|u_{n\boldsymbol{k}}(\boldsymbol{r})\rangle$ obey same periodicity of the lattice potential i.e. these functions are cell periodic. The Hamiltonian for such a system is also parameterized by crystal momentum due to the lattice trans-

lation being a symmetry of the system. Consequently, Berry phase of a Bloch function is defined in terms of the crystal momentum as,

$$\phi = \oint \langle u_{n\boldsymbol{k}} | i\partial_\mu u_{n\boldsymbol{k}} \rangle \cdot d\boldsymbol{k} \tag{2.63}$$

Where $\partial_\mu = \frac{\partial}{\partial k_\mu}$ with $\mu = \{x, y, z\}$ and the integral is calculated over any closed path in the periodic Brillouin zone. The integrand in (2.63) is called Berry potential or Berry connection, $A_{n\mu}(\boldsymbol{k})$. Writing in a standard vector form using gradient taken in $\boldsymbol{k}$ - space,

$$\boldsymbol{A}_n(\boldsymbol{k}) = \langle u_{n\boldsymbol{k}} | i\nabla_{\boldsymbol{k}} u_{n\boldsymbol{k}} \rangle \tag{2.64}$$

The Berry curvature of the material is then defined as the curl of the Berry connection.

$$\Omega_{n,\mu\nu} = \partial_\mu A_{n,\nu}(\boldsymbol{k}) - \partial_\nu A_{n,\mu}(\boldsymbol{k}) = -2Im[\langle \partial_\mu u_{n\boldsymbol{k}} | \partial_\nu u_{n\boldsymbol{k}} \rangle] \tag{2.65}$$

Berry phase of a Bloch function as defined above in (2.63) depend on the choice of the closed path. The Berry connection not being gauge invariant, depends on the particular gauge choice. However, the Berry curvature is gauge invariant and therefore has a definite value for a given Bloch function. However, the Berry curvature of any material must depend on the symmetry of the original lattice. These symmetry considerations are discussed next.

2.7.2 Symmetry Restriction on Berry Curvature

Crystal symmetry poses following restrictions on the Berry curvature.

- For a crystal with an inversion point present, the Berry curvature is an even function of momentum.

$$\boldsymbol{\Omega}_n(-\boldsymbol{k}) = \boldsymbol{\Omega}_n(\boldsymbol{k}) \tag{2.66}$$

- If time reversal is a symmetry of the crystal then Berry curvature is an odd function of momentum.

$$\boldsymbol{\Omega}_n(-\boldsymbol{k}) = -\boldsymbol{\Omega}_n(\boldsymbol{k}) \tag{2.67}$$

Therefore, for a non magnetic (time reversal symmetric), centro symmetric crystal (inversion symmetric), the Berry curvature must be zero for all momentum. It should be noted that as long as the product of time reversal and inversion is a symmetry of the material, Berry curvature will be zero. If a crystal has other symmetries (for example rotational, reflection, etc.) the Berry curvature will also have the same symmetry.

2.7.3 Berry Curvature From Wannier Functions

In principle one can calculate Berry curvature from the periodic part of the Bloch functions as it has been defined in equation (2.65) and different algorithms and methods have been developed along this way over the years. However, the presence of the derivative operator in equation (2.64) or (2.65) makes the calculation computationally very expensive as one needs to do initial DFT calculation over a very fine grid of $\boldsymbol{K}$ points. Another approach to calculate Berry curvature and Berry connection of Bloch electrons is based on the Wannier functions introduced in section 2.6 which reduce the computational cost significantly. This is based on the idea of Wannier interpolation discussed in section 2.6.

Several properties of Wannier functions have been discussed already in section 2.6.1. However, another remarkable property of the Wannier functions is that the position operator matrix element expressed in the Wannier function basis is given by,

$$\langle w_{n\boldsymbol{0}}|\boldsymbol{r}|w_{n\boldsymbol{R}}\rangle = \boldsymbol{A}_{n\boldsymbol{R}} \tag{2.68}$$

where $A_{n\boldsymbol{R}}$ is the Fourier transform of the Berry connection defined by equation (2.64) as follows,

$$A_{n\boldsymbol{R}} = \frac{V_{cell}}{(2\pi)^3} \int_{BZ} e^{-i\boldsymbol{k}\cdot\boldsymbol{R}} \boldsymbol{A_n}(\boldsymbol{k}) d^3k \tag{2.69}$$

The inverse Fourier transform is usually given by the discrete sum over the lattice sites,

$$\boldsymbol{A_n}(\boldsymbol{k}) = \sum_{\boldsymbol{R}} A_{n\boldsymbol{R}} e^{i\boldsymbol{k}\cdot\boldsymbol{R}} \tag{2.70}$$

Using (2.68) the Berry connection of a Bloch function can be expressed as a sum over the corresponding Wannier functions at different lattice cite as,

$$\boldsymbol{A_n}(\boldsymbol{k}) = \sum_{\boldsymbol{R}} \langle w_{n\boldsymbol{0}} | \boldsymbol{r} | w_{n\boldsymbol{R}} \rangle e^{i\boldsymbol{k}\cdot\boldsymbol{R}} \tag{2.71}$$

Finally, the Berry curvature can be calculated by taking the momentum space curl of the above expression,

$$\boldsymbol{\Omega}_n(\boldsymbol{k}) = i \sum_{\boldsymbol{R}} \langle w_{n\boldsymbol{0}} | \boldsymbol{R} \times \boldsymbol{r} | w_{n\boldsymbol{R}} \rangle e^{i\boldsymbol{k}\cdot\boldsymbol{R}} \tag{2.72}$$

Although at first glance this expression seems useless as the summation is over all possible lattice vector $\boldsymbol{R}$. However, since the Wannier functions are well localized in space, in practice one can construct maximally localised Wannier functions as discussed in section 2.6.2 with the tail of Wannier function at the home unit cell overlapping with very few neighboring unit cells and thereby truncating the infinite sum in equation (2.72) to a few neighboring lattice vector $\boldsymbol{R}$

2.8 Electron Spin and Magnetic Materials

In the discussion so far, the electron spin has not been considered. However in reality electrons are to be treated as spinor. Another

important aspect of different materials that has been studied extensively in this thesis is magnetism which generally arises in solids due to interactions between electron spins. In this section, general methods to manage spin of electrons within the *ab-initio* calculation as well as spin only model Hamiltonian to describe magnetism of solids have been discussed.

2.8.1 Local Spin Density Functional Theory

First, let us assume that any spin mixing term such as spin orbit interaction is absent (or in reality can be safely neglected for material consisting of lighter elements). In this situation up and down spin channels can be treated independently. The Kohn-Sham equations (2.31) can be generalized by attaching spin labels such that spin-up electrons obey

$$\Big[-\frac{\hbar^2}{2m}\nabla^2 + V_{ext} + V_H + V_{XC,\uparrow}\Big]\phi_{i,\uparrow}(\mathbf{r}) = \epsilon_{i,\uparrow}\phi_{i,\uparrow}(\mathbf{r}) \tag{2.73}$$

and the spin down electrons will obey,

$$\Big[-\frac{\hbar^2}{2m}\nabla^2 + V_{ext} + V_H + V_{XC,\downarrow}\Big]\phi_{i,\downarrow}(\mathbf{r}) = \epsilon_{i,\downarrow}\phi_{i,\downarrow}(\mathbf{r}) \tag{2.74}$$

where the total density is now given by,

$$n(\mathbf{r}) = n_\uparrow(\mathbf{r}) + n_\downarrow(\mathbf{r}) \tag{2.75}$$

Note, that the Hartree potential and external potential term will continue to have same functional form as before but the electron density on which they depend will be replaced by $n_\uparrow(\mathbf{r})$ or $n_\uparrow(\mathbf{r})$ for up and down spin channel. A pair of exchange correlation potential for up and down spin electrons are extracted from homogeneous electron gas, but this time a uniform spin polarised electron gas is considered. This theory is known as the local spin-density approximation (LSDA).

For materials without any intrinsic magnetism, up and down spin channel must be identical. In this case, the electrons are treated as though they are spinless, by multiplying a factor of 2 in the right-hand sides of equation (2.17) to account for the electron spin. However, in magnetic materials, time-reversal (TR) symmetry is spontaneously broken. Consequently, the energy of the material gets reduced, relative to a fully spin paired nonmagnetic state, by developing imbalance in the density of up and down spins electrons on some atomic sites. Usually these imbalance creates finite magnetic moments on different sites and consequently develop a well-defined magnetic order to minimize the exchange interactions between them. This mechanism can often be well described at the level of LSDA discussed above.

2.8.2 Spin Orbit Coupling

In the presence of spin orbit interactions, which is a purely relativistic effect arises due to interactions between orbital and spin angular momentum of electron, up and down spin channels mix. Therefore, treating electronic wave function as spinor is unavoidable. This effect be incorporated in the Kohn–Sham equations (2.31) takes the following form,

$$\Big[-\frac{\hbar^2}{2m}\nabla^2 + V_{ext} + V_H + V_{XC} + \boldsymbol{W}_{XC}\cdot\boldsymbol{\sigma} + h_{soc}\Big]\phi_{i,\uparrow}(\mathbf{r}) = \epsilon_{i,\uparrow}\phi_{i,\uparrow}(\mathbf{r}) \tag{2.76}$$

where, V_{XC} and $\boldsymbol{W}_{XC}$ are respectively the scalar and spin-dependent exchange correlation potential and $\boldsymbol{\sigma} = (\sigma_x, \sigma_y, \sigma_z)$ is the vector of spin Pauli matrices. The extra term h_{soc} is incorporates the spin-orbit interactions and written as,

$$h_{soc} = \frac{\hbar}{4m^2c^2}\boldsymbol{\sigma}\cdot\nabla V(\boldsymbol{r})\times\boldsymbol{p} \tag{2.77}$$

where, $V(\boldsymbol{r}) = -e\phi(\boldsymbol{r})$ is the electrostatic potential felt by the electron.

2.8.3 Model Hamiltonian for Magnetism

As discussed in section 2.8.1, in magnetic material imbalance between up and down spin occupation develops in some specific sites to lower the total energies of the systems. The imbalance creates localised magnetic moment in different sites. Often it is customary to construct a model Hamiltonian that incorporates interactions between these localized moments to understand magnetic properties of solids. The basic model Hamiltonian in magnetism, named after Heisenberg, is given by

$$\mathcal{H}_{Heisenberg} = -\frac{1}{2}\sum_{i\neq j} J_{ij}\boldsymbol{S}_i \cdot \boldsymbol{S}_j \tag{2.78}$$

Where $\boldsymbol{S}_i$ or $\boldsymbol{S}_j$ is the spin magnetic moment at site i or j. The exchange interaction between them is denoted by J_{ij} and the multiplicative factor in front is due to compensate the double counting performed by the summation which is performed over all possible pair of localized spin site. In practice, however, the interaction between only a few neighboring site is of significant value and determine the magnetic ground state.

The magnetic ground states is determined by the sign of the exchange interactions. For example in a material where only the nearest neighbor interaction is significant, a positive exchange interaction will make all spin orienting in the same direction ensuring a ferromagnetic ground state whereas a negative exchange interaction will orient spins at the neighboring site in the opposite direction favouring an antiferromagnetic state. However if exchange interactions between sites other than nearest neighbor are of significant value and having

different sign, then the ground states becomes much more complex with possibility of canted spin structure, spin spirals or frustrated magnetic state.

The strength of the exchange interactions determine the ordering temperature for the magnetic material. Therefore in the study of magnetic materials carried out in this thesis, it is of utmost importance that these interactions are calculated preciously. In the coming section one method to extract exchange interactions from DFT calculation of magnetic materials is discussed.

2.8.4 Extraction of Exchange Interactions

There are primarily two ways to acquire the pair exchange energies from the *ab inito* energy calculation. The first method, based on Green function calculation and multiple-scattering theories, is often used with the approximation of infinitesimal rotations of spins[34]. This is a widely used method when calculation of Green function is readily available[35, 36, 37, 38, 39, 40, 41]. However, in this thesis the calculation of the exchange interactions are performed with the second approach, presented in [42] that involves reciprocal space calculations, where the system is confined to specific spin spirals with defined wave vectors $\boldsymbol{q}$. This necessitates noncollinear calculations that can be restricted to the unit cell only using the generalized Bloch theorem[43].

We start by writing the magnetic part of the energy given by Heisenberg Hamiltonian given in equation (2.78) for a solid with pe-

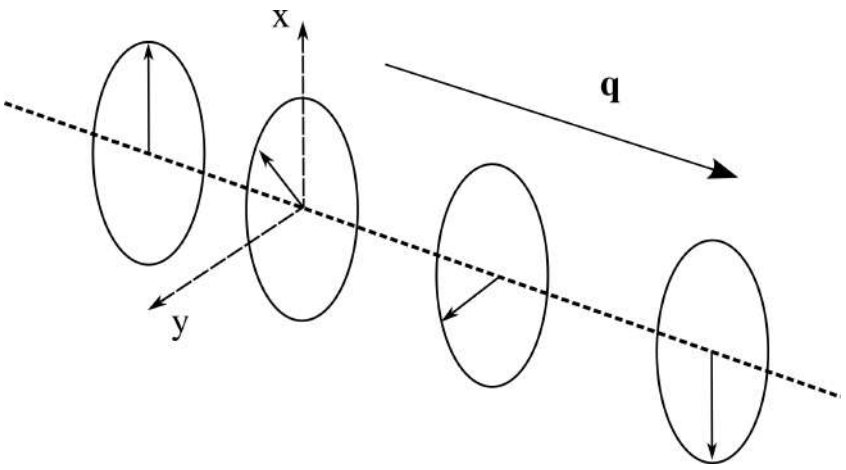

Figure 2.6: Schematic representation of Spin Spiral with propagation vector, $\boldsymbol{q}$, parallel to the z axis. The cone angles for the magnetic moment in this example is $\frac{\pi}{2}$

riodic crystal in the following form,

$$E = -\frac{1}{2} \sum_{\substack{m,n \\ \alpha\beta \\ \boldsymbol{R}_{m\alpha} \neq \boldsymbol{R}_{n\beta}}} J(\boldsymbol{R}_{m\alpha}, \boldsymbol{R}_{n\beta}) \hat{\boldsymbol{s}}_{m\alpha} \cdot \hat{\boldsymbol{s}}_{n\beta} \tag{2.79}$$

where $\boldsymbol{R}_{m\alpha(m\beta)} \equiv \boldsymbol{R}_{m(n)} + \boldsymbol{\tau}_{\alpha(\beta)}$. The lattice vector $\boldsymbol{R}_{m(n)}$ denotes $m^{th}(n^{th})$ unit cell and $\boldsymbol{\tau}_{\alpha(\beta)}$ are the basis vectors that specifies the magnetic atom positions within each unit cell. $\hat{\boldsymbol{s}}_{m\alpha}$ and $\hat{\boldsymbol{s}}_{n\beta}$ are unit vector along the direction of the atomic spin magnetic moments at $\boldsymbol{R}_{m\alpha}$ and $\boldsymbol{R}_{n\beta}$ respectively. The exchange coupling between atoms at these sites are to be calculated and are denoted by $J(\boldsymbol{R}_{m\alpha}, \boldsymbol{R}_{n\beta})$. Note that, the magnitude of the magnetic moments are absorbed into the exchange interactions.

The collective transverse magnetic excitations are approximated by static spin spirals. One example is shown in 2.6 . The magnetic moment at any unit cell is rotated relative to the previous unit cell moment by an angle depending on the propagation vector $\boldsymbol{q}$. The

energy of these spin spirals are calculated using noncollinear DFT calculation that is treating the electronic states as spinor. For the required Fourier and inverse-Fourier transformations, the formalism of Haliov et. al. [44] is followed. For a particular spin spiral with wave vector $\boldsymbol{q}$, the azimuthal angle of $\hat{\boldsymbol{s}}_{n\alpha}$ is given by $\varphi_{n\alpha} = \boldsymbol{q}.R_{n\alpha}$. Therefore, the moment at the position $\boldsymbol{R}_{n\alpha}$ is given by the generalised Bloch theorem as,

$$\hat{\boldsymbol{s}}_{n\alpha} = \begin{pmatrix} sin(\theta_\alpha)cos(\boldsymbol{q}.\boldsymbol{R}_{n\alpha} + \phi_\alpha) \\ sin(\theta_\alpha)sin(\boldsymbol{q}.\boldsymbol{R}_{n\alpha} + \phi_\alpha) \\ cos(\theta_\alpha) \end{pmatrix} \tag{2.80}$$

Where $\boldsymbol{S}_\alpha$ is the moment of the α sub-lattice within the home unit cell. The "cone angle" θ_α is the angle between the rotation axis and the α sub-lattice of magnetic atoms. In the absence of spin orbit interactions, the rotation can be taken around the z-axis without loss of generality. ϕ_α represents some general overall phase factor of the α sub-lattice known as the "phase angle".

using equation (2.80) and the translational invariance of the crystal, the magnetic part of the energy given by equation (2.79) can be written as,

$$E = -\frac{1}{2} \sum_{\substack{\alpha\beta \\ \boldsymbol{R} \\ \boldsymbol{\tau}_\alpha \neq \boldsymbol{\tau}_\beta - \boldsymbol{R}}} J(\boldsymbol{\tau}_\alpha, \boldsymbol{\tau}_\beta - \boldsymbol{R}) \Big\{ sin(\theta_\alpha)sin(\theta_\beta) \times cos[\boldsymbol{q} \cdot (\boldsymbol{\tau}_{\alpha\beta} - \boldsymbol{R}) + (\phi_\alpha - \phi_\beta)] + cos(\theta_\alpha)cos(\theta_\beta) \Big\} \tag{2.81}$$

Where, $\boldsymbol{\tau}_{\alpha\beta} = \boldsymbol{\tau}_\alpha - \boldsymbol{\tau}_\beta$ and $\boldsymbol{R} = \boldsymbol{R_n} - \boldsymbol{R_m}$. The energy E is a function of the wave vectors of the spin-spiral $\boldsymbol{q}$ along with the phase and cone angles of the magnetic moments on all the magnetic atoms of the unit cell. Next we define the Fourier transformation of the

exchange interactions $J(\boldsymbol{\tau}_\alpha, \boldsymbol{\tau}_\beta - \boldsymbol{R})$ to be,

$$J_{\alpha\beta}(\boldsymbol{q}) = \sum_{\boldsymbol{R}} J(\boldsymbol{\tau}_\alpha, \boldsymbol{\tau}_\beta - \boldsymbol{R}) e^{i\boldsymbol{q}\cdot(\boldsymbol{\tau}_{\alpha\beta} - \boldsymbol{R})} \tag{2.82}$$

Using equation (2.82) , the energy in equation (2.81) will be,

$$\begin{aligned} E(\boldsymbol{q}, \Theta, \Phi) = -\frac{1}{2} \sum_{\alpha\beta} \Big[& sin(\theta_\alpha) sin(\theta_\beta) Re\{J_{\alpha\beta}(\boldsymbol{q}) e^{i(\phi_\alpha - \phi_\beta)}\} \\ & + cos(\theta_\alpha) cos(\theta_\beta) J_{\alpha\beta}(\boldsymbol{0}) \Big] \end{aligned} \tag{2.83}$$

Where the dependence of the energy on the wave vector, phase angles and cone angle are shown explicitly. Θ and Φ collectively represents cone and phase angle of all the moments respectively.

Symmetries of Exchange Interactions

Equation (2.83) relates the energy corresponding to the magnetic part with the Fourier transformed pair exchange interactions $J_{\alpha\beta(\boldsymbol{q})}$. Before discussing the calculation scheme for real materials, let us consider various symmetry relations followed by $J_{\alpha\beta(\boldsymbol{q})}$ to be able to reduce no of DFT calculation. The symmetry conditions are,

1. $J_{\alpha\beta}(\boldsymbol{q}) = J_{\beta\alpha}(-\boldsymbol{q})$
2. $Re[J_{\alpha\beta}(\boldsymbol{q})] = Re[J_{\alpha\beta}(-\boldsymbol{q})]$
3. $Im[J_{\alpha\beta}(\boldsymbol{q})] = -Im[J_{\alpha\beta}(-\boldsymbol{q})]$. Two corollary follow from this condition.
   (a) $Im[J_{\alpha\beta}(\boldsymbol{0})] = 0$
   (b) $Im[J_{\alpha\alpha}(\boldsymbol{q})] = 0$
4. $J_{\alpha\beta}(\hat{C}\boldsymbol{q}) = J_{\alpha'\beta'}(\boldsymbol{q})$ Where $\hat{C}$ is any group symmetry obeyed by the lattice and sites denoted by α' and β' are related to the lattice sites α and β by the action of the operator $\hat{C}$ i.e. $\hat{C}\boldsymbol{\tau}_{\alpha'} + \boldsymbol{R} = \tau_\alpha$ for some lattice vector $\boldsymbol{R}$.

These symmetry relations imply that spin spiral state with wave vector $\boldsymbol{q}$ from the irreducible part of the Brillouin zone is needed to be calculated. $J_{\alpha\beta}(\boldsymbol{q})$ in the rest of the Brillouin zone can be obtained using symmetry relations.

Calculation Scheme

For calculation of the Fourier transformation $J_{\alpha\beta}(\boldsymbol{q})$ two different situation must be considered.

Single Magnetic Atom per Unit Cell In this case only one sub-lattice is present meaning only one sub-lattice index is required. Letting the cone angle of the moment be θ_α and the the spin spiral running through the magnetic atom in different unit cells, equation (2.83) simplifies in this case to,

$$J_{\alpha\alpha}(\boldsymbol{q}) - J_{\alpha\alpha}(\boldsymbol{0}) = -2\frac{E_\alpha(\boldsymbol{q}) - E_\alpha(\boldsymbol{0})}{sin^2(\theta_\alpha)} \tag{2.84}$$

Where the subscript in E denotes on which atom the spin spiral is running.

Multiple Magnetic atoms per Unit Cell In this case, consider the magnetic moments on atoms α and β are tilted by cone angles θ_α and θ_β respectively. The spin spiral runs through the system changes the orientation of magnetic moments on these atoms keeping rest of the moments unchanged. In the absence of the inversion symmetry, the imaginary part of $J_{\alpha\beta(\boldsymbol{q})}$ is non zero. The real and imaginary part can be obtained using equation (2.83) as follows.

$$\begin{aligned} Re\big[J_{\alpha\beta}(\boldsymbol{q})\big] = \frac{1}{sin(\theta_\alpha)sin(\theta_\beta)}\Big\{ & E_{\alpha\beta}\big(\boldsymbol{0}, \frac{\pi}{2}\big) - E_{\alpha\beta}(\boldsymbol{q}, 0) \\ & + E_\alpha(\boldsymbol{q}) - E_\alpha(\boldsymbol{q}) \\ & + E_\beta(\boldsymbol{q}) - E_\beta(\boldsymbol{0})\Big\} \end{aligned} \tag{2.85}$$

$$Im\big[J_{\alpha\beta}(\boldsymbol{q})\big] = \frac{E_{\alpha\beta}\big(\boldsymbol{q}, \frac{\pi}{2}\big) - E_{\alpha\beta}\big(\boldsymbol{q}, 0\big)}{sin(\theta_\alpha)sin(\theta_\beta)} - Re\big[J_{\alpha\beta}(\boldsymbol{q})\big] \tag{2.86}$$

Where, as before the subscript of E indicate on which atom the spin spiral is running and $E_{\alpha\beta}(\boldsymbol{q}, \frac{\pi}{2})$ and $E_{\alpha\beta}(\boldsymbol{q}, 0)$ represent total energies of the spin spiral with propagation vector $\boldsymbol{q}$ and the relative phase angle $\phi_\alpha - \phi_\beta = \frac{\pi}{2}$ and 0 respectively.

Equation (2.84), (2.85) and (2.86) express the Fourier transform of the exchange interaction as difference of the total energies of particular magnetic configurations, provided by the spin spirals. The energies can be obtained from DFT calculation thereby providing $J_{\alpha\beta}(\boldsymbol{q})$. The final step would obviously be to perform an inverse Fourier transformation on these quantities to obtain the real space pair interaction energies. The inverse Fourier transformation would be,

$$J(\boldsymbol{\tau}_\alpha, \boldsymbol{\tau}_\beta - \boldsymbol{R}) = \frac{1}{V_{BZ}} \int_{BZ} J_{\alpha\beta}(\boldsymbol{q}) e^{-i\boldsymbol{q}\cdot(\boldsymbol{\tau}_{\alpha\beta} - \boldsymbol{R})} d^3q \tag{2.87}$$

In practice, of course, a discrete Fourier transformation is performed on the calculated sample space of $J_{\alpha\beta}(\boldsymbol{q})$.

Bibliography

[1] M. Born and R. Oppenheimer. Zur quantentheorie der molekeln. *Annalen der Physik*, 389(20):457–484, 1927.

[2] J. C. Slater. The Theory of Complex Spectra. *Physical Review*, 34(10):1293–1322, November 1929.

[3] Douglas Rayner Hartree and W. Hartree. Self-consistent field, with exchange, for beryllium. *Proceedings of the Royal Soci-*

ety of London. Series A - Mathematical and Physical Sciences, 150(869):9–33, 1935.

[4] Valerio Magnasco. *Post-Hartree–Fock Methods*, chapter 8, pages 133–139. John Wiley and Sons, Ltd, 2009.

[5] W. Kohn. Nobel lecture: Electronic structure of matter—wave functions and density functionals. *Rev. Mod. Phys.*, 71:1253–1266, Oct 1999.

[6] P. Hohenberg and W. Kohn. Inhomogeneous electron gas. *Phys. Rev.*, 136:B864–B871, Nov 1964.

[7] Wolfram Koch and Max C. Holthausen. *Electron Density and Hole Functions*, chapter 2, pages 19–28. John Wiley and Sons, Ltd, 2001.

[8] D. R. Hartree. The wave mechanics of an atom with a non-coulomb central field. part i. theory and methods. *Mathematical Proceedings of the Cambridge Philosophical Society*, 24(1):89–110, 1928.

[9] W. Kohn and L. J. Sham. Self-consistent equations including exchange and correlation effects. *Phys. Rev.*, 140:A1133–A1138, Nov 1965.

[10] P. A. M. Dirac. Note on exchange phenomena in the thomas atom. *Mathematical Proceedings of the Cambridge Philosophical Society*, 26(3):376–385, 1930.

[11] J. C. Slater. A simplification of the hartree-fock method. *Phys. Rev.*, 81:385–390, Feb 1951.

[12] Murray Gell-Mann and Keith A. Brueckner. Correlation energy of an electron gas at high density. *Phys. Rev.*, 106:364–368, Apr 1957.

[13] Jerzy Cioslowski, Paul Ziesche, and Katarzyna Pernal. Description of a high-density homogeneous electron gas with the Yasuda density matrix functional. *The Journal of Chemical Physics*, 115(19):8725–8730, 11 2001.

[14] W. J. Carr and A. A. Maradudin. Ground-state energy of a high-density electron gas. *Phys. Rev.*, 133:A371–A374, Jan 1964.

[15] E. Wigner. Effects of the electron interaction on the energy levels of electrons in metals. *Trans. Faraday Soc.*, 34:678–685, 1938.

[16] W. J. Carr. Energy, specific heat, and magnetic properties of the low-density electron gas. *Phys. Rev.*, 122:1437–1446, Jun 1961.

[17] E. Wigner. On the interaction of electrons in metals. *Phys. Rev.*, 46:1002–1011, Dec 1934.

[18] D. M. Ceperley and B. J. Alder. Ground state of the electron gas by a stochastic method. *Phys. Rev. Lett.*, 45:566–569, Aug 1980.

[19] John P. Perdew. Accurate density functional for the energy: Real-space cutoff of the gradient expansion for the exchange hole. *Phys. Rev. Lett.*, 55:2370–2370, Nov 1985.

[20] John P. Perdew and Yue Wang. Accurate and simple analytic representation of the electron-gas correlation energy. *Phys. Rev. B*, 45:13244–13249, Jun 1992.

[21] A. D. Becke. Density-functional exchange-energy approximation with correct asymptotic behavior. *Phys. Rev. A*, 38:3098–3100, Sep 1988.

[22] Chengteh Lee, Weitao Yang, and Robert G. Parr. Development of the colle-salvetti correlation-energy formula into a functional of the electron density. *Phys. Rev. B*, 37:785–789, Jan 1988.

[23] Axel D. Becke. Density-functional thermochemistry. I. The effect of the exchange-only gradient correction. *The Journal of Chemical Physics*, 96(3):2155–2160, 02 1992.

[24] John P. Perdew, Kieron Burke, and Matthias Ernzerhof. Generalized gradient approximation made simple. *Phys. Rev. Lett.*, 77:3865–3868, Oct 1996.

[25] Hendrik J. Monkhorst and James D. Pack. Special points for brillouin-zone integrations. *Phys. Rev. B*, 13:5188–5192, Jun 1976.

[26] M. Methfessel and A. T. Paxton. High-precision sampling for brillouin-zone integration in metals. *Phys. Rev. B*, 40:3616–3621, Aug 1989.

[27] Peter E. Blöchl, O. Jepsen, and O. K. Andersen. Improved tetrahedron method for brillouin-zone integrations. *Phys. Rev. B*, 49:16223–16233, Jun 1994.

[28] P. E. Blöchl. Projector augmented-wave method. *Phys. Rev. B*, 50:17953–17979, Dec 1994.

[29] G. Kresse and D. Joubert. From ultrasoft pseudopotentials to the projector augmented-wave method. *Phys. Rev. B*, 59:1758–1775, Jan 1999.

[30] O. K. Andersen and R. V. Kasowski. Electronic states as linear combinations of muffin-tin orbitals. *Phys. Rev. B*, 4:1064–1069, Aug 1971.

[31] Gregory H. Wannier. The structure of electronic excitation levels in insulating crystals. *Phys. Rev.*, 52:191–197, Aug 1937.

[32] E.I. Blount. Formalisms of band theory. In Frederick Seitz and David Turnbull, editors, *Formalisms of Band Theory*, volume 13 of *Solid State Physics*, pages 305–373. Academic Press, 1962.

[33] Michael Victor Berry. Quantal phase factors accompanying adiabatic changes. *Proceedings of the Royal Society of London. A. Mathematical and Physical Sciences*, 392(1802):45–57, 1984.

[34] A.I. Liechtenstein, M.I. Katsnelson, V.P. Antropov, and V.A. Gubanov. Local spin density functional approach to the theory of exchange interactions in ferromagnetic metals and alloys. *Journal of Magnetism and Magnetic Materials*, 67(1):65–74, 1987.

[35] M. I. Katsnelson and A. I. Lichtenstein. First-principles calculations of magnetic interactions in correlated systems. *Phys. Rev. B*, 61:8906–8912, Apr 2000.

[36] J. Rusz, L. Bergqvist, J. Kudrnovský, and I. Turek. Exchange interactions and curie temperatures in ni_{2-x}MnSb alloys: First-principles study. *Phys. Rev. B*, 73:214412, Jun 2006.

[37] A. V. Ruban, S. Khmelevskyi, P. Mohn, and B. Johansson. Temperature-induced longitudinal spin fluctuations in fe and ni. *Phys. Rev. B*, 75:054402, Feb 2007.

[38] S. Polesya, S. Mankovsky, O. Sipr, W. Meindl, C. Strunk, and H. Ebert. Finite-temperature magnetism of fe_xpd_{1-x} and co_xpt_{1-x} alloys. *Phys. Rev. B*, 82:214409, Dec 2010.

[39] S. Frota-Pessôa, R. B. Muniz, and J. Kudrnovský. Exchange coupling in transition-metal ferromagnets. *Phys. Rev. B*, 62:5293–5296, Sep 2000.

[40] L. Szunyogh, L. Udvardi, J. Jackson, U. Nowak, and R. Chantrell. Atomistic spin model based on a spin-cluster expansion technique: Application to the $irmn_3$/co interface. *Phys. Rev. B*, 83:024401, Jan 2011.

[41] M. dos Santos Dias, J. B. Staunton, A. Deak, and L. Szunyogh. Anisotropic spin-spin correlations in $mn_1/x(111)$ (x = pd, pt, ag, and au). *Phys. Rev. B*, 83:054435, Feb 2011.

[42] Marjana Ležaić, Phivos Mavropoulos, Gustav Bihlmayer, and Stefan Blügel. Exchange interactions and local-moment fluctuation corrections in ferromagnets at finite temperatures based on noncollinear density-functional calculations. *Phys. Rev. B*, 88:134403, Oct 2013.

[43] L. M. Sandratskii. Energy band structure calculations for crystals with spiral magnetic structure. *physica status solidi (b)*, 136(1):167–180, 1986.

[44] S. V. Halilov, H. Eschrig, A. Y. Perlov, and P. M. Oppeneer. Adiabatic spin dynamics from spin-density-functional theory: Application to fe, co, and ni. *Phys. Rev. B*, 58:293–302, Jul 1998.

Part II

Materials With 2D Crystal Lattices

CHAPTER 3

Insulating Ground State of 1H TMDCs

"With four parameters I can fit an elephant, and with five I can make him wiggle his trunk."

von Neumann

3.1 Introduction

Mo or W based transition metal dichalcogenides have attracted lot of interest in the growing field of 2D materials [1]. Various electronic ground state has been reported depending on the different arrangement of chalcogen atoms (S,Se or Te) around the transition metal (Mo or W) atoms. The most stable polymorph, known as 1H phase, has six chalcogens forming a trigonal biprismatic coordination around the metal atom [2]. In the 1H phase, these TMDCs are direct bandgap semiconductors with the valence band maximum (VBM) and conduction band minimum (CBM) both at the K point of the Brillouin zone. The insulating phase is believed to be between the d states of the transition metal originating from the crystal field effects of the chalcogen. Due to the crystal field effects, the lowest energy d_{z^2} state becomes fully occupied and the gap is in between occupied d_{z^2} and unoccupied d_{xy} and $d_{x^2-y^2}$.

Description of the low energy physics in these materials have been modelled considering the interactions between d states [3]. However, looking closely at the orbital character of the valence band top and conduction band bottom across the Brillouin zone one finds that, at Γ point, the valence band is comprised of the d_{z^2} states and the conduction band bottom has $d_{x^2-y^2}$ and d_{xy} character while at the K point the VBM is comprised of the in plane d states and the out of plane d_{z^2} states contribute to the CBM. Such level reversal while the system remains insulating is puzzling. There are two hopping pathways for the d electrons, one is the direct hopping between d states on different transition metal atom and the other pathway is via the chalcogen p states. Therefore a detail study on the effect of the direct and indirect hopping of the d electrons on the valence and conduction bands is crucial in the description of the low energy physics in these materials. Since, in the previous studies, model Hamiltonian with d bands only has been constructed, a more detailed study is necessary which will not only help us understand how level reversal become possible in a insulating system but also shed light on the contribution from various hopping pathways.

In this project, with an aim to understand the insulating phase in 1H Mo and W based TMDCs, we have performed *ab initio* calculations and mapped the results onto a tight binding model. Taking MoS_2 as typical example of this family, we have shown by calculating tight binding Hamiltonian matrix elements under two centre approximation, that within a d only model, one can not simultaneously describe the insulating gap and correct energetic ordering of different orbitals. Previously it has been shown, that including distant (second and third) transition metal neighbor the low energy bands can be produced within a d only model. However our calculation will show that this fitting of low energy bands using distant neighbor

hopping comes at the expense of the physical meaning of the hopping parameters. We shall show that within the first neighbor model itself, including hopping of d electrons via the S-p states gives a reasonable fit of the low energy band structure.

3.2 Computational Methods

The *ab-initio* electronic structure is calculated within a projector augmented-wave method implementation [4, 5] of density functional theory (DFT) [6] within the Vienna Ab-initio Simulation Package(VASP) [7, 8, 9]. The monolayer is formed by taking the bulk MoS_2 structure with experimental lattice parameters [10] $a = 3.16$ Å and $c = 12.29$ Å and adding a vacuum of 20 Å in the c direction. The added vacuum to the lattice constant in the c direction ensures that the interactions between images of periodic supercells imposed by the method we use are negligible. The atom positions are optimized to reduce the forces acting on the atom to lie below the tolerance value of 5 meV. Perdew-Burke-Ernzerhof potentials were used for the exchange correlation functional. For the self-consistent calculation for monolayer MoS_2, a k-space grid of $8 \times 8 \times 1$ was used. The cutoff energy for the plane wave basis was taken to be 600 eV. The tight binding Hamiltonian is constructed by calculating maximally localized Wannier function [11, 12] using WANNIER90 code [13]. The basis of the model Hamiltonian consists of the p orbitals of S and d orbitals of Mo atoms. The spread of the Wannier functions are found to be less than 2.0 $Å^2$ implying that Wannier functions are good representation of atomic orbitals.

3.3 Results and Discussion

3.3.1 Deviation From Crystal Field Effects

The structure of monolayer MoS_2 in 2H polymorph is shown in Fig. 3.1 a. The central Mo layer is sandwiched between two S layers. Three S atoms in top and bottom layer sit on top of each other making a trigonal bi-prismatic coordination. The nearest neighbor distance between Mo and S atoms are 2.41 Å. The distance between two neighboring Mo atoms is 3.16 Å. Mo-S-Mo angle is 82^0. The schematic in the Fig: 3.1 b shows the expected ordering of the d orbitals of Mo due to crystal field effects. d_{z^2} is the lowest energy orbital which is expected to be filled with two valence electrons of Mo and the next higher energy d orbitals are d_{xy} and $d_{x^2-y^2}$ which are expected to be unoccupied. This simple picture describes the presence of the band-gap. The calculated electronic band structure of monolayer 2H MoS_2 is shown in Fig. 3.1 c. Both the VBM and the CBM are at the K point of the 2D Brillouin zone, making it a direct band-gap material. The calculated band gap is 1.76 eV which matches well with previous studies.

To probe the orbital character of the valence band top and conduction band bottom across the 2D Brillouin zone, we have projected the eigenfunctions onto the orbital basis. The orbital projected band structure is shown in Fig. 3.2a. The length of the vertical red and blue lines respectively denotes the relative contribution of $d_{xy}, d_{x^2-y^2}$ and d_{z^2} orbitals to the band at the particular crystal momentum. The VBM at the K point comprises of $d_{x^2-y^2}$ and d_{xy} states whereas the CBM has prominent d_{z^2} character. This is in contradiction to the crystal field description of the levels discussed earlier.

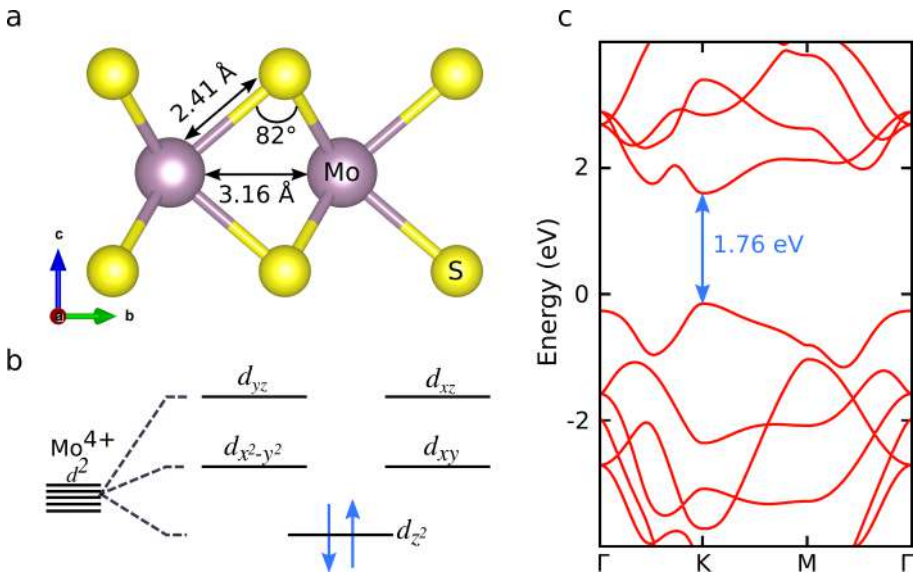

Figure 3.1: (a) Trigonal biprismatic arrangements of S atoms around Mo atoms in monolayer 1H MoS_2.(b) Crystal field effect of S atoms lifts five fold degeneracy of Mo-d orbitals (c) Electronic band structure of MoS_2 along different high symmetry direction of the Brillouin zone

In earlier studies in the literature on the low energy physics of MoS_2, the main focus has been on this particular ordering at K point. However, at the Γ the VBM is comprised of d_{z^2} states and the in plane orbitals $d_{x^2-y^2}$ and d_{xy} contribute to the conduction band. This level reversal of valence band and conduction band between Γ and K is surprising as the material remains insulating throughout the $\Gamma - K$ direction. Evidently a better low energy description is required that will not only capture the gap throughout the Brillouin zone but also shed light on the level reversal between the d orbitals maintaining the insulating character.

3.3.2 Effect of Direct $d-d$ Interactions

To analyse the insulating state and contribution from different hopping pathways, we have mapped the *ab initio* band structure

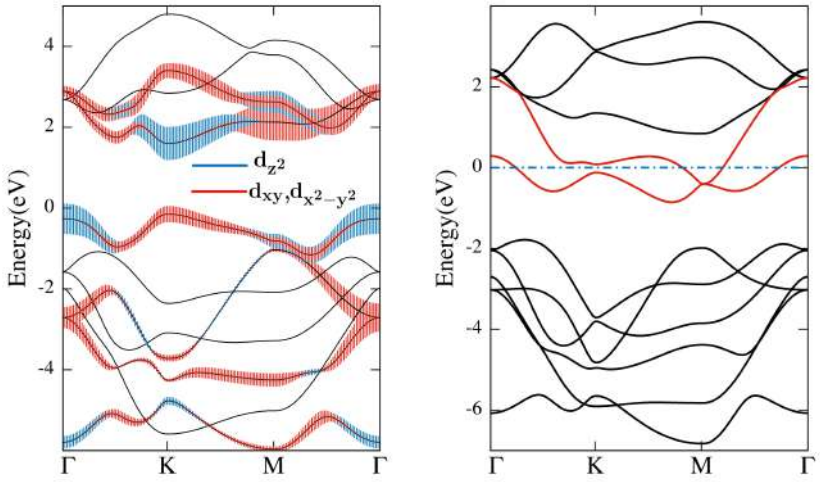

Figure 3.2: (a) Orbital projected electronic band structure of monolayer of 2H MoS_2 (b) Band structure 2H MoS_2 after switching off second neighbor d-d interactions.

of monolayer MoS_2(1H) onto a tight binding model, taking d orbitals of Mo and p orbitals of S as basis states. Since previous studies have mainly focused on the interactions between relevant d orbitals to capture the dispersion around **K**, we start our analysis by looking at the importance of the direct hopping between d orbitals on neighboring Mo atoms. Within the wannierised tight binding model, we have selectively switched off hopping interactions for electrons occupying d orbitals on the Mo atoms. The resulting modified band structure is shown in Fig. 3.2 b. The material becomes metallic in the absence of direct d-d hopping. However, the gap does not close completely along the Γ-K direction implying indirect hopping of d electrons via p states of chalcogens plays important role in determining the low energy electronic structure.

3.3.3 Construction of The d Only Model

Instead of using the full Wanniersed tight binding model, we have first constructed a 3-band tight binding Hamiltonian with the basis

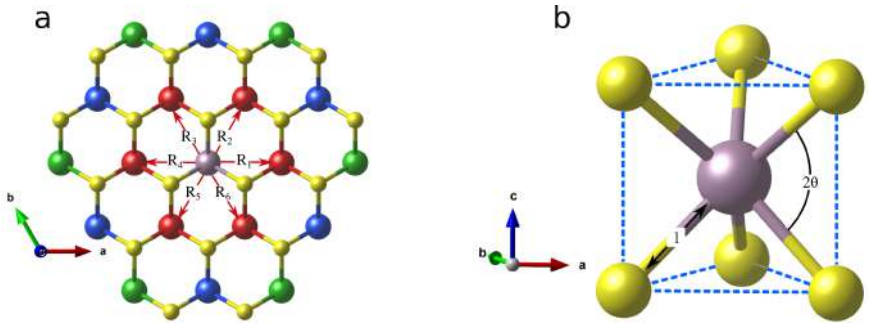

Figure 3.3: (a) Mo network in 1H MoS_2 as viewed from the c axis. The central Mo atom is in purple. The red, blue and green Mo atoms are respectively first, second and third neighbor to the central Mo atom. (b) Six neighboring S atom (yellow) to the central Mo atom are shown. The structural parameters l (Mo-S bond length) and θ (Angle between S atoms and Mo-plane) are also shown.

Atom number	Lattice vector	Direction cosine (l,m,n)
1	$\boldsymbol{R_1} = \langle a, 0, 0\rangle$	$(1, 0, 0)$
2	$\boldsymbol{R_2} = \langle \frac{a}{2}, \frac{\sqrt{3}a}{2}, 0\rangle$	$(\frac{1}{2}, \frac{\sqrt{3}}{2}, 0)$
3	$\boldsymbol{R_3} = \langle -\frac{a}{2}, \frac{\sqrt{3}a}{2}, 0\rangle$	$(-\frac{1}{2}, \frac{\sqrt{3}}{2}, 0)$
4	$\boldsymbol{R_4} = \langle -a, 0, 0\rangle$	$(-1, 0, 0)$
5	$\boldsymbol{R_5} = \langle -\frac{a}{2}, -\frac{\sqrt{3}a}{2}, 0\rangle$	$(-\frac{1}{2}, -\frac{\sqrt{3}}{2}, 0)$
6	$\boldsymbol{R_6} = \langle \frac{a}{2}, -\frac{\sqrt{3}a}{2}, 0\rangle$	$(\frac{1}{2}, -\frac{\sqrt{3}}{2}, 0)$

Table 3.1: Lattice vector corresponding to the neighboring Mo atoms shown in Fig. 3.3. a is the lattice parameter for MoS_2

$\{|1\rangle = |d_{xy}\rangle, |2\rangle = |d_{x^2-y^2}\rangle, |3\rangle = |d_{z^2}\rangle\}$. The tight binding Hamiltonian $\hat{H}$ is obtained as,

$$H_{ij}(\boldsymbol{k}) = \sum_{\boldsymbol{R}} e^{i\boldsymbol{k}\cdot\boldsymbol{R}} E_{ij}(\boldsymbol{R}) \tag{3.1}$$

Where, $E_{ij}(\boldsymbol{R}) = \langle i(\boldsymbol{r})|\hat{H}|j(\boldsymbol{r}-\boldsymbol{R})\rangle$ is the hopping energy between basis $|i\rangle$ at home unit cell and $|j\rangle$ at lattice vector $\boldsymbol{R}$. To account for the interactions between d orbitals of Mo atoms, the sum is restricted to the nearest neighbors only (red colored atoms around central vi-

olet colored atom) as shown in Fig. 3.3. The positions and direction cosines of the six nearest neighbor Mo are shown in table 3.1. Since, neighboring Mo network possess inversion symmetry implying, $E_{ij}(-\boldsymbol{R}) = E_{ij}(\boldsymbol{R})$ all the Hamiltonian matrix elements within d-only model in equation (3.1) are real for all $\boldsymbol{k}$. The 3×3 Hamiltonian matrix has six independent matrix elements. The functional form of the matrix elements can be written in terms of two-centre bond integrals following the formulation of Slater and Koster (see appendixA). The model Hamiltonian have five independent parameters in the model Hamiltonian (A.4) which are $V_{dd\sigma}, V_{dd\pi}, V_{dd\delta}, \epsilon_1$ and ϵ_2. The first three of these are Slater Koaster parameters representing different types of interaction between d orbitals on the adjacent Mo atoms while the last two are the onsite energy of in plane, d_{xy} and $d_{x^2-y^2}$ and out of plane, d_{z^2} orbitals respectively.

3.3.4 Failure of The d Only Model

In a previous study[3], reasonable fit of low energy bands has been obtained with a three band model comprising only $d_{xy}, d_{x^2-y^2}$and d_{z^2} as basis states by considering $d-d$ interactions up to third Mo neighbour of the central Mo atom. The fitted parameters obtained in that study have been analysed to understand the physical relevance of those parameters. The first, second and third neighbor Slater-Koster parameters have been estimated using the best fitted parameters obtained from [3]. These are shown in table 3.2. The parameters are not physically meaningful, in the sense that the Slater Koster parameters does not decrease consistently with more distant neighbor. This suggests, trying to fit the low energy bands in this material with d-only model considering higher neighbor interactions and thereby increasing number of independent model parameters yield a reasonable fit of the bands at the cost of losing the physical relevance of those parameters.

The failure of any model, constructed with only d orbitals, can be understand by looking at the matrix element between $d_{x^2-y^2}$ and d_{xy}, given by $\left(\frac{3\sqrt{3}}{4}V_{dd\sigma} - \sqrt{3}V_{dd\pi} + \frac{\sqrt{3}}{4}V_{dd\delta}\right)\sin\alpha\sin\beta$ (AppendixA), where $\alpha = ak_x$ and $\beta = a\sqrt{3}k_y$. The momentum dependent phase $\sin\alpha\sin\beta$ is zero at both $\Gamma = (0,0,0)$ and $K = (\frac{2\pi}{3a}, \frac{2\pi}{\sqrt{3}a})$. Physically this means that no hopping between in plane d orbitals is allowed at the K point in the absence of the S-p states. Consequently, within this model, the in plane orbitals ($d_{x^2-y^2}$ and d_{xy}) remain degenerate at both these point. Therefore, a crossing between d bands is unavoidable to allow for the orbital character reversal of VBM and CBM between Γ and K. A crucial observation is the fact that this limitation of the d only model can not be removed by adding second, third or higher Mo-Mo neighbors as the direct hopping term between $d_{x^2-y^2}$ and d_{xy} remains zero as the phase associated with direct hopping of d electrons between adjacent Mo atoms is zero for all higher neighbor Mo-Mo interactions.

3.3.5 Inclusion of S-p Orbitals in TB Hamiltonian

Having shown that the insulating gap across the Brillouin zone can not be described within a d-only model, we have next constructed a 7 band model with the addition of Sulfur p_x and p_y into the the basis. This allows for sulfur p mediated hopping between two different d states on neighboring Mo atoms. The neighboring S atoms to the central Mo atom are shown in fig. 3.3. Using the same definition

SK parameter	1^{st} neighbor	2^{nd} neighbor	3^{rd} neighbor
$V_{dd\sigma}$	1.680 ± 0.16	-0.159 ± 0.03	-0.290 ± 0.01
$V_{dd\pi}$	0.085 ± 0.16	-0.040 ± 0.03	0.266 ± 0.01
$V_{dd\delta}$	-1.310 ± 0.16	0.190 ± 0.03	0.147 ± 0.01

Table 3.2: Estimated values of Slater-Koster parameters between different neighboring Mo atoms using the effective hopping interactions terms obtained from [3]

as the d only model, the additional matrix elements have been constructed (see Appendix A). The extra independent parameters are, ϵ_3,$V_{dp\sigma}$,$V_{dp\pi}$,$V_{pp\sigma}$,$V_{pp\pi}$.

The 7 band TB model is fitted with the *ab initio* band structure to obtain the low energy d bands accurately. By comparing the *ab initio* band structure superposed onto TB bands in fig. 3.4, we can see that the minimal 7-band model with only first neighbor interaction between Mo-S, Mo-Mo and S-S, provide reasonably fitted low energy bands. The best fitted parameters are listed in table 3.3.

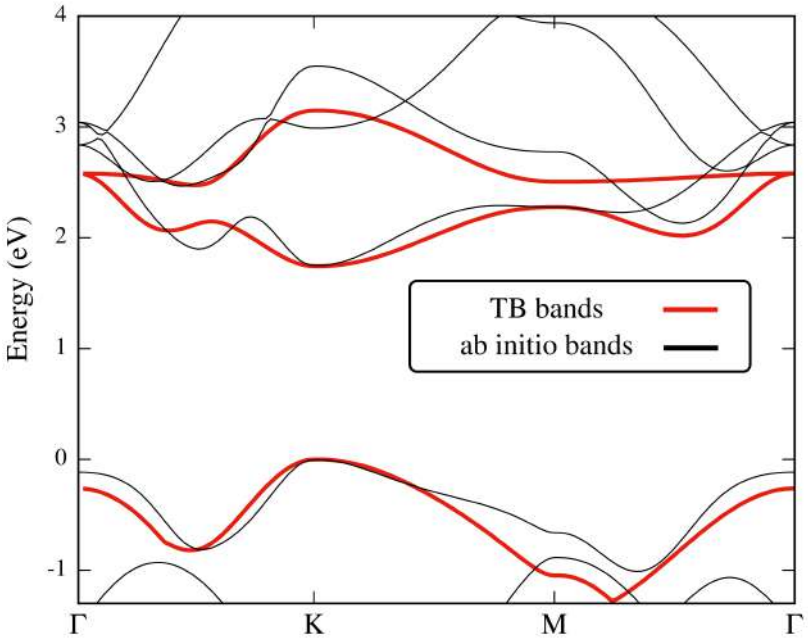

Figure 3.4: Comparison of fitted bands (red lines) from TB-Hamiltonian with *ab initio* bands (black lines).

3.3.6 Role of In-plane S-p States

To analyse the role of the p_x and p_y states of S to bring about insulating gap everywhere along with the reversal of the orbital character

ϵ_1	ϵ_2	ϵ_3	$V_{dd\sigma}$	$V_{dd\pi}$	$V_{dd\delta}$	$V_{dp\sigma}$	$V_{dp\pi}$	$V_{pp\sigma}$	$V_{pp\pi}$
-0.84	-4.44	-4.72	-0.04	0.22	-0.19	0.01	-0.58	0.86	-0.03

Table 3.3: Fitted parameters of the seven band model based on the *ab initio* band structure of 1H MoS_2. The parameters are in units of eV.

between VBM and CBM at Γ and K, the tight binding Hamiltonian at Γ and K point has been looked at. Dividing the basis into two subset: A, comprising of Mo-d states and B, comprising S-p states, we have downfolded $\mathcal{H}_B$ onto $\mathcal{H}_A$ to obtain an effective 3×3 band model as follows.

$$\mathcal{H}_{eff} = \mathcal{H}_A + \mathcal{V}(\mathbb{I} - \epsilon\mathcal{H}_B)\mathcal{V}^\dagger \tag{3.2}$$

where, $\mathcal{V}$ is the off diagonal block and ϵ is an eigenvalue within the energy window of interest. The effective Hamiltonian of d bands incorporates both the direct hopping interactions between d orbitals of adjacent Mo atoms and the indirect hopping interactions via Sulfur p states. The Hamiltonian block of d orbitals before and after downfolding explains the important role played by the p orbitals in this system. At Γ point the effect of downfolding is shown below,

$$\begin{pmatrix} -0.4 & 0.00 & 0.00 \\ 0.00 & -0.4 & 0.00 \\ 0.00 & 0.00 & -5.51 \end{pmatrix} \xrightarrow[p \text{ block onto } d \text{ block}]{\text{Downfolding}} \begin{pmatrix} -0.21 & 0.00 & 0.00 \\ 0.00 & -0.21 & 0.00 \\ 0.00 & 0.00 & -5.51 \end{pmatrix}$$

Similarly, at the K point the effect of downfolding is shown below.

$$\begin{pmatrix} -1.05 & 0.00 & 0.00 \\ 0.00 & -1.05 & 0.00 \\ 0.00 & 0.00 & -3.9 \end{pmatrix} \xrightarrow[p \text{ block onto } d \text{ block}]{\text{Downfolding}} \begin{pmatrix} -0.4 & -0.69i & 0.00 \\ 0.69i & -0.4 & 0.00 \\ 0.00 & 0.00 & -0.5 \end{pmatrix}$$

All the matrices above are written with the ordering of the basis as $\{|d_{xy}\rangle, |d_{x^2-y^2}\rangle, |d_{z^2}\rangle\}$. As shown earlier, direct hopping between different d orbitals on neighboring Mo atoms are prohibited at both

Γ and K point. Consequently, at both these point the dd block have the off-diagonal terms all zero. The effective Hamiltonian at Γ shows that both hopping pathways, direct and via p states, the interactions between in-plane d orbitals remains zero making the d_{xy} and $d_{x^2-y^2}$ orbitals degenerate. While at K, the hopping between different in plane d orbitals on adjacent Mo atoms is allowed via S-p states and therefore the interaction between these orbitals is finite after downfolding.

3.4 Conclusion

We have studied the insulating phase in the 1H MoS_2 in detail using *ab initio* calculations and constructing tight binding models. It is shown that although the gap is primarily between d states of the transition metals, indirect hopping via S-p states plays a crucial role in determining the insulating character of these materials. In particular, we have showed that a model Hamiltonian constructed only with d bands fails to describe the insulating gap across the Brillouin zone. Including the p orbitals within the model, allows for the indirect hopping between d orbitals on adjacent transition metal atoms via the chalcogen p states at the K point. Therefore, the in plane orbitals, d_{xy} and $d_{x^2-y^2}$ can interact via the chalcogen p states at K while they remain degenerate at Γ. Consequently, the ordering of the transition metal d states reverses between Γ and K while the system remain insulating throughout.

Bibliography

[1] E.M. Vogel and J.A. Robinson. Two dimensional layered transition-metal dichalcogenides for versatile properties and applications. *MRS Bulletin*, 40:558–563, 2015.

[2] Q. Wang, K. Kalantar-Zadeh, A. Kis, et al. Electronics and optoelectronics of two-dimensional transition metal dichalcogenides. *Nature Nanotech*, 7:699–712, 2012.

[3] Gui-Bin Liu, Wen-Yu Shan, Yugui Yao, Wang Yao, and Di Xiao. Three-band tight-binding model for monolayers of group-vib transition metal dichalcogenides. *Phys. Rev. B*, 88:085433, Aug 2013.

[4] P. E. Blöchl. Projector augmented-wave method. *Phys. Rev. B*, 50:17953–17979, Dec 1994.

[5] G. Kresse and D. Joubert. From ultrasoft pseudopotentials to the projector augmented-wave method. *Phys. Rev. B*, 59:1758–1775, Jan 1999.

[6] W. Kohn. Nobel lecture: Electronic structure of matter—wave functions and density functionals. *Rev. Mod. Phys.*, 71:1253–1266, Oct 1999.

[7] G. Kresse and J. Hafner. Ab initio molecular dynamics for liquid metals. *Phys. Rev. B*, 47:558–561, Jan 1993.

[8] G. Kresse and J. Furthmüller. Efficient iterative schemes for ab initio total-energy calculations using a plane-wave basis set. *Phys. Rev. B*, 54:11169–11186, Oct 1996.

[9] G. Kresse and J. Furthmüller. Efficiency of ab-initio total energy calculations for metals and semiconductors using a plane-wave basis set. *Computational Materials Science*, 6(1):15–50, 1996.

[10] K. D. Bronsema, J. L. De Boer, and F. Jellinek. On the structure of molybdenum diselenide and disulfide. *Zeitschrift für anorganische und allgemeine Chemie*, 540(9-10):15–17, 1986.

[11] Nicola Marzari and David Vanderbilt. Maximally localized generalized wannier functions for composite energy bands. *Phys. Rev. B*, 56:12847–12865, Nov 1997.

[12] Nicola Marzari, Arash A. Mostofi, Jonathan R. Yates, Ivo Souza, and David Vanderbilt. Maximally localized wannier functions: Theory and applications. *Rev. Mod. Phys.*, 84:1419–1475, Oct 2012.

[13] Arash A. Mostofi, Jonathan R. Yates, Giovanni Pizzi, Young-Su Lee, Ivo Souza, David Vanderbilt, and Nicola Marzari. An updated version of wannier90: A tool for obtaining maximally-localised wannier functions. *Computer Physics Communications*, 185(8):2309–2310, 2014.

CHAPTER 4

The QSH phase in 1T′ TMDCs

"What we know is a drop, what we don't know is an ocean"

Sir Isaac Newton

4.1 Introduction

The study of quantum spin hall (QSH) insulating phases[1, 2, 3, 4, 5] of matter has been central to the development of quantum electronic devices at the nanoscale. This new phase has conducting edge modes which are protected against back scattering by time reversal symmetry, while the bulk of the material is insulating. The study of 2D quantum spin hall phase started with a landmark paper by Kane and Mele where they have shown that in the presence of time reversal symmetry, a QSH insulator can be distinguished from trivial insulators by a topological invariant Z_2 [2]. Further, they have shown that graphene in principle is a suitable candidate for QSH [1]. However, due to weak spin orbit interaction strength in graphene, the gap is much smaller than what can be experimentally detected, making it a semi-metal for all practical purposes.

The Kane Mele model describes a graphene like system with two sub-lattices having a different onsite energies. The competition between the onsite energy difference between the sub-lattice atoms (Δ) and the spin orbit interaction (λ_{SO}) strength, dictate whether the material is topologically nontrivial or not. In the regime, where the onsite energy difference dominates, the material is a trivial band insulator however, for materials with high spin orbit interactions compared to the onsite energy difference, the QSH phase sets in. Consequently, for different compounds with elements from the same group of the periodic table, the ones with heavier elements show the QSH phase. For example, HgTe[6] and HgSe[7] are both QSH insulator but HgS is a trivial insulator[8]. Similarly, Bi_2Se_3 and Bi_2Te_3 [9] both have inverted band gap while Bi_2S_3 is a trivial insulator. Qian et. al [10] has shown using a similar model involving d and p bands, that all the monolayers of Mo and W based transition metal dichalcogenides (TMDC) are quantum spin hall insulators in their 1T' phase. All six materials have an inverted gap, in the vicinity of Γ, arising due to the chalcogen p states having higher energy than the transition metal d states and also a Dirac cone, existing in this region of the Brillouin zone. Spin orbit interactions gap the Dirac cone and a small fundamental gap opens up making the materials QSH insulators. However, unlike the II-VI semiconductors, where the gap is mainly between the anion p and cation s states, making the level inversion plausible, in the case of monolayer transition metal dichalcogenides in the semiconducting 1H phase, the gap is believed to arise from crystal field effects and is between different d orbitals. Therefore the idea of level inversion in these material is questionable and so we investigate the origin using a combination of *ab initio* calculations mapped onto realistic models.

These monolayer TMDCs have various polymorphs. The most stable polymorph, 1H, have a large direct bandgap, whereas the 1T phase is a metal with a Fermi surface comprising of many hole and electron pockets across the Brillouin zone. Distortions in the 1T polymorph, brings about the QSH insulating phase in 1T' polymorph. Since the neighboring atomic bond-lengths are very similar in 1H and 1T, the different electronic properties in these polymorphs is due to the different crystal field effect as well as availability of different hopping pathways depending on the local chalcogen environment in different polymorphs. For example, in 1H polymorph owing to trigonal biprismatic arrangement of chalcogens, the d levels of transition metals split into 3 groups. d_{z^2} has the lowest energy whereas d_{xy} and $d_{x^2-y^2}$ are next higher energy states and the highest energy states are d_{xz} and d_{yz}. Due to a d electron count of 2 in the transition metals in these materials, 1H polymorph is insulating. Similarly, for 1T polymorph, the octahedral arrangement of chalcogens splits the d levels into lower energy t_{2g} (d_{xy}, d_{xz} and d_{yz}) states and higher energy e_g ($d_{x^2-y^2}$ and d_{z^2}) states making the material metallic. However, these crystal field arguments are clearly not complete as the gap and low energy bands are not dictated by d levels only, rather the p orbitals of chalcogen plays a crucial role. Therefore, it is important to understand the role of different structures in order to understand the electronic properties of different polymorphs.

In this project, we have studied different polymorphs in detail to understand the origin of such unusual band inversion in all the materials of this class and the role of crystal structure in driving the QSH insulating phase in 1T' polymorph. We show that although these materials have a positive Δ in different polymorphic structure, the strong second neighbor interactions renormalizes the orbital energy by introducing a k dependent term. Consequently, Δ becomes effec-

tively negative at the Γ point. We further show that the hybridization between transition metal d and chalcogen p states strongly depend on the crystal structure. We find the distortions in 1T' phase give rise to linear chalcogen chains reducing the $d-p$ hybridization and therefore the conduction and valence band at Γ becomes pure p and d bands respectively. As a result, a crossing between these bands in the vicinity of zone centre becomes unavoidable making all the material in this polymorph a QSH insulator.

4.2 Computational Methods

4.2.1 *ab initio* Calculations

The *ab-initio* calculation have been performed using projector augmented wave [11, 12] method implementation of density functional theory (DFT) [13] within VASP[14, 15, 16]. The monolayer is constructed from the bulk structures by adding a vacuum of 20 Å in the c direction. This nullifies the interactions between images of periodic supercells. In each calculation, atomic positions have been relaxed to reduce the forces acting on the atom to lie below the tolerance value of 1 meV/Å. Perdew-Burke-Ernzerhof potentials [17] were used for the exchange correlation functional. For the self-consistent calculation for monolayer TMDCs, a k-space grid of $8\times8\times1$ was used. The cutoff energy for the plane wave basis was taken to be 800 eV.

4.2.2 Tight Binding Fitting

The tight binding Hamiltonian is constructed with maximally localized Wannier functions (MLWF) [18, 19], obtained through WANNIER90 code[20]. The basis of the model Hamiltonian consists of the p orbitals of chalcogens and d orbitals of the transition metal. The spread of the MLWF in all the calculations have not exceeded 2.0 Å^2

implying that the MLWFs are good descriptor of the atomic orbitals.

4.3 Results and Discussion

4.3.1 Crystal and Electronic Structure of Different Polymorphs

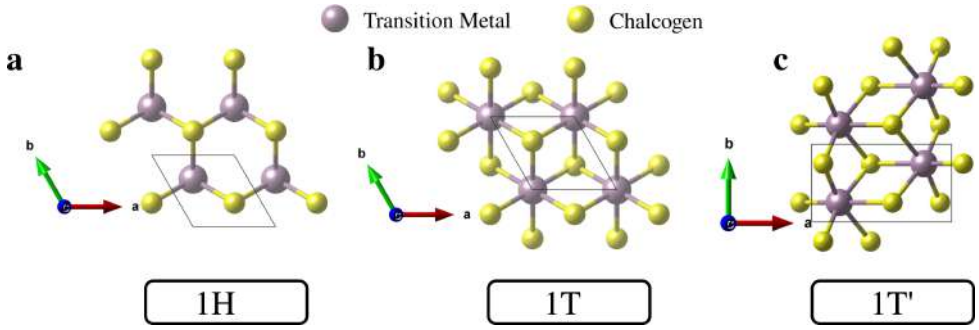

Figure 4.1: Arrangement of transition metal and chalcogens in different polymorphs as viewed from c-axis. (a)Trigonal bi prismatic arrangement in 1H polymorph , (b) Octahedral arrangement in 1T polymorph and (c) Distorted octahedra in 1T'

Different polymorphs of TMDCs are shown in Fig. 4.1. In each case, the transition metals are sandwiched between two layers of chalcogens. The most stable polymorph is the hexagonal(1H) structure, where the chalcogens are in a trigonal biprismatic arrangement around the transition metal. As shown in Fig. 4.1**a**, the chalcogens in top and bottom layers sit on top of each other. In the 1T polymorph, shown in Fig. 4.1**b**, the chalcogens form an octahedra around the transition metal atom. The TMDCs are unstable in this structure and lower their energy by distorting into the 1T' structure shown in Fig. 4.1**c**. The distortion in going from 1T to 1T' involves the transition metals forming dimers.

We have next examined the crystal field effects in the different polymorphs in order to understand the electronic structure. In the

most stable 1H phase, the crystal field splitting due to the trigonal biprismatic arrangement of the chalcogens is believed to give rise to a bandgap between the occupied d_{z^2} orbitals and the unoccupied $d_{x^2-y^2}$ and d_{xy} orbitals, although the origin of the insulating gap is more complicated and have been discussed in chapter 3. However, due to octahedral crystal field of chalcogens in the 1T phase, makes the lower energy t_{2g} orbitals partially filled and thereby 1T phase becomes metallic.

The bond lengths between the transition metal and chalcogen are very similar in 1H and 1T structure. Hence, one would not expect very different electronic behaviour in these structures. However, one finds that while 1H structure is a semiconducting (Fig. 4.2)**a** with a direct band gap of 1.76 eV at K point of the Brillouin zone, the 1T structure is metallic (Fig. 4.2)**b**. This suggests that the crystal field effect and the filling of the orbitals dictates the electronic ground state of these polymorphs. The low energy bands in 1T (Fig. 4.2)**b**) have very small dispersional width. Therefore the Mo atoms come closer to form dimers enhancing the interactions between d orbitals. Consequently a gap opens up almost everywhere in the Brillouin zone except a small region around Γ as shown in Fig.4.2**c** where one finds a Dirac cone shown by dashed circle.

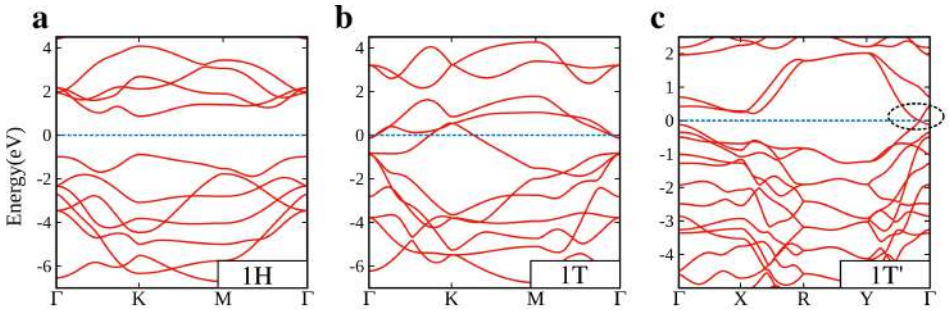

Figure 4.2: Electronic band structure along different high symmetry directions in (a) 1H, (b) 1T and (c)1T' polymorph

4.3.2 Renormalization of Onsite Energies

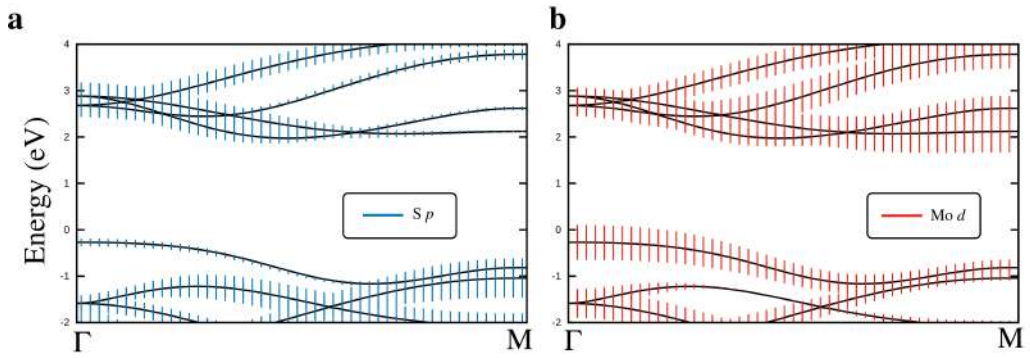

Figure 4.3: Orbital projected band dispersion near Γ point in 1H MoS_2

In order to understand the different electronic structure in these polymorphs we have mapped the *ab initio* band structures, onto a tight binding model with Mo-d and S-p states as basis. The onsite energies of the tight binding model for 1H are given in table 4.1. The d states have higher onsite energy than the p states with the splitting of the d orbitals following the expected crystal field ordering for 1H polymorph. However, plotting the orbital character of the *ab initio* bands one finds a different picture. The contributions from d orbitals of Mo and p orbitals of S are shown in Fig. 4.3 where black solid lines are dispersive bands near Γ point and vertical lines have proportional height to the contribution of a particular orbital at that k point. The blue and red lines in Fig. 4.3**a** and 4.3**b**, indicate the contribution from S-p states and Mo-d states respectively. The valence band top at Γ is mainly contributed by the d states but the conduction band at Γ have contributions from both Mo-d and S-p states implying strong $d-p$ hybridization.

Orbital	d_{z^2}	d_{xz}	d_{yz}	$d_{x^2-y^2}$	d_{xy}	p_x	p_y	p_z
Onsite Energy	-3.10	-1.88	-1.88	-2.88	-2.88	-4.53	-4.53	-4.83

Table 4.1: Extracted onsite energies for different orbitals from the tight binding fitting.

We then examine the tight binding Hamiltonian within the Mo d block ($\mathcal{H}_{dd}$) and S p block ($\mathcal{H}_{pp}$) at Γ . The matrix blocks are given below.

$$\mathcal{H}_{dd} = \begin{pmatrix} -4.8 & 0 & 0 & 0 & 0 \\ 0 & -2.38 & 0 & 0 & 0 \\ 0 & 0 & -2.38 & 0 & 0 \\ 0 & 0 & 0 & -3.55 & 0 \\ 0 & 0 & 0 & 0 & -3.53 \end{pmatrix} \tag{4.1}$$

with the basis in the order $\{d_{z^2}, d_{xz}, d_{yz}, d_{x^2-y^2}, d_{xy}\}$ and,

$$\mathcal{H}_{pp} = \begin{pmatrix} -1.99 & 0 & 0 \\ 0 & -1.99 & 0 \\ 0 & 0 & -4.80 \end{pmatrix} \tag{4.2}$$

with the basis in the order $\{p_x, d_y, p_z\}$. We find that the S-p states are energetically higher than the Mo-d states at Γ. Since, the unit cell considered in the tight binding Hamiltonian, have a single Mo atom and two S atoms belonging to the top an bottom chalcogen layer, interactions between Mo-Mo or between S-S changes the diagonal onsite blocks of the tight binding Hamiltonian. Consequently, Δ acquires an additional k dependent term. This k dependent part makes Δ effectively negative at Γ as shown schematically in Fig. 4.4. In the left, the positions of the different orbitals based on their fitted onsite energies are shown. Due to renormalization process p_x and p_y states move higher in energy making Δ negative at Γ as shown in the right side. Although there is the level reversal at Γ , the conduction band bottom at Γ is energetically much higher than the CBM making

these states inaccessible through doping. Thereby, this polymorph is not appropriate for the QSH phase.

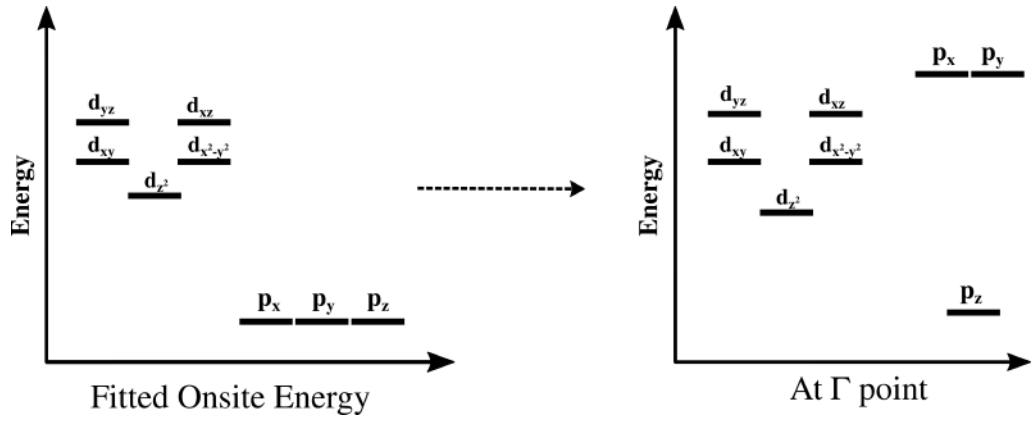

Figure 4.4: Reordering of the orbitals due to second neighbor interactions. Relative positions based on the onsite energies of different orbitals are shown in left. and the relative position of the orbitals at Γ due to renormalization is shown in the right.

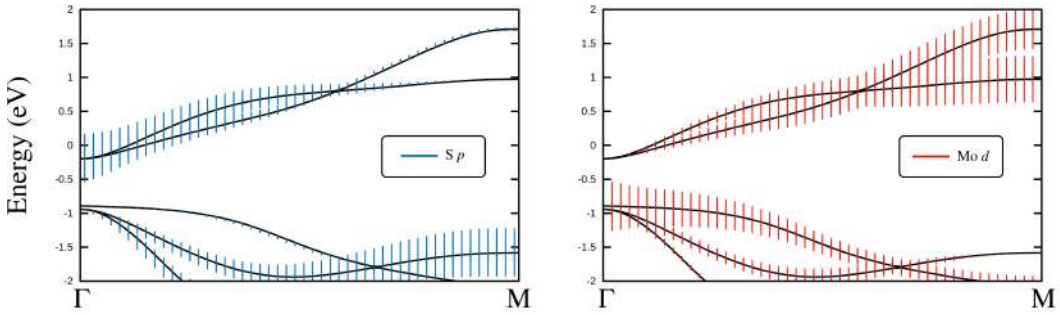

Figure 4.5: Orbital projected band dispersion of 1T MoS_2

Moving onto the 1T phase, the orbital character of low energy bands near Γ are shown in Fig. 4.5 where contributions from the S-p states Mo-d states are shown in blue and red color respectively. The p states have higher energy implying a negative Δ in this polymorph as

well. However unlike 1H, the conduction band has only contribution from p states of sulfur and the valence band has contributions from only d states of Mo. This hints at negligible hybridization between Mo and S in the vicinity of the Γ point. However, due to several other band crossing the Fermi energy , this polymorph is metallic and does not show QSH phase.

4.3.3 Origin of The Instability in The 1T Polymorph

In order to understand what determines the structural instability in the 1T phase, we have examined the electronic structure near the Fermi energy. In Fig. 4.6 contributions from $d_{x^2-y^2}$, d_{xy} and d_{z^2} orbitals have been shown. Near the zone centre, Γ, the lowest unoccupied band is mainly contributed by the in plane $d_{x^2-y^2}$ orbital. This has very small dispersional width which is very unusual as one expects significant interactions from the in plane d orbitals. In contrast d_{xy} has larger dispersional width. Examining the dispersions of the d_{z^2} bands, one finds that it is flat till halfway along the $\Gamma - K$ direction. As there are two pathways possible between the Mo atoms, one involving the direct interaction between d orbitals on both atoms, and the other is via the S-p states, we examined the contributions from these by selectively switching off different pathways and looking at the effect of different pathways in the band structure.

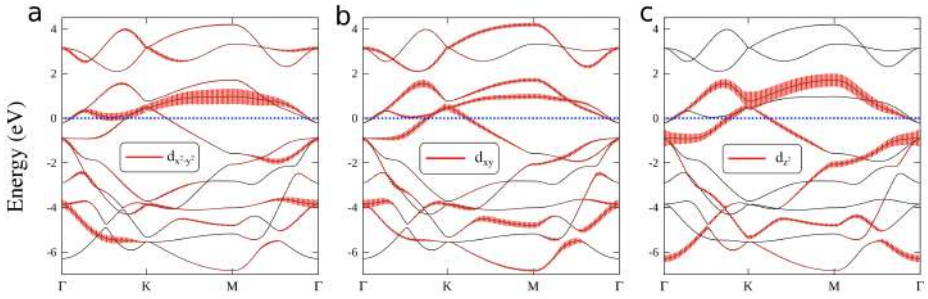

Figure 4.6: Orbital projected band structure of different d states of 1T MoS_2

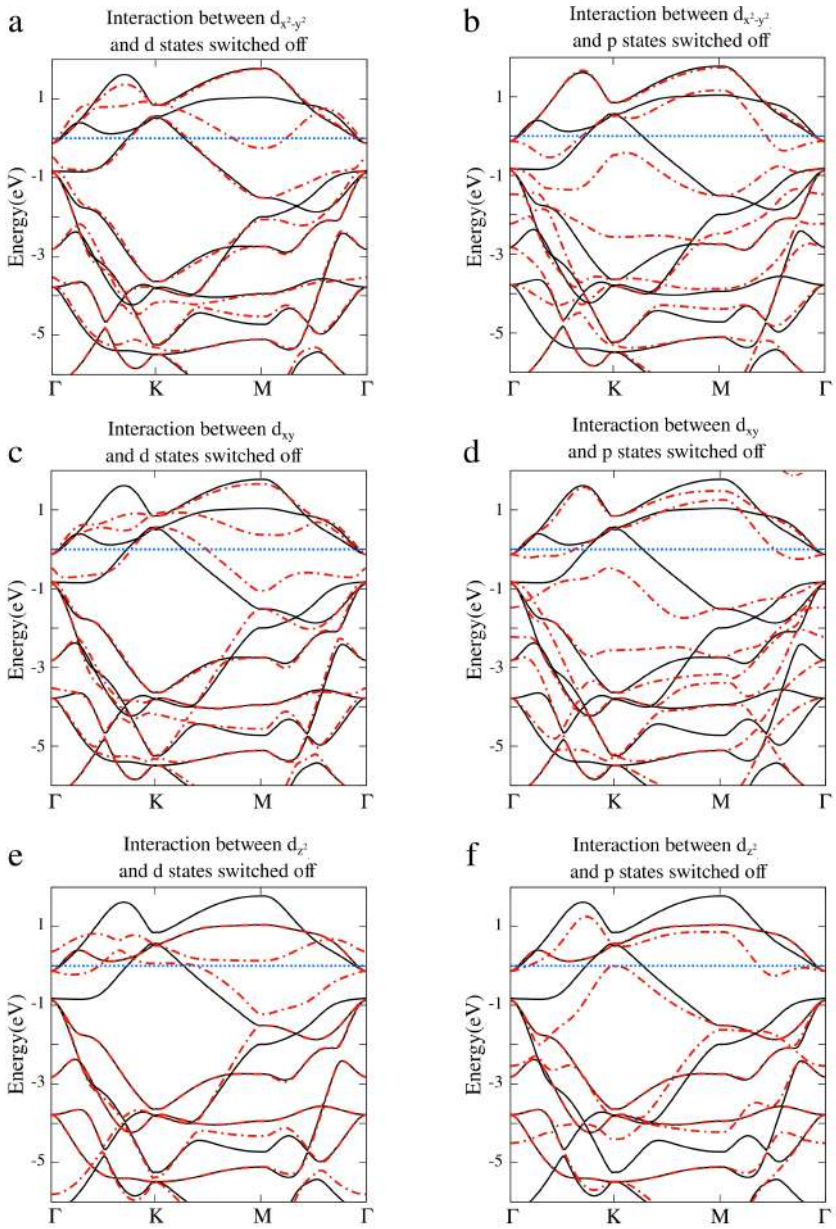

Figure 4.7: Effects of switching of interaction between a particular d orbitals with other d or p orbitals in 1T MoS_2. In each figure the black solid lines are band dispersions of original 1T MoS_2 and the red dashed lines are modified band dispersion due to switching off of the indicated interactions.

In Fig. 4.7a, the interactions between $d_{x^2-y^2}$ and other d states have been turned off. The modified band structure shown in red dashed line shows that the unoccupied $d_{x^2-y^2}$ band disperse more in upward direction near Γ although it remains flat for rest of the $\Gamma - K$ direction. On the other hand, Fig. 4.7b shows that the absence of the interactions via the S-p states make the same band disperse downward and gain more dispersional width. This explains that the original band which has a small hump (in black solid line) and then is flat has the competition between direct $d - d$ interactions and indirect hopping through S-p states as its origin. Performing the same calculation for d_{xy} one finds that, switching off the interactions with d orbitals makes the unoccupied bands more flat (Fig. 4.7c), while turning off the interactions via S-p orbitals increases the dispersional with of the unoccupied bands (Fig. 4.7d). Additionally, the highest occupied band moves deeper into the valence band in the absence of the hopping pathways via S-p states. Next in Fig. 4.7e, one can see that switching off the direct hopping pathway between d_{z^2} and d states of other Mo atoms makes the unoccupied bands nearly dispersionless in the $\Gamma - K$ direction while in Fig. 4.7f, the absence of the indirect hopping via S-p states increases the dispersional width of these bands and moves the highest occupied band deeper into valence band. Our analysis clearly suggests that the direct $d-d$ interaction is responsible for the dispersions of the Mo-d bands and the system does not gain enough dispersion from the indirect hopping via S-p states. Therefore, the Mo atoms move closer to form dimers and thereby enhance the direct hopping pathways between the d orbitals while hopping via the p states decreases. Consequently, the band width of the low energy unoccupied states increases and the highest occupied states moves deeper into the valence band driving the system into 1T' phase.

4.3.4 Origin of The QSH Phase in 1T' Polymorph

Next, we focus on the effects of the structural distortions in 1T' phase. The distance between neighboring Mo atoms changes from 1T to 1T' as shown in Fig. 4.8. In the 1T phase, the distance between all neighboring Mo atoms is 3.17 Å. However, in 1T' the Mo atoms form dimers with alternating short (2.76 Å) and long (3.81 Å) bond lengths along {110} direction as shown in Fig. 4.8**b**. This enhances the interactions between d orbitals and consequently a band gap opens up. To confirm this hypothesis, we have calculated the band dispersion within the fitted tight binding model after selectively switching of all interactions between d orbitals. In Fig. 4.9**b** the band dispersion with $d-d$ interactions switched off is shown. Comparing with the *ab initio* band structure in Fig. 4.9**a**, we found that the band gap collapses across the Brillouin zone confirming that the band gap in 1T' phase arises from the enhanced $d-d$ interactions due to dimer formation. However, we further observe that in the vicinity of the Dirac cone, the effect of $d-d$ interactions is negligible and the Dirac cone is intact.

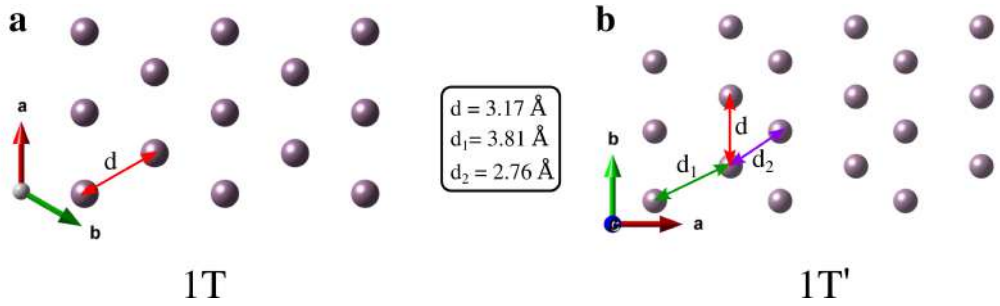

Figure 4.8: (a) Mo atoms in 1T MoS_2. Neighboring Mo atoms have same distance $d = 3.17$Å (b) Dimer formation along {110} direction due to structural distortion in 1T' MoS_2.

To understand the origin of the Dirac cone we revisit the distorted structure once more. In Fig. 4.10, different bond lengths have been

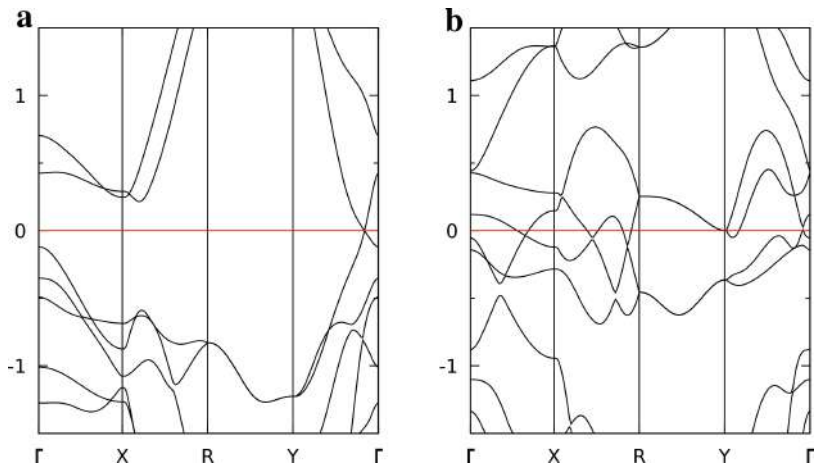

Figure 4.9: (a) *ab initio* Electronic band dispersion of 1T' MoS_2 (b) Electronic band dispersion from the tight binding Hamiltonian after switching off all interactions between d orbitals

marked. Apart form the Mo atoms forming a dimer, we find that quasi 1D linear chains have formed along {010} direction by the S atoms. The cyan and yellow sulfur chains are respectively above and below the central Mo atoms. Due to isolated chain formation, indirect hopping between d orbitals through p states of Sulfur has decreased and the direct interactions between p orbitals of sulfurs belonging to the linear chain increases. Calculating the charge density of the conduction band at Γ, one finds that the p_y orbitals of sulfur atoms belonging to the isolated chain contribute to it. This is shown in Fig. 4.11.

To probe the effect of the isolated chains, we have systematically decreased the interactions between p orbitals and calculated the band dispersions and Z_2 index within the fitted tight binding model. The result is shown in Fig. 4.12.Although reduction of $p-p$ interactions has hardly any effect on the band gap across the Brillouin zone, we find that the fundamental gap closes and reopens making the transition from the QSH state to trivial insulating state.

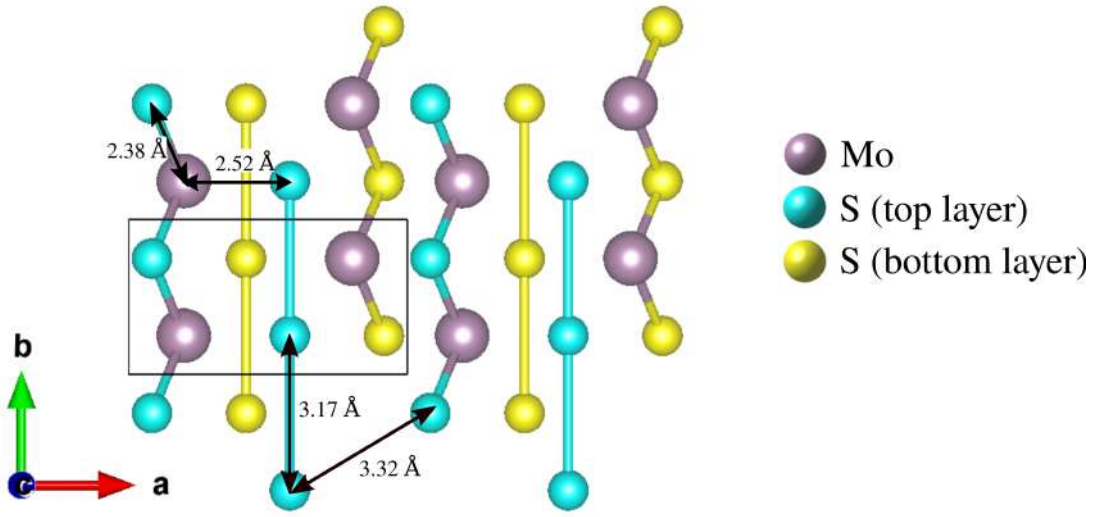

Figure 4.10: Linear isolated chains of sulfur atoms in top and bottom layer emerging due to structural distortions in 1T' MoS_2.

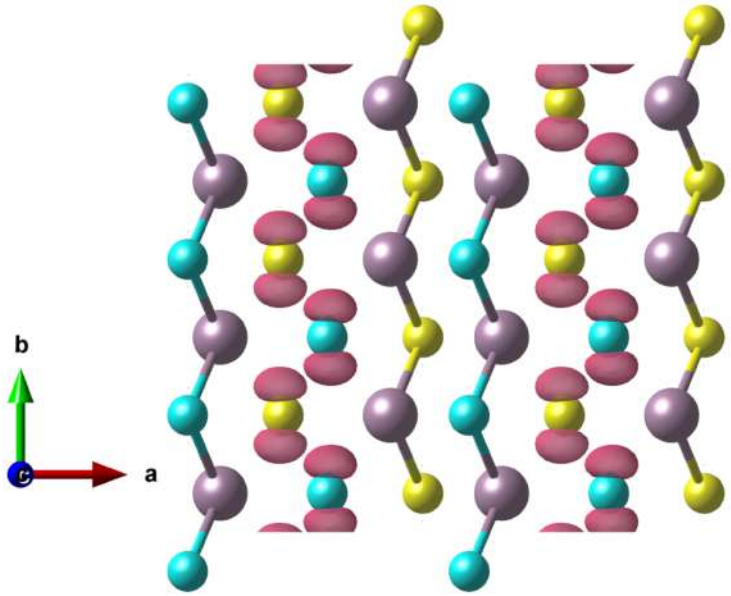

Figure 4.11: Charge density of the conduction band at Γ

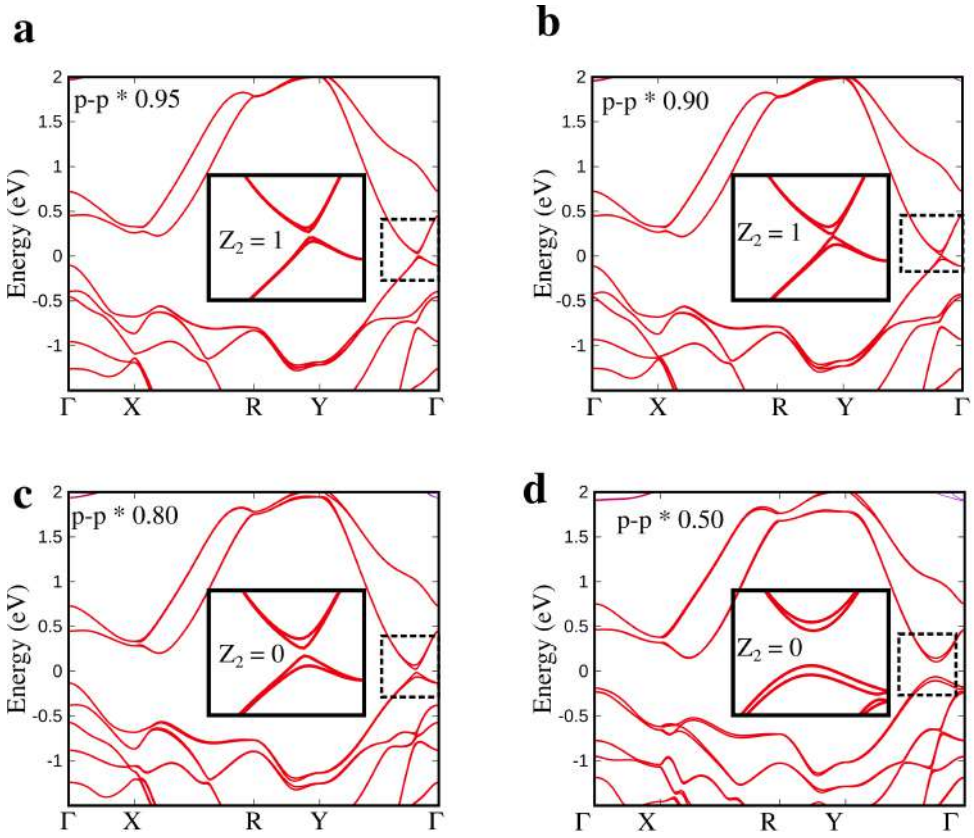

Figure 4.12: Evolution of tight binding band dispersion of 1T' MoS_2 with reduction of interactions between different p orbitals. At (a) 95% (b) 90% (c) 80% (d) 50% of original interactions strength.

4.4 Conclusion

We have studied topological insulating phase in 1T' TMDCs. By performing *ab initio* study and mapping them onto tight binding model, we have shown that electronic properties in different polymorph is strongly related to the local environment of chalcogens around the transition metals. Furthermore, our calculation has shown that the onsite energy difference between two sublattice atoms (Δ) acquires a k dependent term and is negative at Γ in all the polymorphs making an inverted gap feasible. However, in 1H phase, we have found

strong hybridization between Mo-d and S-p states opens a large gap at the zone centre making it a trivial band insulator. Due to octahedral arrangement of chalcogens in 1T phase, the hybridization at Γ reduces and the inverted gap is between pure p and d states, but due to several other bands crossing the Fermi energy in various places of the Brillouin zone makes this polymorph a metal. We have further shown that the structural instability and the distortions in the 1T phase results from the competition between direct $d-d$ hopping strength and indirect hopping through the p states. As a result, in 1T' phase, structural distortions creates Mo dimer and isolated linear sulfur chains. The enhanced direct interactions between d orbitals opens up a large gap across the Brillouin zone except the small region around Γ and the interactions between p orbitals within the linear sulfur chains dictates the Dirac cone within this region making it a QSH insulator.

Bibliography

[1] C. L. Kane and E. J. Mele. Quantum spin hall effect in graphene. *Phys. Rev. Lett.*, 95:226801, Nov 2005.

[2] C. L. Kane and E. J. Mele. Z_2 topological order and the quantum spin hall effect. *Phys. Rev. Lett.*, 95:146802, Sep 2005.

[3] B. Andrei Bernevig and Shou-Cheng Zhang. Quantum spin hall effect. *Phys. Rev. Lett.*, 96:106802, Mar 2006.

[4] M. Z. Hasan and C. L. Kane. Colloquium: Topological insulators. *Rev. Mod. Phys.*, 82:3045–3067, Nov 2010.

[5] Xiao-Liang Qi and Shou-Cheng Zhang. Topological insulators and superconductors. *Rev. Mod. Phys.*, 83:1057–1110, Oct 2011.

[6] B. Andrei Bernevig, Taylor L. Hughes, and Shou-Cheng Zhang. Quantum spin hall effect and topological phase transition in hgte quantum wells. *Science*, 314(5806):1757–1761, 2006.

[7] Li J., C. He, L. Meng, et al. Two dimensional topological insulators with tunable band gaps: Single-layer hgte and hgse. *Sci Rep*, 5:14115, 2015.

[8] Chang-Youn Moon and Su-Huai Wei. Band gap of hg chalcogenides: Symmetry-reduction-induced band-gap opening of materials with inverted band structures. *Phys. Rev. B*, 74:045205, Jul 2006.

[9] Zhang H., Liu CX, Qi XL., et al. Topological insulators in bi_2se_3, bi_2te_3 and sb_2te_3 with a single dirac cone on the surface. *Nature Phys*, 5:438–442, 2009.

[10] Xiaofeng Qian, Junwei Liu, Liang Fu, and Ju Li. Quantum spin hall effect in two-dimensional transition metal dichalcogenides. *Science*, 346(6215):1344–1347, 2014.

[11] P. E. Blöchl. Projector augmented-wave method. *Phys. Rev. B*, 50:17953–17979, Dec 1994.

[12] G. Kresse and D. Joubert. From ultrasoft pseudopotentials to the projector augmented-wave method. *Phys. Rev. B*, 59:1758–1775, Jan 1999.

[13] W. Kohn. Nobel lecture: Electronic structure of matter—wave functions and density functionals. *Rev. Mod. Phys.*, 71:1253–1266, Oct 1999.

[14] G. Kresse and J. Hafner. Ab initio molecular dynamics for liquid metals. *Phys. Rev. B*, 47:558–561, Jan 1993.

[15] G. Kresse and J. Furthmüller. Efficient iterative schemes for ab initio total-energy calculations using a plane-wave basis set. *Phys. Rev. B*, 54:11169–11186, Oct 1996.

[16] G. Kresse and J. Furthmüller. Efficiency of ab-initio total energy calculations for metals and semiconductors using a plane-wave basis set. *Computational Materials Science*, 6(1):15–50, 1996.

[17] John P. Perdew, Kieron Burke, and Matthias Ernzerhof. Generalized gradient approximation made simple. *Phys. Rev. Lett.*, 77:3865–3868, Oct 1996.

[18] Nicola Marzari, Arash A. Mostofi, Jonathan R. Yates, Ivo Souza, and David Vanderbilt. Maximally localized wannier functions: Theory and applications. *Rev. Mod. Phys.*, 84:1419–1475, Oct 2012.

[19] Nicola Marzari and David Vanderbilt. Maximally localized generalized wannier functions for composite energy bands. *Phys. Rev. B*, 56:12847–12865, Nov 1997.

[20] Arash A. Mostofi, Jonathan R. Yates, Giovanni Pizzi, Young-Su Lee, Ivo Souza, David Vanderbilt, and Nicola Marzari. An updated version of wannier90: A tool for obtaining maximally-localised wannier functions. *Computer Physics Communications*, 185(8):2309–2310, 2014.

Part III

Materials With quasi 2D Crystal Lattices

CHAPTER 5

Chiral metallic phase as CDW

"A new idea comes suddenly and in a rather intuitive way. But intuition is nothing but the outcome of earlier intellectual experience."

Albert Einstein

5.1 Introduction

$LaAgSb_2$ is found to exhibit two CDW transitions, one at 211 K which is associated with an incommensurate wave over approximately 40 unit cells along the lattice vector a and another incommensurate CDW develops along the c direction at a lower temperature of 186 K. It locks into a commensurate order involving six unit cells as the temperature is furthered lowered [1]. However, the nature and origin of these transitions are not clear and debated. A common practice is to describe electronic CDW in different materials using Fermi surface nesting, where presence of parallel sheets of the Fermi surface in a metal causes electronic instability analogous to the 1D case of Peierls transitions. Consequently, the material goes through CDW transitions and opens up a gap. But, this mechanism does not shed any light on the periodic distortions of the atoms concomitantly occurring with the electronic transitions. The Fermi surface measurements for $LaAgSb_2$ have also revealed a nesting vector, suggesting Fermi surface

nesting as the origin of the CDW [2]. There are a lot of experimental observations against a nesting driven CDW scenario. These observations are consistent with the growing understanding that while one may have regions of the Fermi surface parallel to each other, usually other effects take over and the direction of the CDW modulation has little or no connection with the nesting vector [3, 4]. NMR experiments reveal the emergence of only two distinct La species in the CDW phase which seems unusual [5] , despite the long wavelength associated with the CDW at 211 K.

We have studied the high temperature structure of $LaAgSb_2$ in detail to understand what drives the periodic lattice distortions in the system. By showing that the relative coupling in the c direction is small, we have further determined that increasing Coulomb repulsion between electron clouds of Sb and Ag layer drives the transition. Our calculation reveals that the CDW phase may have a chiral metallic structure.

5.2 Computational Method

5.2.1 *ab initio* Calculations

The *ab-initio* electronic structure was calculated using projector augmented-wave method [6, 7] implementation of density functional theory [8] within the Vienna Ab initio Simulation Package (VASP) [9, 10, 11]. The tetragonal crystal has been considered with the expermental lattice parameters given by $a = b = 4.35$ Å and $c = 10.78$ Å. The atomic positions were optimized to reduce the forces acting on the atoms to lie below the tolerance value of 10 meV/Å^2. Perdew–Burke–Ernzerhof GGA potentials [12] were used for the exchange correlation functional. For the self-consistent calculation, a

k-space grid of 8×8×4 was used for the unit cell. The cut-off energy for the plane wave basis was taken to be 600 eV.

5.2.2 Phonon calculations

The phonon frequencies and eigen modes have been calculated by determining the accurate force constants using finite displacement supercell approach implemented in the open source package Phonopy [13, 14]. First, several supercell of dimension $3 \times 3 \times 1$ have been constructed with finite displacement to one atom in each of the supercell. The forces on the atoms have been calculated by performing DFT calculations with Γ centered k mesh of $8 \times 8 \times 1$. Then, using the data set of displacement and forces acting on atoms, the dynamical matrix has been constructed. The eigen spectrum the dynamical matrix provides the phonon band structures and eigen modes.

5.3 Results and Discussions

5.3.1 Crystal Structure and Electronic Structure

$LaAgSb_2$ crystallizes in the tetragonal P4/nmm space group. As shown in Fig:5.1a, the material consists of two types of Sb atoms. One type of Sb atoms (red balls), and the Ag atoms (green balls) arrange themselves in a square net to form 2D layers. These layers are stacked alternately along the c-axis of the crystal. La ions (blue balls) and the other type of Sb (yellow balls) atoms are sandwiched within these layers. The corresponding Brillouin zone is shown in Fig:5.1b along with the corresponding high-symmetry points. The density of states (DOS) at the Fermi level as shown in Fig:5.1c is dominated by states from the 2D Sb layers with small contributions from La d-states and the p-states of the other Sb atoms.

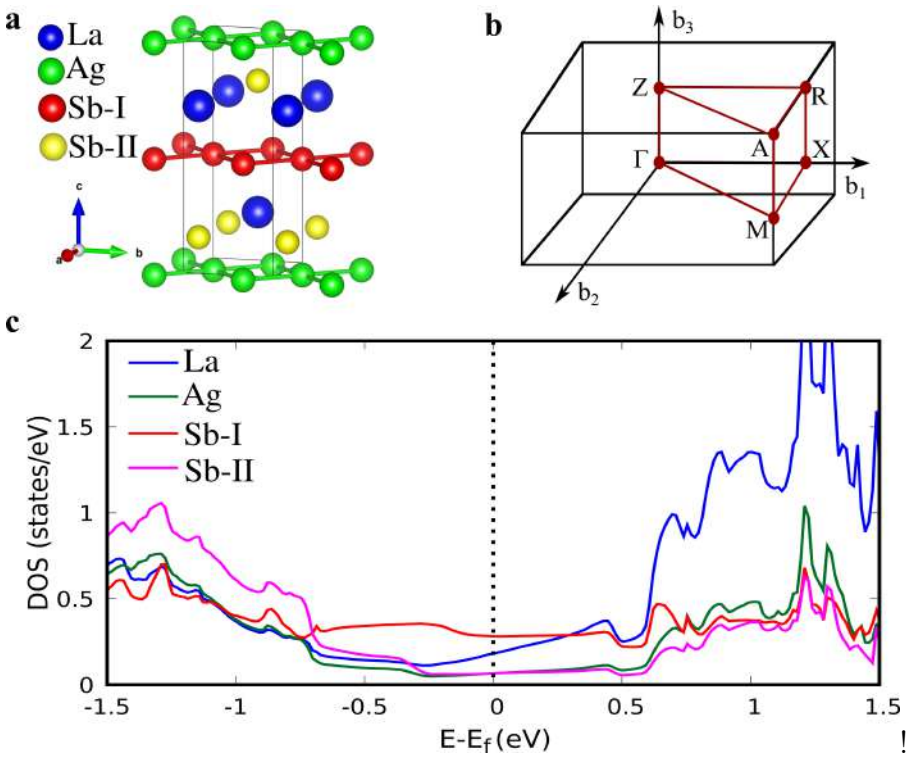

Figure 5.1: (a) High temperature ($T > T_{CDW1}$) tetragonal crystal structure of LaAgSb2 (side view). (b) Brillouin zone of $LaAgSb_2$ (c) Atom projected partial density of states

5.3.2 Multiple CDW Transitions in $LaAgSb_2$

Focusing first on the temperature dependent electrical resistivity [15], an anomaly is observed in the zero-field resistivity (ρ vs T plot in 5.2 as the sample is cooled below a characteristic temperature (T_{CDW1}=211 K). There is another anomaly present, taking place at T_{CDW2} which although difficult to spot in the ρ vs T plot, but is clearly visible in the $\partial\rho/\partial T$ vs. T plot (inset of 5.2). Both the transitions at T_{CDW1}=211 K and T_{CDW2}=183 K are associated with the partial opening of a gap due to a CDW forming along the a and c axis, respectively [1]. The CDW transition taking place at 211 K has been associated with an incommensurate order appearing, involving

approximately 40 unit cells along the lattice vector a. Consequently, one would expect the emergence of several inequivalent lattice sites. Surprisingly, however, one finds just two distinct La sites emerging from NMR measurements [5]. Additionally, these measurements suggest the presence of an underlying periodic unit. The lower temperature CDW transition at 183 K is also incommensurate. However it locks into a commensurate transition at 164 K involving six-unit cells in the c direction [1]. We focus on this transition in our study to understand and determine the periodic lattice distortions in the system from a microscopic point of view.

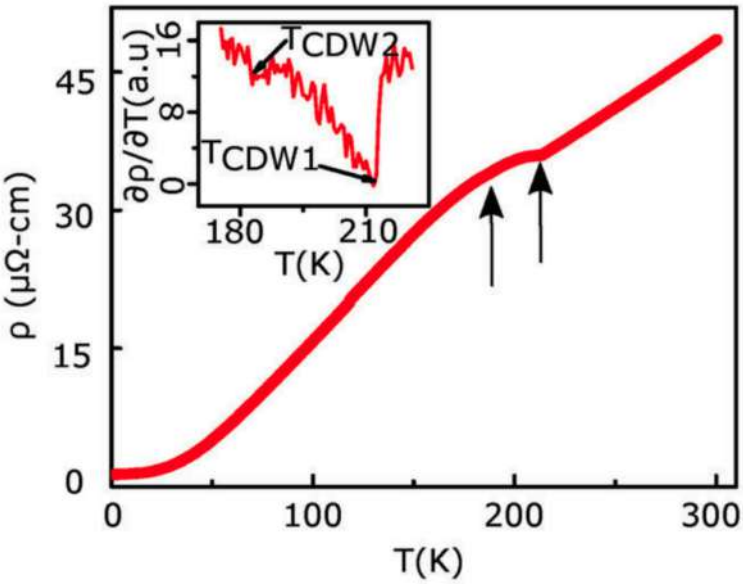

Figure 5.2: Resistivity (ρ) vs. temperature (T) plot exhibiting anomalies near the two CDW transitions indicated by the black arrows. Inset, showing the corresponding $\frac{\partial \rho}{\partial T}$ vs. T curve to depict two CDW transitions more clearly (Experiment is done by R. Alam from ANP group[15])

5.3.3 Proposed Mechanism for Periodic Distortions

First, the coupling strength in the c direction has been examined. In order to determine this, the exfoliation energy has been calculated.

A monolayer is constructed by cleaving the bulk structure in between the Sb square networks and La atoms (red and blue balls respectively in Fig: 1a) and adding a vacuum of 20 Å. The atomic positions in the constructed monolayer were then geometrically optimized and total energy was calculated. In a similar manner a bilayer has been constructed. The exfoliation energy is then given by,

$$E_{exfoliation} = \frac{E_{Bilayer} - 2 \times E_{monolayer}}{A_{surface}} \tag{5.1}$$

Where, $A_{surface} = ab$ is the area of the cleaved surface. The exfoliation energy is calculated to be 115 meV/Å^2 which places the $LaAgSb_2$ in the regime of potentially exfoliable materials [16]. Therefore the coupling strength in the c direction is weak.

Due to the weak coupling in the c direction we have calculated the phonon eigen modes for the bilayer. Previously it had been shown that layered materials like graphene, h-BN etc have low frequency shear and compression mode [17]. In our calculations, for the constructed bilayer of $LaAgSb_2$ we have found the shear mode with frequency 18.94 cm^{-1} and compression mode with frequency 31.92 cm^{-1}. These modes, shown in Fig:5.3, allows for layer sliding as well as compression of the structure.

Returning to the crystal structure in Fig:5.1a, one finds that the square networks formed by Sb and Ag atoms are stacked in an atom on atom arrangement. Furthermore, as temperature is lowered, the c lattice parameter decreases. Consequently, the electron cloud on Sb layers experience a stronger Coulomb repulsion from the electron cloud on the Ag layer. Consequently, on allowing for atomic displacements to minimize the total energy the neighboring layers slide and form a periodically distorted structure.

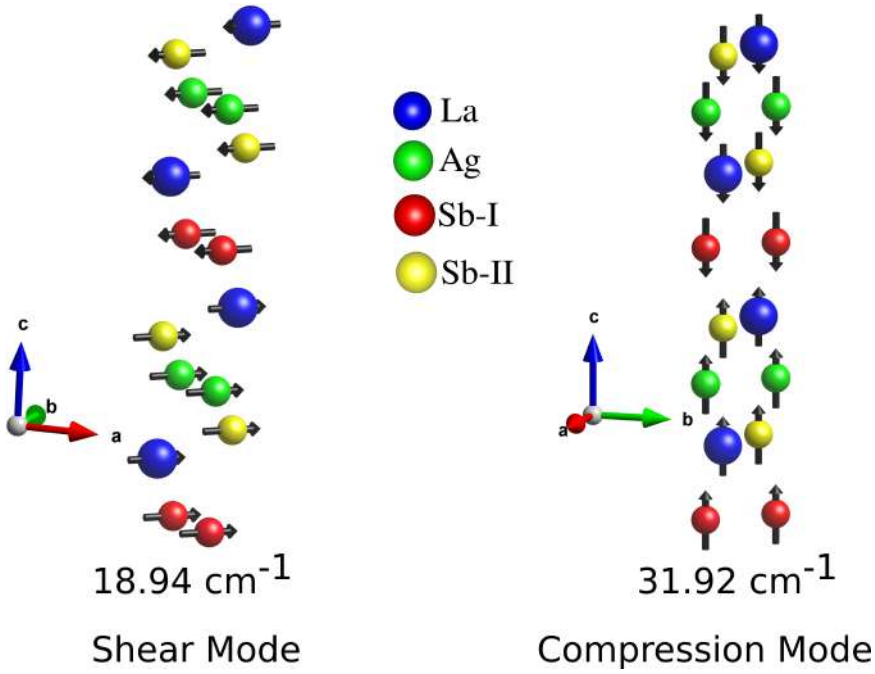

Figure 5.3: The low frequency phonon modes for constructed $LaAgSb_2$ bilayer shows (a) shear mode, (b) compression mode.

In order to test the hypothesis, a supercell of $1 \times 1 \times 6$ dimension had been constructed with accordance with the size of experimentally determined commensurate CDW modulation. Next the Sb square networks were displaced periodically along the {110} direction with respect to the Ag layers. This is shown in Fig:5.4a by pink arrows on the Sb atoms. Allowing for the atomic displacements to relax in order to minimize the total energy of the material, one finds a modulated structure with energy lowered by about 11 meV per formula unit. The periodic modulation viewed from the c axis is shown in Fig:5.4b.

5.3.4 Effect of CDW Modulation on Band Structure

To investigate properties of the obtained CDW modulation, electronic band structure is calculated. The band dispersions, calculated

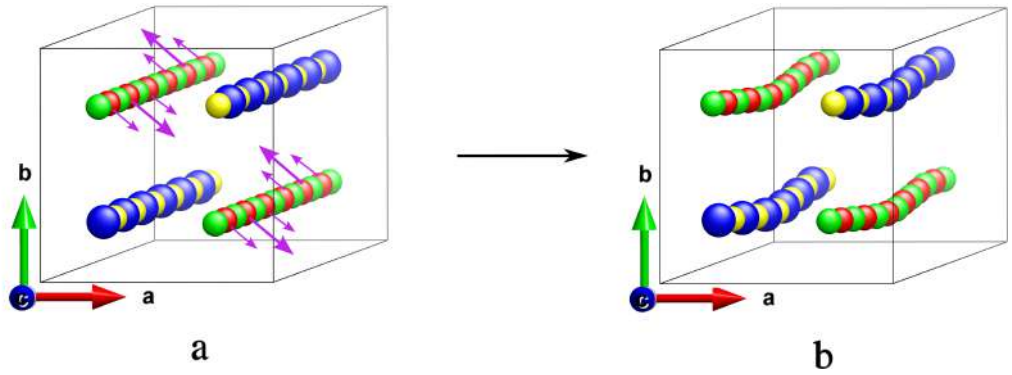

Figure 5.4: Top view of crystal structure for (a) $T > T_{CDW1}$ (b) $T < T_{CDW2}$

for the modulated structure have been unfolded onto the Brillouin zone of the high temperature structure. A small gap opening is found in the RX direction parallel to the c direction, while the other directions remain metallic. In Fig5.5a the high temperature band is shown in black color, while the red points are the modulated supercell band weights along the same primitive cell Brillouin zone RX direction. The size of the red points indicate the weight of the unfolded band at that $\boldsymbol{k}$ point.

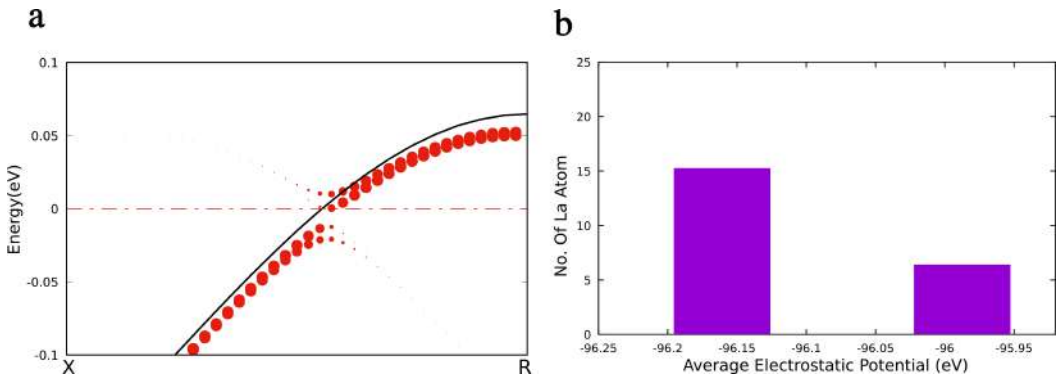

Figure 5.5: (a)Band structure of the modulated supercell unfolded onto the high temperature structure X to R direction (b)Histogram plot of no. of La atoms in the CDW structure as a function of their average electrostatic potential.

Furthermore, we have calculated the electrostatic potential around each atom. Then plotted the number of La atoms according to their electrostatic potential in a histogram. The histogram is shown in Fig: 5.5b. Clearly, two distinct types of La atom has emerged due to the modulation. This matches with the NMR studies done on the system providing more validation to the obtained CDW distortions.

5.4 Conclusion

Considering $LaAgSb_2$, a material with multiple CDW transitions, we have calculated the exfoliation energy to show that it is potentially exfoliable. Phonon calculation reveals the presence of low frequency shear and compression modes in the material allowing for layer sliding and compression as well. As the c parameter decreases with temperature, the repulsion between electron cloud of vertically stacked Sb and Ag layers increases. To minimize the forces, the layers slide perpendicular to the c lattice vector and commensurate periodical modulations are found. Consequently, the electronic band dispersion along the **RX** direction (parallel to c) of the BZ reveals opening of a small gap upon unfolding the band structure onto the brillouin zone of the high temperature structure. Furthermore, our modulated structure also reveals emergence of two different types of La atoms matching well with previous studies.

Bibliography

[1] C. Song, Jaehyun Park, Japil Koo, K.-B. Lee, J. Y. Rhee, S. L. Bud'ko, P. C. Canfield, B. N. Harmon, and A. I. Goldman. Charge-density-wave orderings in laagsb$_2$: an x-ray scattering study. *Phys. Rev. B*, 68:035113, Jul 2003.

[2] X. Shi, P. Richard, Kefeng Wang, M. Liu, C. E. Matt, N. Xu,

R. S. Dhaka, Z. Ristic, T. Qian, Y.-F. Yang, C. Petrovic, M. Shi, and H. Ding. Observation of dirac-like band dispersion in laagsb$_2$. *Phys. Rev. B*, 93:081105, Feb 2016.

[3] M. D. Johannes, I. I. Mazin, and C. A. Howells. Fermi-surface nesting and the origin of the charge-density wave in Nbse$_2$. *Phys. Rev. B*, 73:205102, May 2006.

[4] M. D. Johannes and I. I. Mazin. Fermi surface nesting and the origin of charge density waves in metals. *Phys. Rev. B*, 77:165135, Apr 2008.

[5] Seung-Ho Baek, Sergey L. Bud'ko, Paul C. Canfield, F. Borsa, and Byoung Jin Suh. Nmr evidence for a peierls transition in the layered square-net compound laagsb$_2$. *Phys. Rev. B*, 106:195153, Nov 2022.

[6] P. E. Blöchl. Projector augmented-wave method. *Phys. Rev. B*, 50:17953–17979, Dec 1994.

[7] G. Kresse and D. Joubert. From ultrasoft pseudopotentials to the projector augmented-wave method. *Phys. Rev. B*, 59:1758–1775, Jan 1999.

[8] W. Kohn. Nobel lecture: Electronic structure of matter—wave functions and density functionals. *Rev. Mod. Phys.*, 71:1253–1266, Oct 1999.

[9] G. Kresse and J. Hafner. Ab initio molecular dynamics for liquid metals. *Phys. Rev. B*, 47:558–561, Jan 1993.

[10] G. Kresse and J. Furthmüller. Efficient iterative schemes for ab initio total-energy calculations using a plane-wave basis set. *Phys. Rev. B*, 54:11169–11186, Oct 1996.

[11] G. Kresse and J. Furthmüller. Efficiency of ab-initio total energy calculations for metals and semiconductors using a plane-wave basis set. *Computational Materials Science*, 6(1):15–50, 1996.

[12] John P. Perdew, Kieron Burke, and Matthias Ernzerhof. Generalized gradient approximation made simple. *Phys. Rev. Lett.*, 77:3865–3868, Oct 1996.

[13] Atsushi Togo and Isao Tanaka. First principles phonon calculations in materials science. *Scripta Materialia*, 108:1–5, 2015.

[14] Atsushi Togo. First-principles phonon calculations with phonopy and phono3py. *Journal of the Physical Society of Japan*, 92:012001, 2023.

[15] Rafiqul Alam, Prasun Boyal, Shubhankar Roy, Ratnadwip Singha, Buddhadeb Pal, Riju Pal, Prabhat Mandal, Priya Mahadevan, and Atindra Nath Pal. Detection of nontrivial topology driven by charge density wave in a semi-dirac metal. *Advanced Functional Materials*, 33(44):2306751, 2023.

[16] N. Mounet, P. Gibertini, M.and Schwaller, D. Campi, A. Merkys, A. Marrazzo, T. Sohier, I. E. Castelli, A. Cepellotti, G. Pizzi, and Marzari N. Two-dimensional materials from high-throughput computational exfoliation of experimentally known compounds. *Nature Nanotech*, 13:246–252, 2018.

[17] K. H. Michel and B. Verberck. Rigid-plane phonons in layered crystals. *physica status solidi (b)*, 249(12):2604–2607, 2012.

CHAPTER 6

Probing non trivial topology through PHE

"Once you have eliminated the impossible, whatever remains, no matter how improbable, must be the truth"

Sir Arthur Conan Doyle

6.1 Introduction

Apart from the CDW transitions as discussed in chapter 5 , another intriguing aspect of $LaAgSb_2$ is the observation of unsaturated quasi-linear magneto resistance(MR) with distinct features above and below the CDW transitions [1]. The origin of the unsaturated quasi-linear MR at low temperature is still elusive. For an material with isotropic Dirac cone, it has been simply attributed to the quantum limit of the possible Dirac fermions [2] at a relatively low field, while for systems with an anisotropic and tilted Dirac cone, it has been predicted to arise whenever there is non vanishing Berry curvature, indicating the topological nature of the electronic bands [3, 4, 5]. $LaAgSb_2$, as seen in the previous chapter, is an example of a square net compound, a structure type in which several inter-metallic compounds have been found to be topological semi-metals [6, 7, 8]. Apart from hosting multiple CDW transitions [9], $LaAgSb_2$ also have multiple tilted Dirac cones near Fermi energy which have been confirmed

by ARPES measurements [10, 11] and first principle calculations [1]. It is naturally expected that the interplay between the low energy Dirac cones and the chiral metallic structure at low temperature will lead to exotic ground states. In the following sections we discuss this aspect by using planar Hall effect (PHE) signal as a probe.

PHE, which is defined as the transverse voltage when the magnetic field and electric field are co-planar, has recently emerged as a transport-based probe to detect the non-trivial bands[12, 13] in various topological semi-metals or insulators, such as ZrTe5 [14], Cd_3As_2 [15], GdPtBi [16], VaI_3[17], Ta_3SiTe_6[18], Bi_2Se_3[19], $PrRhC_2$[20] and SmB_6 [21]. Experimentally, an anomaly in the zero-field resistivity and ordinary Hall coefficient at approximately 211 K have been observed, suggesting the reconstruction of the Fermi surface mediated by the CDW transition [22]. However, the most intriguing result is the observation of PHE from low temperature to room temperature with a change of sign in the amplitude of the PHE above and below the first CDW transition ($\approx$ 211 K). Sign reversal of the PHE suggests different mechanism must be at play in the two regime.

We have calculated the electronic band structure for both normal and CDW modulated phase. By mapping the *ab initio* results onto a tight binding model we have showed that the broken inversion symmetry in the chiral structure in low temperature splits the Dirac cone into Weyl cones giving rise to finite Berry Curvature. This explains the PHE signal in the low temperature regime through chiral anomaly as has been discussed in the literature [12, 13]. In the high temperature however, the the absence of Berry curvature makes the PHE signal rather unusual. It possibly arises from the coupling of in plane magnetic field with the anisotropic Dirac cone as has been previously reported in a theoretical model calculation [23] .

6.2 Computational Methods

6.2.1 Band Structure Calculation

The *ab initio* band structure was calculated by projector augmented wave method [24, 25] implementation of density function theory [26] within the Vienna Ab initio Simulation Package (VASP) [27, 28, 29]. The Perdew – Burke – Ernzerhof GGA potentials [30] were used for the exchange correlation functional. Taking the initial charge density for the geometrically relaxed structures described in chapter 5, the energy eigenvalues have been calculated along the straight lines joining different high symmetry points of the Brillouin Zone.

6.2.2 Tight Binding Fit

The effective tight binding model was obtained by constructing maximally localized Wannier functions (MLWF) [31, 32] implemented in WANNIER90 [33]. The basis of the tight binding Hamiltonian consisted of d orbitals of La and Ag and p orbitals of Sb atoms. Spin orbit interactions have been considered while constructing the Wannier functions. The Berry Curvature was calculated within the WANNIER TOOLS [34] package. A 501×501 grid has been used to interpolate the Berry curvature across the 2D slice of the Brillouin zone.

6.3 Results and Discussions

6.3.1 Experimental observations of PHE

In order to measure the planar Hall signal, the magnetic field was rotated in a way such that the current and magnetic field always

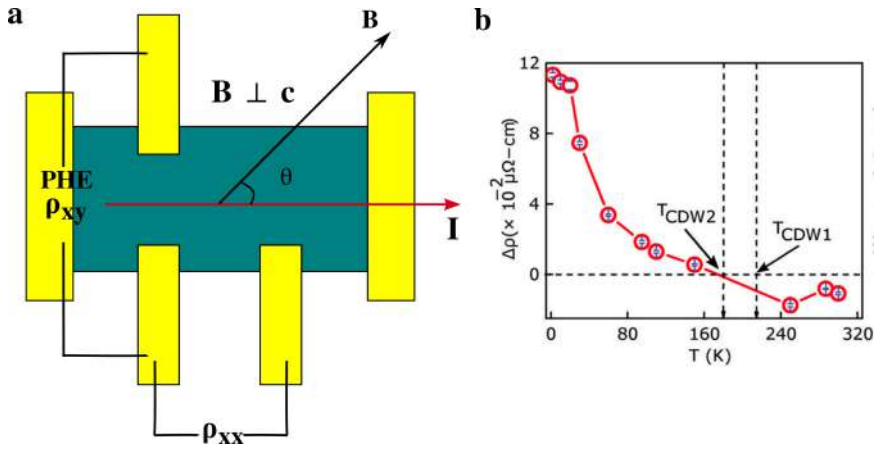

Figure 6.1: (a) Experimental configuration of PHE measurement set-up, (b) Temperature dependence of $\Delta\rho(B = 9T) = \rho_{\perp} - \rho_{\parallel}$, extracted from the fitting of the PHE signal using equation 6.1 (reproduced from [22])

remains in the same plane and the Hall resistivity and magneto resistance (MR) at different angles between the current and magnetic field (θ) was measured. The device schematic is shown in Fig: 6.1a. The PHE signal for the given geometry is defined as,

$$\rho_{xy}^{PHE} = -\Delta\rho sin(\theta)cos(\theta) \tag{6.1}$$

Where, $\Delta\rho = \rho_{\perp} - \rho_{\parallel}$ with $\rho_{\perp}$ and $\rho_{\parallel}$ being the sheet resistance in the perpendicular and parallel direction to the magnetic field respectively. The obtained PHE signal is fitted with equation (6.1) and the amplitude $\Delta\rho$ is extracted. As shown in the Fig:6.1b by plotting $\Delta\rho$ vs. T , the amplitude changes sign from negative to positive at the first CDW transition at approximately 210 K.

6.3.2 Theoretical understanding of PHE

Above CDW

The high temperature structure, shown in Fig. 5.1 , is centrosymmetric. Furthermore the absence of magnetism in the material

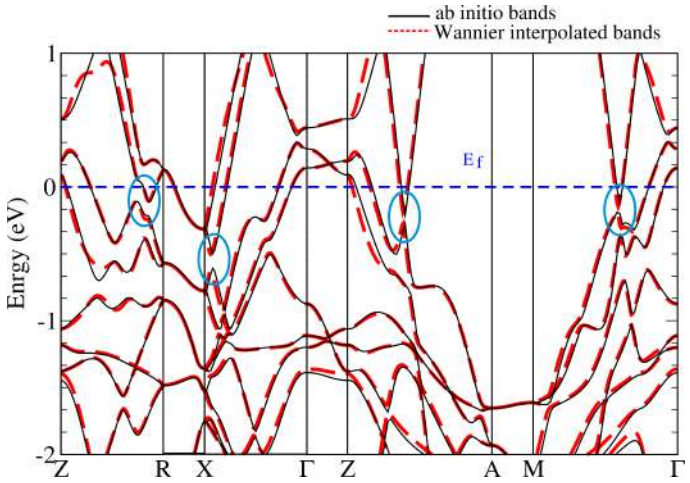

Figure 6.2: *ab initio*(black solid line) and tight binding fitted (red dashed lines) electronic band structure of $LaAgSb_2$ including spin orbit interactions. The zero of the energy is Fermi energy (indicated by the blue dashed line). The linear band dispersions in the vicinity of the Fermi level have been indicated by the blue circles.

makes the system symmetric under time reversal. Combination of these two symmetry ensures that the Berry curvature is zero at every $\boldsymbol{k}$-point. This hints at a non-topological origin in the PHE above the CDW transition. In order to understand the origin of PHE signal in a non magnetic, inversion symmetric material, we have first studied the electronic band structure in high temperature phase in detail.

The calculated band dispersion along various high symmetry directions is shown in Fig: 6.2 in which black solid lines are *ab initio* results and superposed red dashed lines indicate the tb fitted band structure obtained through wannier interpolation. The band structure reveals multiple Dirac cones near the Fermi energy matching with previous studies. In 6.3a one such crossing along the $M\Gamma$ direction is shown where the bands forming the Dirac cone are depicted in red color. The Dirac cone has a gap of 40 meV. The Dirac cone is anisotropic in nature as shown in 6.3b . The anisotropic nature plays a crucial role for finite PHE signal above CDW transition as

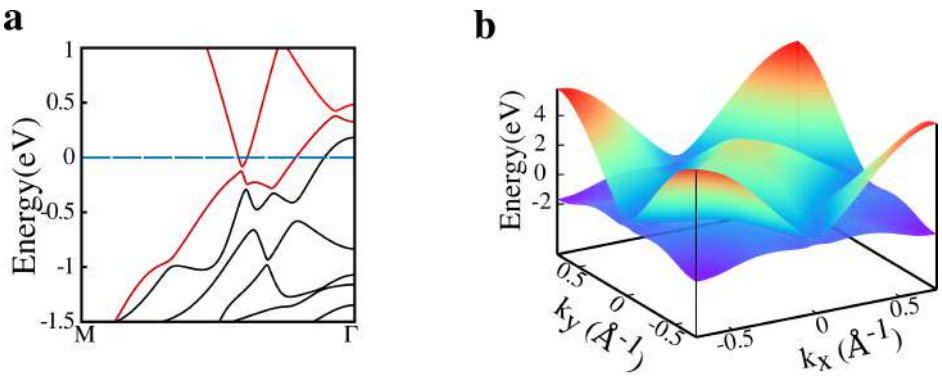

Figure 6.3: (a)The electronic band structure along the $M - \Gamma$ direction with red bands showing the linearly dispersive bands (zero energy corresponds to the Fermi energy). (b) Dispersion of the bands that crosses the Fermi energy in across the $k_z = 0$ plane of the Brillouin zone.

discussed below.

In plane magnetic field have no physical effect on an isotropic Dirac cone, which is linear in all direction with same Fermi velocity for electron and hole band, as on application of such magnetic field the Dirac cone only change its position in the reciprocal space with same Fermi velocity. However, the situation is completely different for a material with anisotropic Dirac cone like $LaAgSb_2$. The in plane magnetic field couples with the anisotropic part of the Dirac cone and breaks the time reversal symmetry parallel to the field. Consequently, back scattering between states at $\boldsymbol{k}$ and -$\boldsymbol{k}$ is allowed in the direction parallel to the in-plane magnetic field, while that is not the case in the direction perpendicular to the field [23]. This is shown schematically in 6.4. The black dot indicate possible source (impurity) of scattering, the blue dot represents electron. The black circle (ellipse) are Fermi surface of an isotropic (anisotropic) Dirac cone. In 6.4a in plane magnetic field does not allow back scattering between electrons with crystal momentum $\boldsymbol{k}$ and $-\boldsymbol{k}$ as the orthogonality of spin character $|s_{\boldsymbol{k}}\rangle$ and $|s_{-\boldsymbol{k}}\rangle$ remains intact. However, for anisotropic Dirac

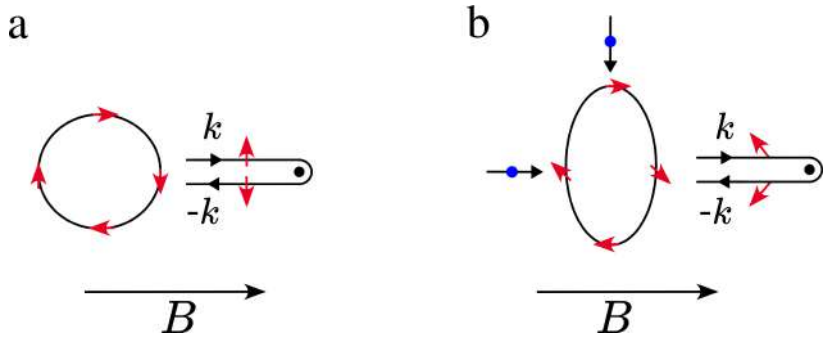

Figure 6.4: (a) Circular Fermi surface of a isotropic Dirac cone. Back scattering of the impurity (black dot) is not allowed as $|s_{\boldsymbol{k}}\rangle$ and $|s_{-\boldsymbol{k}}\rangle$ remains orthogonal in all direction. (b) For elliptical Fermi surface of an anisotropic Dirac cone the orthogonality $|s_{\boldsymbol{k}}\rangle$ and $|s_{-\boldsymbol{k}}\rangle$ breaks along the the direction of the magnetic field $\boldsymbol{B}$. (reproduced from [23])

cone (6.4b) $|s_{\boldsymbol{k}}\rangle$ and $|s_{-\boldsymbol{k}}\rangle$ are not orthogonal along the direction of the magnetic field allowing back scattering. Due to this anisotropic response to the in plane field, the resistivity in the parallel direction ($\rho_{\parallel}$) increases while the perpendicular sheet resistance ($\rho_{\perp}$) does not change. As a result, the PHE signal , defined by $\Delta\rho = \rho_{\perp} - \rho_{\parallel}$ becomes finite with a negative amplitude.

Below CDW

In order to understand the large magnitude of PHE signal in the low temperature region, we have taken the chiral structure obtained as the CDW modulated structure in the previous chapter and calculated its electronic band structure. The band dispersion along the $M\Gamma$ direction of the supercell Brillouin zone, shown in 6.5, shows the emergent Weyl cones as a consequence of broken inversion symmetry in the chiral structure. Furthermore, the Weyl cones are observed to be tilted. For such case, assuming the electric field is applied along the x-axis, the perpendicular and parallel conductivity under planar Hall geometry has been derived from modified Boltzmann transport

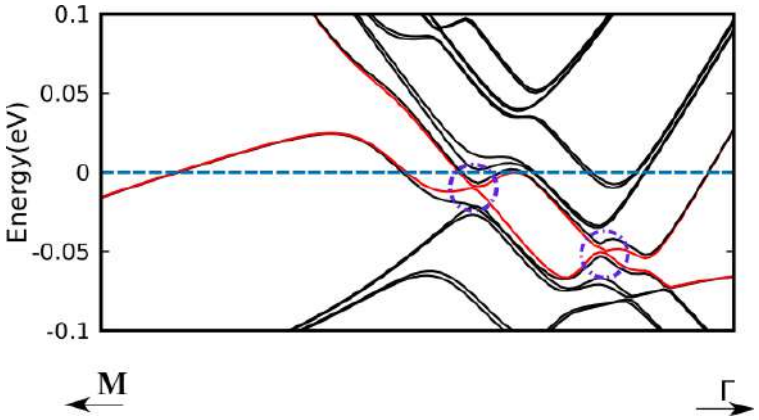

Figure 6.5: Electronic band structure in a small portion of the $M\Gamma$ direction of the Brillouin zone of the low temperature CDW structure. Two doubly degenerate Weyl node emerges as a result of inversion symmetry breaking.

equation[13]. These are given by,

$$\sigma_{\parallel} = \sigma + e^4 \int_{BZ} \frac{d^3k}{(2\pi)^3} \mathcal{D}\tau \left(-\frac{\partial f_{eq}}{\partial \epsilon}\right) \frac{B^2}{\hbar^2} (\boldsymbol{v_k} \cdot \boldsymbol{\Omega_k})^2 \tag{6.2}$$

and,

$$\sigma_{\perp} = \sigma \tag{6.3}$$

Where, $\sigma = \int_{BZ} \frac{d^3k}{(2\pi)^3} \mathcal{D}\tau \left(-\frac{\partial f_{eq}}{\partial \epsilon}\right) v_x$ is the Drude conductivity of the sample, τ is the average relaxation time of electron, $\mathcal{D} = [1 + \frac{e}{\hbar}\boldsymbol{B} \cdot \boldsymbol{\Omega_k}]^{-1}$ is the phase space volume correction due to finite Berry curvature ($\boldsymbol{\Omega_k}$) in the presence of the magnetic field ($\boldsymbol{B}$), f_{eq} is the equilibrium Fermi-Dirac distribution function and $\boldsymbol{v_k}$ is the group velocity of the Bloch electrons. Physically this means that the coupling of the finite Berry curvature in the presence of magnetic field generates extra conductivity channels along the applied magnetic field. This phenomenon known as "chiral anomaly" explains the positive amplitude PHE signal observed in the experiment as the resistivity, defined to be the inverse of the conductivity, decreases in the parallel direction. Thereby producing large positive amplitude PHE signal,

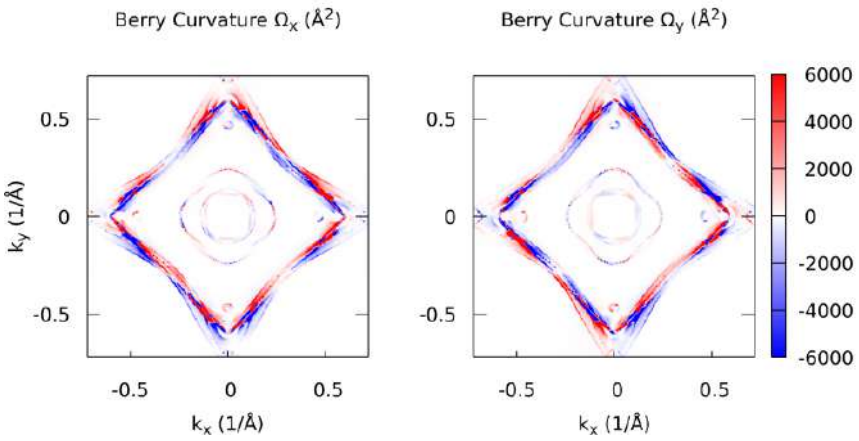

Figure 6.6: 2D color plots of the x (left) and y (right) component of Berry curvature in $k_z = 0$ plane in the CDW phase

defined to be $\Delta\rho = \rho_\perp - \rho_\parallel$.

To validate the mechanism described above for the CDW modulate chiral structure, we have calculated the Berry curvature at a 2D slice of the Brillouin zone, defined by $k_z = 0$. The finite x and y component of the Berry curvature is shown in 6.6. The red and blue colour indicates in the figure positive and negative value of Berry curvature. Although the Berry curvature still vanishes globally due to the coexistence of positive and negative region, manifesting the presence of time reversal symmetry in the CDW structure, locally it has large finite value. From the expression in (6.2), one finds that the extra conductivity term due to chiral anomaly adds up from both positive and negative Berry curvature contributions, enhancing the PHE signal in the CDW structure.

6.4 Conclusion

We have used the chiral CDW structure of $LaAgSb_2$, which we have found to be stable at the low temperature, in order to explain the

planar Hall data obtained by our collaborators. The high temperature structure being centero-symmetric and non-magnetic, have zero Berry curvature at every point in the k-space. However, we have shown the presence of anisotropic Dirac cones in the system, which produce the planer hall signal in high temperature regime due to the anisotropic response to the in-plane magnetic field. We have explained this mechanism is consistent with the negative amplitude PHE observed. However due to broken inversion symmetry, Berry curvature is finite locally in the low temperature chiral structure which we had found by layer sliding. Furthermore, we have shown that the Dirac cone splits into Weyl cones making the low temperature structure a topologically distinct phase. Consequently, extra conductivity channel parallel to the in plane magnetic field are accessible in the low temperature regime thereby reducing the parallel resistivity and producing positive amplitude enhanced PHE signal.

Bibliography

[1] Kefeng Wang and C. Petrovic. Multiband effects and possible dirac states in laagsb$_2$. *Phys. Rev. B*, 86:155213, Oct 2012.

[2] A. A. Abrikosov. Quantum magnetoresistance. *Phys. Rev. B*, 58:2788–2794, Aug 1998.

[3] Kamal Das and Amit Agarwal. Linear magnetochiral transport in tilted type-i and type-ii weyl semimetals. *Phys. Rev. B*, 99:085405, Feb 2019.

[4] Anirban Kundu, Zhuo Bin Siu, Hyunsoo Yang, and Mansoor B A Jalil. Magnetotransport of weyl semimetals with tilted dirac cones. *New Journal of Physics*, 22(8):083081, aug 2020.

[5] Di Xiao, Junren Shi, and Qian Niu. Berry phase correction to

electron density of states in solids. *Phys. Rev. Lett.*, 95:137204, Sep 2005.

[6] Sebastian Klemenz, Shiming Lei, and Leslie M. Schoop. Topological semimetals in square-net materials. *Annual Review of Materials Research*, 49(1):185–206, 2019.

[7] Shiming Lei, Teicher, et al. Band engineering of dirac semimetals using charge density waves. *Advanced Materials*, 33(30):2101591, 2021.

[8] Ratnadwip Singha, Arnab Kumar Pariari, Biswarup Satpati, and Prabhat Mandal. Large nonsaturating magnetoresistance and signature of nondegenerate dirac nodes in zrsis. *Proceedings of the National Academy of Sciences*, 114(10):2468–2473, 2017.

[9] C. Song, Jaehyun Park, Japil Koo, K.-B. Lee, J. Y. Rhee, S. L. Bud'ko, P. C. Canfield, B. N. Harmon, and A. I. Goldman. Charge-density-wave orderings in laagsb$_2$: an x-ray scattering study. *Phys. Rev. B*, 68:035113, Jul 2003.

[10] T. Arakane, T. Sato, S. Souma, T. Takahashi, Y. Watanabe, and Y. Inada. Electronic structure of laagsb2 and ceagsb2 studied by high-resolution angle-resolved photoemission spectroscopy. *Journal of Magnetism and Magnetic Materials*, 310(2, Part 1):396–398, 2007. Proceedings of the 17th International Conference on Magnetism.

[11] X. Shi, P. Richard, Kefeng Wang, M. Liu, C. E. Matt, N. Xu, R. S. Dhaka, Z. Ristic, T. Qian, Y.-F. Yang, C. Petrovic, M. Shi, and H. Ding. Observation of dirac-like band dispersion in laagsb$_2$. *Phys. Rev. B*, 93:081105, Feb 2016.

[12] A. A. Burkov. Giant planar hall effect in topological metals. *Phys. Rev. B*, 96:041110, Jul 2017.

[13] S. Nandy, Girish Sharma, A. Taraphder, and Sumanta Tewari. Chiral anomaly as the origin of the planar hall effect in weyl semimetals. *Phys. Rev. Lett.*, 119:176804, Oct 2017.

[14] P. Li, C. H. Zhang, J. W. Zhang, Y. Wen, and X. X. Zhang. Giant planar hall effect in the dirac semimetal $ZrTe_{5-\delta}$. *Phys. Rev. B*, 98:121108, Sep 2018.

[15] Hui Li, Huan-Wen Wang, Hongtao He, Jiannong Wang, and Shun-Qing Shen. Giant anisotropic magnetoresistance and planar hall effect in the dirac semimetal cd_3as_2. *Phys. Rev. B*, 97:201110, May 2018.

[16] Nitesh Kumar, Satya N. Guin, Claudia Felser, and Chandra Shekhar. Planar hall effect in the weyl semimetal gdptbi. *Phys. Rev. B*, 98:041103, Jul 2018.

[17] Ratnadwip Singha, Shubhankar Roy, Arnab Pariari, Biswarup Satpati, and Prabhat Mandal. Planar hall effect in the type-ii dirac semimetal val_3. *Phys. Rev. B*, 98:081103, Aug 2018.

[18] Shubhankar Roy, Ratnadwip Singha, Arup Ghosh, and Prabhat Mandal. Signature of topological nontrivial band structure in ta_3Site_6. *Phys. Rev. Mater.*, 5:064203, Jun 2021.

[19] Yang Wang, Sivakumar V. Mambakkam, Yue-Xin Huang, Yong Wang, Yi Ji, Cong Xiao, Shengyuan A. Yang, Stephanie A. Law, and John Q. Xiao. Observation of nonlinear planar hall effect in magnetic insulator - topological insulator heterostructures. *Phys. Rev. B*, 106:155408, Oct 2022.

[20] Banasree Sadhukhan and Tanay Nag. Effect of chirality imbalance on hall transport of $prrhc_2$. *Phys. Rev. B*, 107:L081110, Feb 2023.

[21] L. Zhou, B. C. Ye, H. B. Gan, J. Y. Tang, P. B. Chen, Z. Z. Du, Y. Tian, S. Z. Deng, G. P. Guo, H. Z. Lu, F. Liu, and H. T. He. Surface-induced positive planar hall effect in topological kondo insulator smb_6 microribbons. *Phys. Rev. B*, 99:155424, Apr 2019.

[22] Rafiqul Alam, Prasun Boyal, Shubhankar Roy, Ratnadwip Singha, Buddhadeb Pal, Riju Pal, Prabhat Mandal, Priya Mahadevan, and Atindra Nath Pal. Detection of nontrivial topology driven by charge density wave in a semi-dirac metal. *Advanced Functional Materials*, 33(44):2306751, 2023.

[23] Shi-Han Zheng, Hou-Jian Duan, Jia-Kun Wang, Jia-Yu Li, Ming-Xun Deng, and Rui-Qiang Wang. Origin of planar hall effect on the surface of topological insulators: Tilt of dirac cone by an in-plane magnetic field. *Phys. Rev. B*, 101:041408, Jan 2020.

[24] P. E. Blöchl. Projector augmented-wave method. *Phys. Rev. B*, 50:17953–17979, Dec 1994.

[25] G. Kresse and D. Joubert. From ultrasoft pseudopotentials to the projector augmented-wave method. *Phys. Rev. B*, 59:1758–1775, Jan 1999.

[26] W. Kohn. Nobel lecture: Electronic structure of matter—wave functions and density functionals. *Rev. Mod. Phys.*, 71:1253–1266, Oct 1999.

[27] G. Kresse and J. Hafner. Ab initio molecular dynamics for liquid metals. *Phys. Rev. B*, 47:558–561, Jan 1993.

[28] G. Kresse and J. Furthmüller. Efficient iterative schemes for ab initio total-energy calculations using a plane-wave basis set. *Phys. Rev. B*, 54:11169–11186, Oct 1996.

[29] G. Kresse and J. Furthmüller. Efficiency of ab-initio total energy calculations for metals and semiconductors using a plane-wave basis set. *Computational Materials Science*, 6(1):15–50, 1996.

[30] John P. Perdew, Kieron Burke, and Matthias Ernzerhof. Generalized gradient approximation made simple. *Phys. Rev. Lett.*, 77:3865–3868, Oct 1996.

[31] Nicola Marzari and David Vanderbilt. Maximally localized generalized wannier functions for composite energy bands. *Phys. Rev. B*, 56:12847–12865, Nov 1997.

[32] Ivo Souza, Nicola Marzari, and David Vanderbilt. Maximally localized wannier functions for entangled energy bands. *Phys. Rev. B*, 65:035109, Dec 2001.

[33] Arash A. Mostofi, Jonathan R. Yates, Giovanni Pizzi, Young-Su Lee, Ivo Souza, David Vanderbilt, and Nicola Marzari. An updated version of wannier90: A tool for obtaining maximally-localised wannier functions. *Computer Physics Communications*, 185(8):2309–2310, 2014.

[34] QuanSheng Wu et al. Wanniertools: An open-source software package for novel topological materials. *Computer Physics Communications*, 224:405–416, 2018.

Part IV

Materials With 3D Crystal Lattices

CHAPTER 7

Robust Antiferromagnetism in $NaOsO_3$ Under Pressure

"Entities are not be multiplied without necessity"

William of Ockham's

7.1 Introduction

$NaOsO_3$ has played a crucial role in the study of metal-insulator transitions (MIT) over the last decade. The MIT in $NaOsO_3$ is also accompanied by a long-range, collinear G-type antiferromagnetic (AFM) ordering [1, 2]. The transition temperature is 410 K as determined in neutron diffraction experiments [1]. At high temperatures, $NaOsO_3$ behaves like a paramagnetic Fermi liquid. As temperature is lowered the onset of AFM ordering is believed to open a small band gap of 0.1 eV [3] . Further experiments have revealed that the structural parameters change continuously and the cell symmetry does not change across the transition temperature [2]. Moreover, the effect of spin-orbit coupling (SOC) in $NaOsO_3$ is expected to be small as Os^{5+} has half-filled t_{2g} orbitals, which quenches the orbital angular moment. The effects of electron correlations (U) are also expected to be small due to the extended nature of $5d$ orbitals on Os. This has been confirmed in magnetic resonance x-ray spectroscopy exper-

iments [2]. These observations support the case for the mechanism proposed by Slater [4], i.e. the onset of antiferromagnetic ordering, being responsible for the MIT in $NaOsO_3$.

However, later theoretical studies have shown that SOC may be renormalising the correlation energy in $NaOsO_3$ [5]. Resonant inelastic x-ray spectroscopy measurements [6, 7] of this material have revealed that the spin wave excitation in $NaOsO_3$ has a 60 meV gap, a puzzling effect as the spin excitation gap is generally known to arise from SOC-induced anisotropy. Furthermore, inelastic neutron scattering study [8] suggests strong spin-phonon coupling in $NaOsO_3$ resulting in an unusually high phonon frequency shift of 40 cm^{-1}. Based on these results, different mechanisms have been employed to explain the MIT in $NaOsO_3$, where cooperation between electron, spin, and phonon degrees of freedom become important. In a recent study, pressure-dependent transport measurements have shown that the small indirect bandgap of 0.1 eV in $NaOsO_3$ is persistent up to 20 GPa and theoretical calculation within DFT+U have revealed that the magnetic moments on Os atoms decrease very sluggishly as pressure increases. This readily hints at some competing effects in the system, arising from application of pressure that makes the magnetic moment and the insulating state robust.

In this project, we have performed *ab initio* calculations and constructed a model Hamiltonian to understand how pressure changes the electronic and magnetic ground state in $NaOsO_3$. Our calculations show that the robust insulating state and AFM ordering arises from competing effects of Os-O bond length shortening and the angle between Os-O-Os deviating more from 180°. While shorter bond lengths between Os and O helps the AFM ordering through superexchange, the deviation of Os-O-Os angle from 180° makes the AFM

ordering weak. The exchange interactions for neighboring Os atoms have been estimated by mapping *ab initio* energies onto an isotropic Heisenberg model, and the Neel temperature at different pressure have been calculated using Monte-Carlo simulation. Our analysis reveals that even at 40 GPa pressure the Neel temperature is above the room temperature.

7.2 Computational Methods

7.2.1 *ab-initio* Calculations

All *ab-initio* calculations have been performed by a plane-wave projector augmented wave approximation [9, 10] of density functional theory[11] as implemented in VASP[12, 13, 14]. For exchange correlation, PBE functional[15] have been used. Additionally electron correlation effects have been considered by adding $U = 1.0$ eV on the d states of Os within the Dudarev implementation [16] of the DFT+U scheme[17, 18]. For self consistent calculations a Monkhorst-Pack [19] k-mesh of $8 \times 8 \times 8$ k points was used. Cutoff energy of 600 eV has been set for the plane-wave basis states. The difference in energy between different magnetic configurations have converged within 0.12 meV per formula unit with the chosen k-mesh and cut off energy.

7.2.2 Application of Pressure

In order to determine ambient pressure cell parameters, the energy vs volume data is fitted with the Murnaghan equation of state [20]. The fitting curve is depicted in Fig.7.1 where the data points are the computed energy for different unit cell volume and the solid continuous line is the fitted Murnaghan equation of state given by,

$$E(V) = E_0 + k_0 V_0 \left[\frac{1}{B_0'(B_0' - 1)} \left(\frac{V}{V_0} \right)^{1-B_0'} + \frac{1}{B_0'} \frac{V}{V_0} - \frac{1}{B_0' - 1} \right] \quad (7.1)$$

where, V_0 and E_0 are respectively the equilibrium cell volume and the *ab initio* energy at that cell volume. B_0 and B_0' are equilibrium bulk modulus and its pressure derivative respectively. From the fitted data, the equilibrium unit cell volume is found to be 223.8940 Å^3. The bulk modulus obtained from the fitting is 152.20 GPa with a pressure derivative of 4.11 which matches well with previous studies [21]. The lattice parameters in ambient conditions are found to be $a = 5.44$ Å , $b = 7.65$ Å and $c = 5.38$ Å. At each pressure value, the atomic positions have been relaxed assuming G-type AFM ordering of Os atoms.

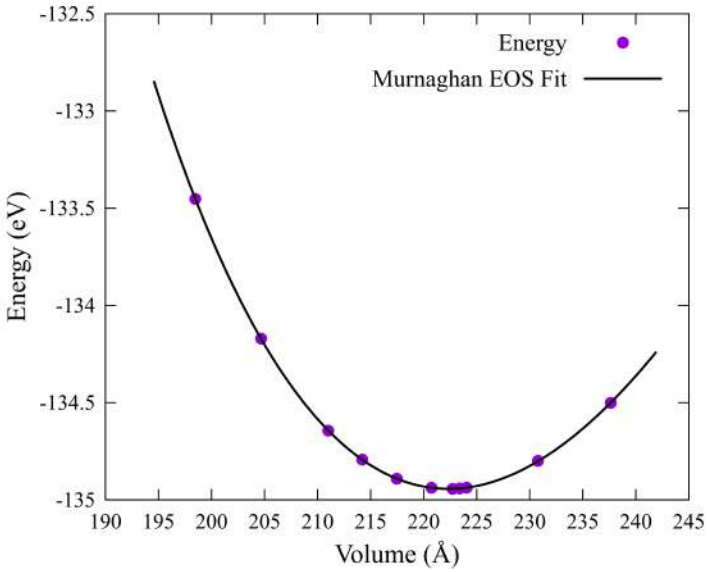

Figure 7.1: Total energy plotted against the unit cell volume. The calculated energies are shown as purple solid circles and the black line is the fitted curve of the data with Murnaghan equation of state[20].

7.2.3 Determination of Isotropic Heisenberg Exchange Interactions

The exchange interactions have been estimated by mapping the magnetic energies onto a minimal isotropic Heisenberg model given

by,

$$\mathcal{H} = -\frac{1}{2}\sum_{i,j} J_{ij}\hat{e}_i \cdot \hat{e}_j \tag{7.2}$$

Where e_i and e_j are unit vector along the moment on site i and j. The exchange interaction between them is denoted by J_{ij}. The calculation scheme based on Fourier transformations as described in chapter 2 is employed to determine the pairwise nearest neighbor interactions. Spin spirals with cone angle, $\theta = \frac{\pi}{2}$ have been constructed. The azimuthal angle of the moment in the n^{th} unit cell is given by $\boldsymbol{q} \cdot \boldsymbol{R_n}$ where $\boldsymbol{q}$ is the propagation vector and R_n the lattice vector defining n^{th} unit cell. Energy of such spin spiral configurations have been obtained using *ab initio* calculation for a grid of $\boldsymbol{q}$ points. The Fourier transforms of the exchange interactions are obtained from the set of the calculated energies. Then the exchange interactions J_{ij} are obtained by performing inverse Fourier transformation. The momentum space integration is performed over a grid size of $10\times10\times10$. All numerical integrations, performing the inverse Fourier transformations, have converged within 0.01 meV.

7.3 Results and Discussions

7.3.1 Density of States of the Half Filled t_{2g} Orbitals

The expected behavior of a material under Slater's proposed mechanism of MIT driven by magnetic ordering is shown schematically in Fig. 7.2. Due to antiferromagnetic ordering, up spin sub-lattice experiences different periodic potential than the down spin sub-lattice making the energy of the up spins lower than the down spins for that sub-lattice. Consequently, an energy gap is created splitting the energy band at the magnetic Brillouin zone boundary. In the case of

a half filled valence band, the lower energy split band will be completely filled and the higher energy band will be empty. As a result the paramagnetic metal phase undergoes a metal insulator transition to become an insulating antiferromagnet.

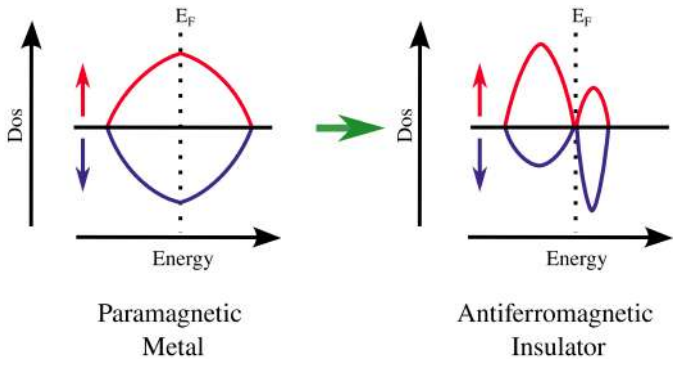

Figure 7.2: Slater mechanism for metal insulator transition

As the temperature driven MIT in $NaOsO_3$ is widely believed to be a realisation of the Slater mechanism, we first studied the density of states of Os d orbitals as a function of applied pressure across the transition. As mentioned before the t_{2g} orbitals on Os are half-filled. However, due to structural distortions, the occupied orbitals might not be pure t_{2g} states, rather an admixture of e_g and t_{2g} states might contribute in the same energy window. The evolution of density of states of a Os atom has been shown in Fig: 7.3. The red and blue line indicate majority and minority carriers respectively. At zero pressure one finds the material to be insulating with a calculated band gap of 0.1 eV. Furthermore, the magnetic calculation reveals the expected G-type antiferromagnetic order. As the pressure increases on the material, the density of states moves rigidly and the gap decreases. At 20 GPa the gap closes, and the system becomes metallic. However, in stark contrast to the general description of a Slater insulator in Fig:7.2, we found that the magnetization does not vanish upon the

gap closure. Rather the density of states under pressure reveals that the magnetization of Os atoms is prominent even in the metallic phase up to a pressure of 40 GPa.

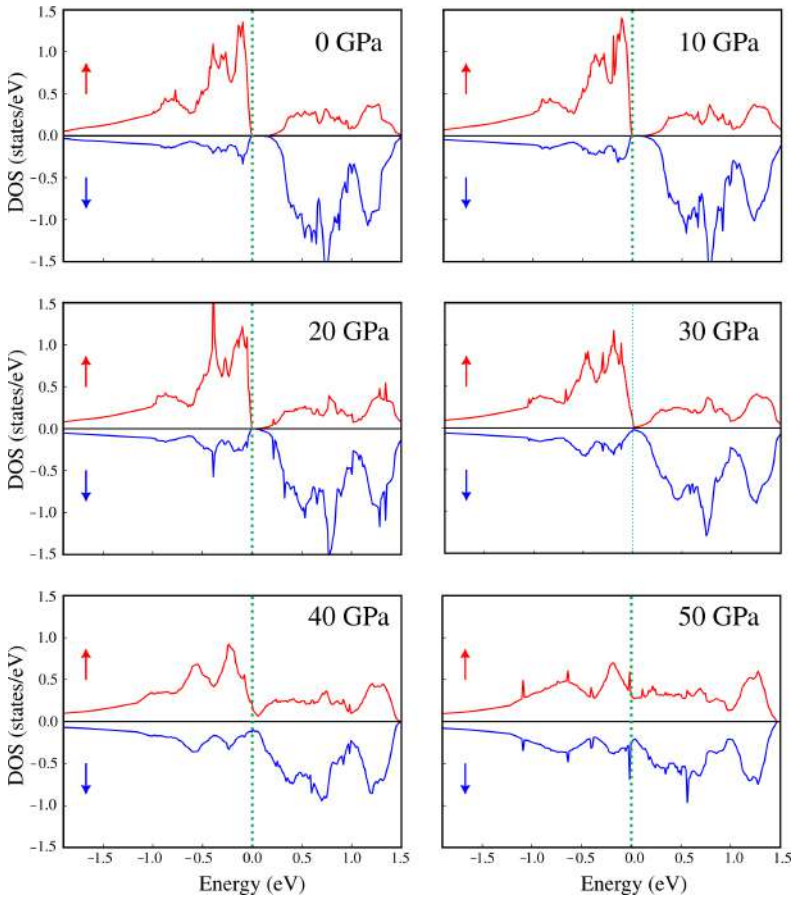

Figure 7.3: Evolution of density of states of Os *d* orbitals under pressure. Red and blue line correspond to the majority and minority spins.

7.3.2 Effect of Pressure on the Electronic Structure

To understand the pressure driven transition and antiferromagnetic metallic state, the electronic band structure have been calculated at different pressure values. The electronic band structure with the G-type antiferromagnetic ordering in the presence of spin orbit

interactions is shown as a function of pressure in Fig. 7.4 . At zero pressure we find the material to be an indirect bandgap insulator with the VBM and the CBM at **X** and **Y** points of the Brillouin zone respectively. As pressure on the material increases the band extrema move towards each other and in accordance with the density of states, at 20 GPa, the indirect bandgap vanishes. However the continuous direct gap persists between valence and conduction band for much higher pressures. Finally, at 40 GPa pressure the direct bandgap also vanishes and the material is metallic.

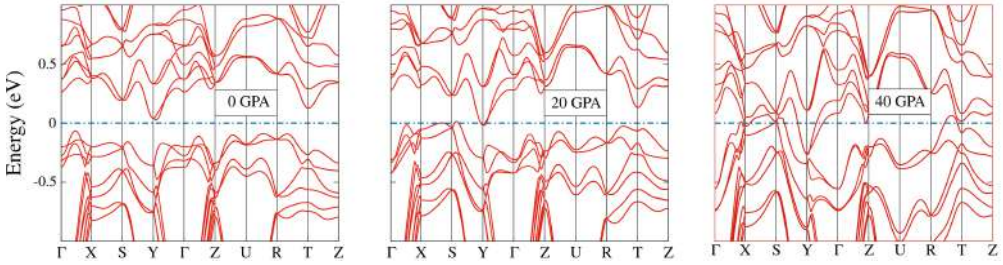

Figure 7.4: Evolution of electronic band structure of NaOsO3 under pressure.

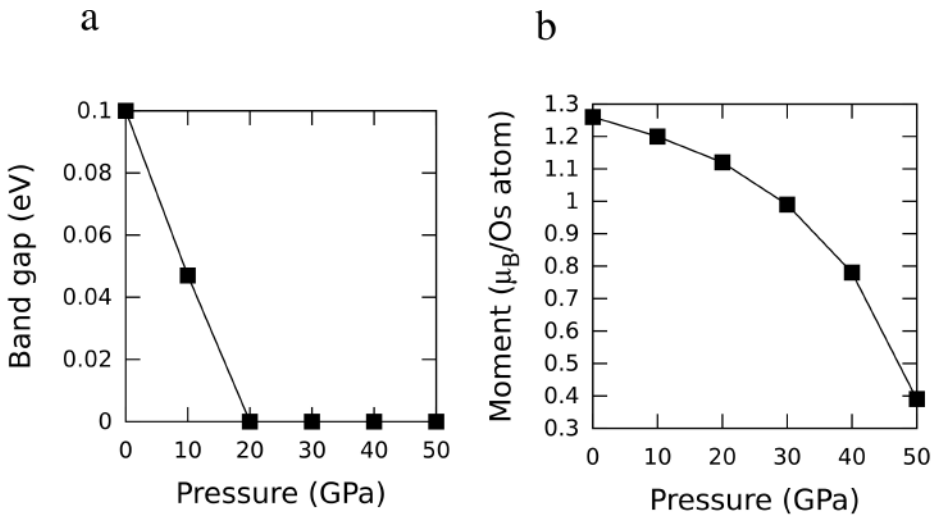

Figure 7.5: (a)Band gap and (b) Magnetic moment per Os atom as a function of applied pressure.

7.3.3 Magnetic Moment and Bandgap Under Pressure

The required pressure of 20 GPa for $NaOsO_3$ to become a metal in-spite of having a relatively small band gap is another surprising result. The evolution of band gap is shown in Fig. 7.5a. The pressure coefficient of band gap, defined to be $\left(\frac{\Delta E}{\Delta P}\right)$, is found to be 0.005 eV/GPa. In table 7.1 This pressure coefficients of band gap for different materials are listed. Evidently, the pressure coefficient of bandgap of $NaOsO_3$ is lower by order of magnitude than that of the materials listed in the table 7.1. The magnetic moment of the Os atoms, which are intimately related with the presence of band gap is also shown in Fig. 7.5b. The moment on Os atom at ambient pressure is found to be $1.26\mu_B$ which is slightly less than the expected value of $\frac{3}{2}\mu_B$ for half-filled t_{2g} orbitals of Os atoms. This can be explained by strong hybridization between d orbitals of Os and p orbitals on the Oxygen. However, the moment on the Oxygen is found to be negligible as the neighboring Os atoms have anti-parallel spins. As the pressure is increased, the moment on the Os atoms decreases rather sluggishly with pressure. At 50 GPa pressure, the moment on the Os atoms remain to be $0.39\mu_B$.

Material	Pressure coefficient of band gap (eV/GPa)
$LaMnO_3$[22]	0.039
$CsMgI_3$[23]	0.05
$Cu_2V_2O_7$ [24]	0.19
$MaSnBr_3$[25]	2
$CsSnBr_3$ [25]	0.16
$Cs_2AgInCl_6$[26]	0.044

Table 7.1: Pressure coefficient of band gap for different materials.

7.3.4 Structural Distortions Under Pressure

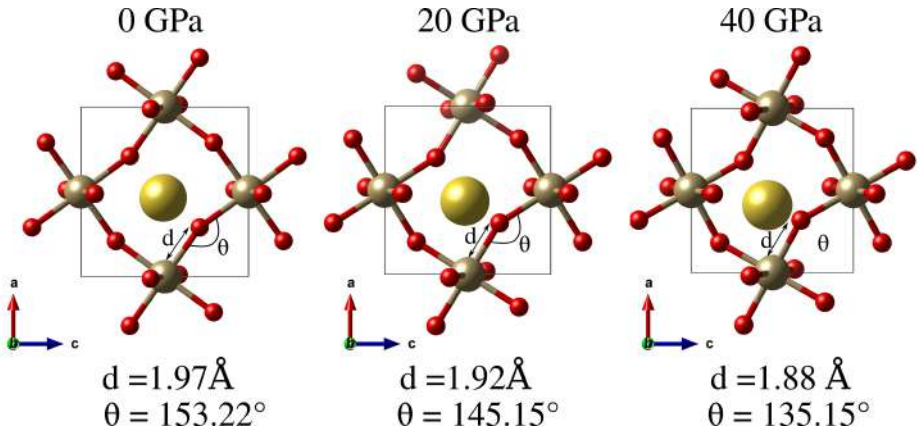

Figure 7.6: Evolution of structural parameters of NaOsO3 under pressure.

In order to probe the robustness of both the insulating state and anti ferromagnetism we concentrate on the structural distortions as a function of the pressure. As the insulating phase is believed to be a direct consequence of AFM ordering, evolution of various structural parameters contributing to the super-exchange pathways under pressure has been studied. In Fig. 7.6 the average Os-O bond length, Os-Os bond length and the Os-O-Os angle are shown as a function of pressure. The Os-O-Os angle at ambient conditions is found to be 153.22°. Under pressure the angle deviates more from 180°. At 40 GPa the angle decreases to 135.15°. As a result the hopping integral and consequently the super-exchange interaction is gradually suppressed with pressure. However, the variation of the bond length reveals that the Os-O bond length also decreases by 0.09 Å within the same pressure range. This implies that as the pressure increases on the unit-cell, not only do the OsO_6 octahedra rotates and thus influencing the Os-O-Os angle but the perovskite cage also shrinks in size shortening the Os-O distance. While the former effect resists the superexchange, the short distance between Os-O increases the hopping

interaction and helps the antiferromagnetic ground state to persist. This competition between both angle decreasing and bond length shortening therefore makes the antiferromagnetic ordering very robust under pressure. Consequently, the insulating phase persists for high pressure. This explains the low pressure coefficient of the band gap of $NaOsO_3$.

7.3.5 Inter-atomic Heisenberg Exchange Interactions

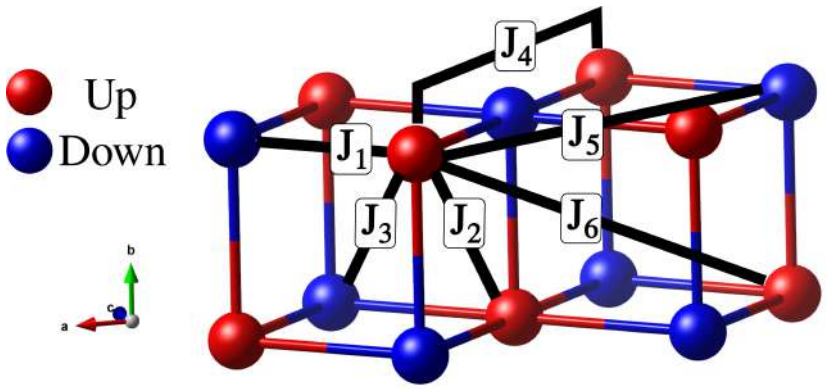

Figure 7.7: Os atoms in the G-AFM spin configuration with different Heisenberg exchange interaction.

To provide the description of the magnetic ordering at high temperature, we have extracted exchange interactions as a function of the pressure. The magnetic Os atoms forms a cubic lattice shown in Fig. 7.7 along with the various neighbor inter atomic exchange interactions. The red and blue spheres respectively denotes the Os atom with up and down spins. The exchange interactions are listed in table 7.2. The variation of first, second, fourth and fifth nearest neighbor exchange interactions as a function of the applied pressure are plotted in Fig. 7.8. All other exchange interactions are found

to be of negligible as shown in table 7.2. The nearest neighbour interaction (J_1) is found to be antiferromagnetic and dominating for all pressure. All exchange interactions are monotonically decreasing except the ferromagnetic fourth neighbor exchange interaction (J_4). It is found to be increasing upto 20 GPa and then decreases upon further increase of pressure.

Pressure(GPa)	J_1	J_2	J_3	J_4	J_5
0	-11.33	0.78	-0.07	1.33	-0.26
10	-11.26	0.56	-0.09	1.55	-0.23
20	-11.02	0.34	-0.09	1.68	-0.20
30	-10.29	0.13	-0.07	1.67	-0.17
40	-8.95	0.07	-0.06	1.44	-0.11

Table 7.2: Exchange interactions extracted from isotropic Heisenberg Hamiltonian

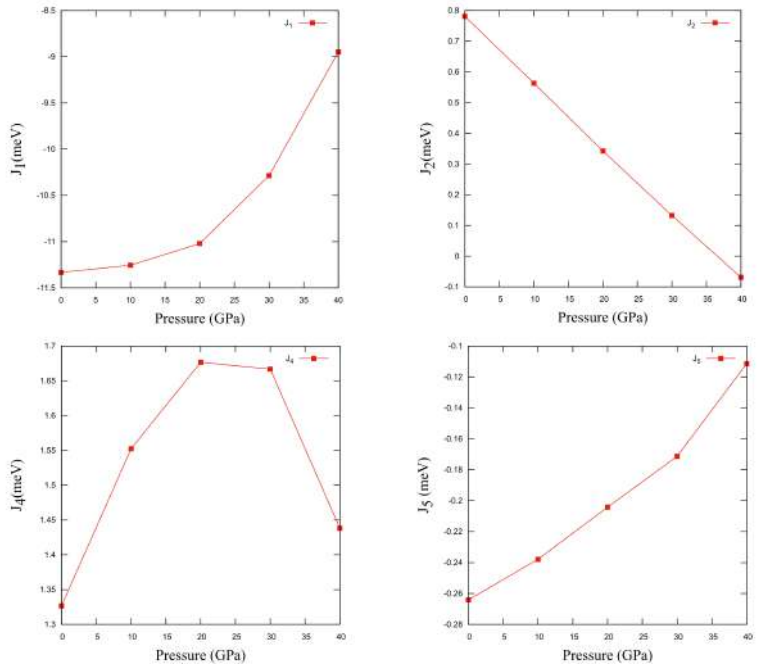

Figure 7.8: Evolution of exchange interactions between between different neighboring Os atoms under pressure.

7.3.6 Evolution of Ordering Temperature With Pressure

The extracted interaction energies are then used as input in Monte Carlo simulation using Metropolis algorithm to determine the Neel temperature at different pressure. The magnetization vs temperature curve is shown in Fig. 7.9a. The Neel temperature at ambient pressure is 460 K. As the pressure is increased the Neel temperature decreases monotonically shown in Fig. 7.9b. At 40 GPa the metallic antiferromagnet has a ordering temperature 310 K.

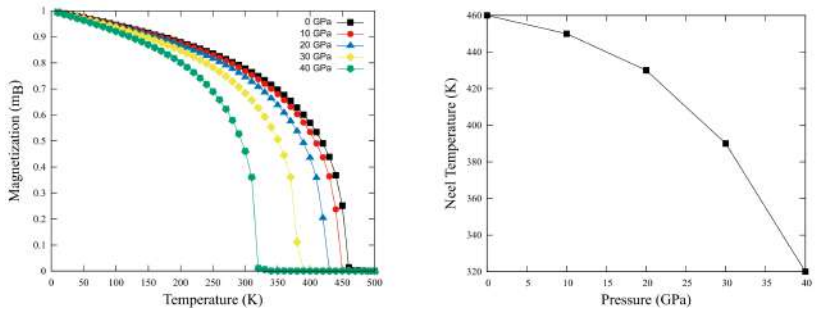

Figure 7.9: (a) Magnetization curve for different applied pressure. (b) Evolution of Neel temperature under pressure.

7.4 Conclusion

We have studied the pressure induced metal insulator transition in $NaOsO_3$. The *ab-initio* results revealed that the transition does not strictly follow Slater mechanism. The density of states shows that the magnetic moment of Os atoms survives deep into the metallic state. Both the band gap and the magnetic moment in this material are robust owing to competition between reduction of Os-O-Os bond angle and Os-O bond length shortening. Using a minimal isotropic Heisenberg model, we have determined the exchange interactions at different pressure and performed a monte-carlo simulation to understand the evolution of magnetism in high temperatures. At 40 GPa,

the antiferromagnetic metallic state has Neel temperature above 310 K.

Bibliography

[1] Y. G. Shi, Y. F. Guo, S. Yu, M. Arai, A. A. Belik, A. Sato, K. Yamaura, E. Takayama-Muromachi, H. F. Tian, H. X. Yang, J. Q. Li, T. Varga, J. F. Mitchell, and S. Okamoto. Continuous metal-insulator transition of the antiferromagnetic perovskite $naoso_3$. *Phys. Rev. B*, 80:161104, Oct 2009.

[2] S. Calder, V. O. Garlea, D. F. McMorrow, M. D. Lumsden, M. B. Stone, J. C. Lang, J.-W. Kim, J. A. Schlueter, Y. G. Shi, K. Yamaura, Y. S. Sun, Y. Tsujimoto, and A. D. Christianson. Magnetically driven metal-insulator transition in $naoso_3$. *Phys. Rev. Lett.*, 108:257209, Jun 2012.

[3] A. Vecchio, I.and Perucchi, Di Pietro P., et al. Magnetically driven metal-insulator transition in $naoso_3$. *Sci. Rep.*, 3:2990, Oct 2013.

[4] J. C. Slater. Magnetic effects and the hartree-fock equation. *Phys. Rev.*, 82:538–541, May 1951.

[5] Bongjae Kim, Peitao Liu, Zeynep Ergönenc, Alessandro Toschi, Sergii Khmelevskyi, and Cesare Franchini. Lifshitz transition driven by spin fluctuations and spin-orbit renormalization in $naoso_3$. *Phys. Rev. B*, 94:241113, Dec 2016.

[6] S. Calder, J. G. Vale, N. Bogdanov, C. Donnerer, D. Pincini, M. Moretti Sala, X. Liu, M. H. Upton, D. Casa, Y. G. Shi, Y. Tsujimoto, K. Yamaura, J. P. Hill, J. van den Brink, D. F. McMorrow, and A. D. Christianson. Strongly gapped spin-wave

excitation in the insulating phase of **naoso$_3$**. *Phys. Rev. B*, 95:020413, Jan 2017.

[7] J. G. Vale, S. Calder, C. Donnerer, D. Pincini, Y. G. Shi, Y. Tsujimoto, K. Yamaura, M. Moretti Sala, J. van den Brink, A. D. Christianson, and D. F. McMorrow. Evolution of the magnetic excitations in naoso$_3$ through its metal-insulator transition. *Phys. Rev. Lett.*, 120:227203, May 2018.

[8] S. Calder, J. Lee, M. Stone, et al. Enhanced spin-phonon-electronic coupling in a 5d oxide. *Nat Commun*, 6:8916, Nov 2015.

[9] P. E. Blöchl. Projector augmented-wave method. *Phys. Rev. B*, 50:17953–17979, Dec 1994.

[10] G. Kresse and D. Joubert. From ultrasoft pseudopotentials to the projector augmented-wave method. *Phys. Rev. B*, 59:1758–1775, Jan 1999.

[11] W. Kohn. Nobel lecture: Electronic structure of matter—wave functions and density functionals. *Rev. Mod. Phys.*, 71:1253–1266, Oct 1999.

[12] G. Kresse and J. Hafner. Ab initio molecular dynamics for liquid metals. *Phys. Rev. B*, 47:558–561, Jan 1993.

[13] G. Kresse and J. Furthmüller. Efficient iterative schemes for ab initio total-energy calculations using a plane-wave basis set. *Phys. Rev. B*, 54:11169–11186, Oct 1996.

[14] G. Kresse and J. Furthmüller. Efficiency of ab-initio total energy calculations for metals and semiconductors using a plane-wave basis set. *Computational Materials Science*, 6(1):15–50, 1996.

[15] John P. Perdew, Kieron Burke, and Matthias Ernzerhof. Generalized gradient approximation made simple. *Phys. Rev. Lett.*, 77:3865–3868, Oct 1996.

[16] S. L. Dudarev, G. A. Botton, S. Y. Savrasov, C. J. Humphreys, and A. P. Sutton. Electron-energy-loss spectra and the structural stability of nickel oxide: An lsda+u study. *Phys. Rev. B*, 57:1505–1509, Jan 1998.

[17] Erik R. Ylvisaker, Warren E. Pickett, and Klaus Koepernik. Anisotropy and magnetism in the LSDA + U method. *Phys. Rev. B*, 79:035103, Jan 2009.

[18] Burak Himmetoglu, Andrea Floris, Stefano de Gironcoli, and Matteo Cococcioni. Hubbard-corrected dft energy functionals: The lda+u description of correlated systems. *International Journal of Quantum Chemistry*, 114(1):14–49, 2014.

[19] Hendrik J. Monkhorst and James D. Pack. Special points for brillouin-zone integrations. *Phys. Rev. B*, 13:5188–5192, Jun 1976.

[20] F. D. Murnaghan. The compressibility of media under extreme pressures. *Proceedings of the National Academy of Sciences*, 30(9):244–247, 1944.

[21] Jie Chen, Jiaming He, Yanyao Zhang, Stella Chariton, Vitali Prakapenka, Kazunari Yamaura, Jung-Fu Lin, J. B. Goodenough, and J.-S. Zhou. *Insitu* structural determination of $3d$ and $5d$ perovskite oxides under high pressure by synchrotron x-ray diffraction. *Phys. Rev. B*, 108:134106, Oct 2023.

[22] I. Loa, P. Adler, A. Grzechnik, K. Syassen, U. Schwarz, M. Hanfland, G. Kh. Rozenberg, P. Gorodetsky, and M. P. Pasternak. Pressure-induced quenching of the jahn-teller distortion

and insulator-to-metal transition in $lamno_3$. *Phys. Rev. Lett.*, 87:125501, Aug 2001.

[23] Mithun Khan, Md. Zahidur Rahaman, and Md. Lokman Ali. Pressure-induced band gap engineering of nontoxic lead-free halide perovskite $csmgi_3$ for optoelectronic applications. *ACS Omega*, 8(28):24942–24951, 2023.

[24] Robin Turnbull, Javier González-Platas, Fernando Rodríguez, Akun Liang, Catalin Popescu, Zhangzhen He, David Santamaría-Pérez, Plácida Rodríguez-Hernández, Alfonso Muñoz, and Daniel Errandonea. Pressure-induced phase transition and band gap decrease in semiconducting β $cu_2v_2o_7$. *Inorganic Chemistry*, 61(8):3697–3707, 2022. PMID: 35157423.

[25] Mauro Coduri, Timothy A. Strobel, Marek Szafrański, Andrzej Katrusiak, Arup Mahata, Federico Cova, Sara Bonomi, Edoardo Mosconi, Filippo De Angelis, and Lorenzo Malavasi. Band gap engineering in $masnbr_3$ and $cssnbr_3$ perovskites: Mechanistic insights through the application of pressure. *The Journal of Physical Chemistry Letters*, 10(23):7398–7405, 2019. PMID: 31721591.

[26] A A Sholagberu, W A Yahya, and A A Adewale. Pressure effects on the opto-electronic and mechanical properties of the double perovskite cs2agincl6. *Physica Scripta*, 97(8):085824, jul 2022.

CHAPTER 8

Unusual Magneto-transport in a Doped Heusler Material

" Instinct is a marvellous thing. It can neither be explained nor ignored"

Agatha Christie

8.1 Introduction

Recently, polycrystalline $Ru_2Fe_{0.6}Mn_{0.4}Ge$ have been synthesized and magnetotransport measurements have been performed [1]. The interest in this class of Heusler materials has increased in recent times after the seminal work on antiferromagnetic spintronics [1, 2], where the active component of spintronic devices are antiferromagnets. In this chapter, theoretical calculations performed on material with similar doping concentration have been discussed. Experimentally, signature of anomalous Hall conductivity and unconventional Hall conductivity has been observed. Significant intrinsic contributions to the anomalous Hall conductivity have been found. By studying the magnetic and electronic ground state, we shall show that the Mn moments are canted with respect to the ferromagnetically arranged Fe moments. Additionally, existence of chiral Weyl node has been found

[1] The results discussed in this chapter is part of a collaborative project with A. Ahmed et al.

around Γ point. Consequently, the system have high Berry curvature and the intrinsic anomalous Hall conductivity becomes finite.

The magnetisation measurement has revealed a bifurcation between the field cooled and zero field cooled sample. This suggests that the doped Mn atoms tend to form anti ferromagnetic clusters within this material. The magnetoresistance of this sample has been found to change sign below the bifurcation temperature. We have studied possible cause for this behaviour by calculating exchange interaction between various type of neighboring atoms.

8.2 Methodology

8.2.1 *ab-initio* Calculations

All *ab-initio* calculation have been performed by a plane-wave projector augmented wave [3, 4] implementation of density functional theory [5] as implemented in VASP [6, 7, 8]. For exchange correlation, PBE functionals [9] have been used. For self consistent calculations a Monkhorst-Pack k-mesh [10] of 12 × 12 × 12 k points have been used. Cutoff energy of 600 eV has been set for the plane-wave basis states. The ion positions have been relaxed till the atomic forces lies below 0.01 eV/Å.

8.2.2 Tight binding fitting

An effective tight binding Hamiltonian for the system was obtained by constructing maximally localized Wannier functions (MLWF) [11, 12] as implemented in WANNIER90 [13]. The basis of the tight binding Hamiltonian consisted of d orbitals of Fe, Mn and Ru and p orbitals of Ge atoms. Spin orbit interactions have been considered

while constructing the Wannier functions. The momentum dependent Berry Curvature and the anomalous Hall conductivity was calculated using the Wannier functions within the WANNIER TOOLS [14] package.

8.3 Results and Discussion

8.3.1 Experimental Observations

The experimental setup for Hall measurements are shown in Fig. 8.1a. The Hall resistivity is shown in Fig. 8.1b for various temperatures. Focusing on the Hall resistivity at low temperatures, signature of anomalous Hall effect and unconventional Hall effect has been found. In Fig. 8.1b these different contributions to the total Hall resistivity at 2K has been shown where ρ_{xy}^{H}, ρ_{xy}^{A}, ρ_{xy}^{N} and ρ_{xy}^{UC} represents total, anomalous, normal and unconventional Hall resistivity.

The Anomalous Hall resistance (ρ_{xy}^{A}) is usually divided into two parts as follows.

$$\rho_{xy}^{A} = a\rho_{xx} + b\rho_{xx}^{2} \tag{8.1}$$

where, the first term in the right indicates the contribution from extrinsic skew scattering and the quadratic term indicates the intrinsic contributions. Both these contributions are shown in Fig. 8.1e as a function of temperature. In Fig. 8.1f, numerical values of the parameters a and b in equation 8.1, has been determined by plotting $\frac{\rho_{xy}^{A}}{\rho_{xx}}$ vs. ρ_{xx}.

Experimentally measured magnetisation curve of the sample is shown in Fig. 8.2a. For low field, bifurcation between magnetisation of zero field cooled sample and field cooled sample has been observed. The ordering temperature, T_c and the bifurcation temperature T_{irr}

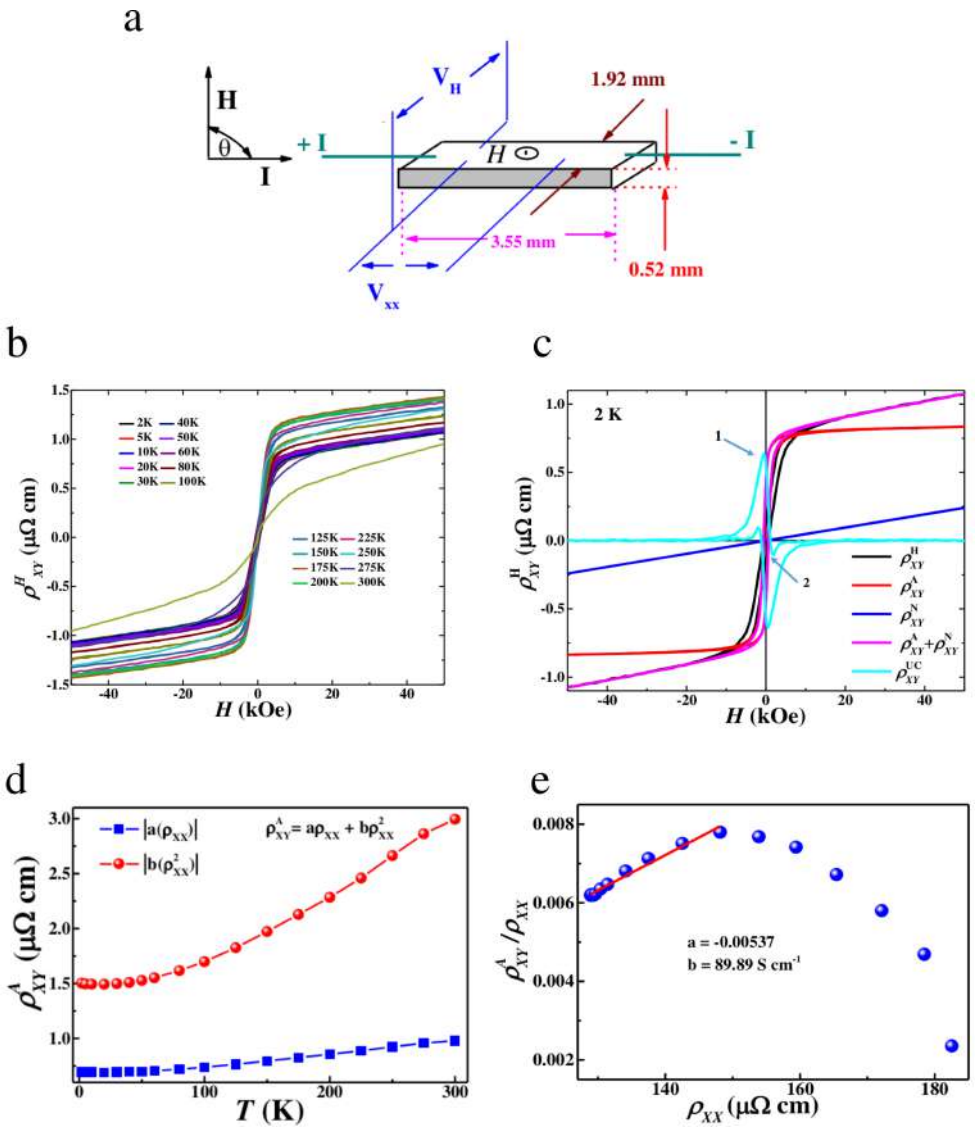

Figure 8.1: (a) Experimental setup for Hall measurements of the sample. (b) Hall resistivity at different temperatures. (c) Different contributions to the total Hall resistivity at low temperatures. (d & e) Extrinsic and intrinsic Anomalous Hall resistivity. [*Reproduced from work of Afsar et. al. with permission*]

are indicated in the plot. Looking at the magnetoresistance data in Fig. 8.2b, one finds that the magnetoresistance curve behaves differently below 150 K. For small external field, the magnetoresistance is

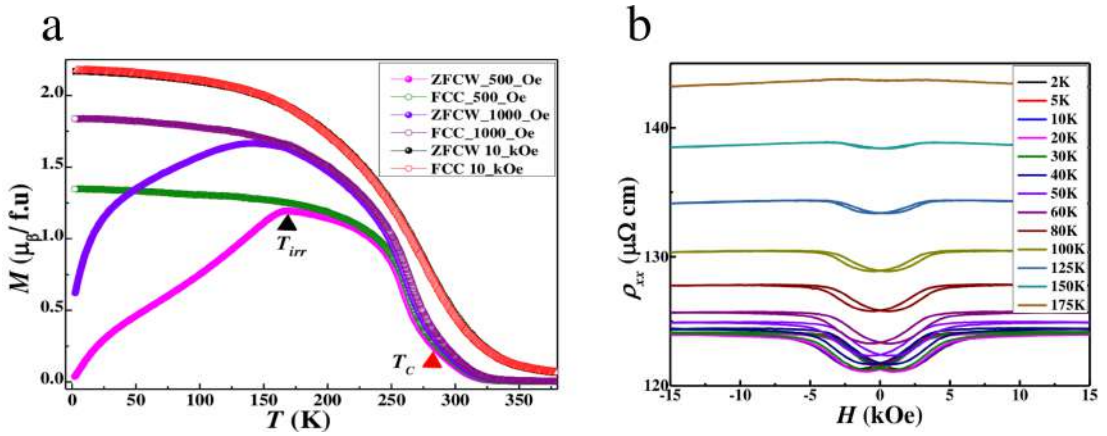

Figure 8.2: (a) Magnetisation curve of the sample at different field strength. (b) Longitudinal magnetoresistance as a function of the applied field for different temperatures. [*Reproduced from work of Ahmed et al. with permission*]

positive below T_{irr} while it is negative above T_{irr}.

8.3.2 Canted Magnetism

In order to explain the observed experimental data we have considered a sample with 50% Mn doping, close to the concentration used in the experiment. As the lattice parameter of both the parent compound Ru_2FeGe and Ru_2MnGe are similar, we have constructed a $2 \times 2 \times 2$ supercell starting with the fcc primitive cell of Ru_2FeGe. The supercell contains 4 Mn and 4 Fe atoms as shown in fig. 8.3a. We then studied the magnetic ground state of the sample.

Previous studies had shown that Ru_2FeGe is a ferromagnet [15] while Ru_2MnGe is an antiferrromagnet [16]. To probe the magnetic ground state in the doped sample $Ru_2Fe_{0.5}Mn_{0.5}Ge$, we have performed magnetic calculations by constraining the direction of the magnetic moments on Mn atoms. As shown in Fig. 8.3a, the moments on the Fe atoms (red arrow) are kept in ferromagnetic arrangement while the moments on the Mn atoms (blue arrow) are rotated

by the canting angle (θ). Canting angle of 0° and 180° correspond to the ferromagnetic and antiferromagnetic ordering respectively. The energy of different magnetic configurations per formula unit are plotted against the canting angle in Fig. 8.3(b). We find that the magnetic configuration with 165° canting angle corresponds to the ground state.

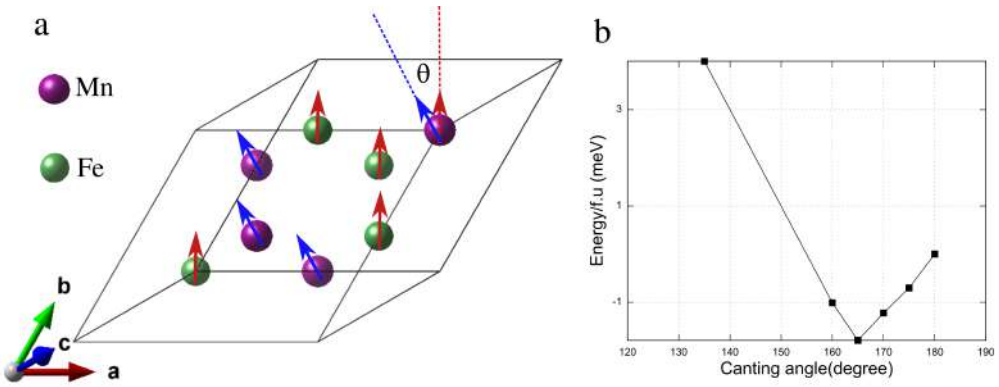

Figure 8.3: (a) Constructed supercell for $Ru_2Fe_{0.5}Mn_{0.5}Ge$ with the magnetic atoms. The arrow on each atom denotes the localised magnetic moment on that atom. The canting angle θ is shown. (b) Total Energy relative to the antiferromagnetic configuration ($\theta = 180$) as a function of the canting angle.

8.3.3 Anomalous Hall Conductivity

The implication of the canted magnetic ground state on the electronic structure is then studied. The electronic band structure shown in Fig.8.4, reveals that the system is metallic with many bands crossing the Fermi energy. Focusing around the Γ point, we find linear band crossings. The chirality of these crossing points have been calculated to be non zero as shown in the inset of Fig.8.4. This indicates that these band crossings are Weyl points. Evidently, these Weyl points are expected to give rise to Berry curvature in the momentum space which contributes to the intrinsic anomalous Hall conductivity. To confirm this, we have obtained a good tight binding fit of the

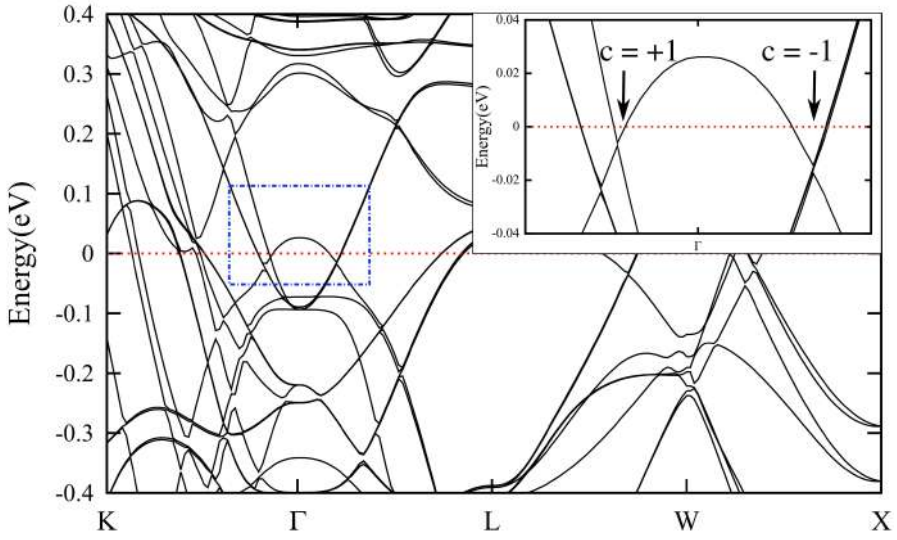

Figure 8.4: The electronic band structure of the canted magnetic configuration along various high symmetry directions. The inset shows Weyl nodes around Γ point.

electronic band structure through Wannier interpolation and calculated the z component of the Berry curvature, $\Omega_z(\boldsymbol{k})$. In Fig. 8.5, calculated Berry curvature is shown on a 2D slice of the Brillouin zone defined by reciprocal lattice vector k_x and k_y.

We then calculated the intrinsic anomalous Hall conductivity given by,

$$\sigma_{xy}^{AHC} = -\int_{BZ} \frac{d^3k}{(2\pi)^3} \sum_{n\in\{Occ.\}} f_n(\boldsymbol{k})\Omega_z(\boldsymbol{k}) \tag{8.2}$$

where, n is the band index, and $f_n(\boldsymbol{k})$ denotes occupancy of n^{th} band. Integrating the calculated Berry curvature, the AHC is at the calculated Fermi energy is found to be 76.47 S/cm. This matches well with the experimentally obtained value of 89.89 S/m as shown in Fig. 8.2 d. The variation of the AHC with the Fermi energy is

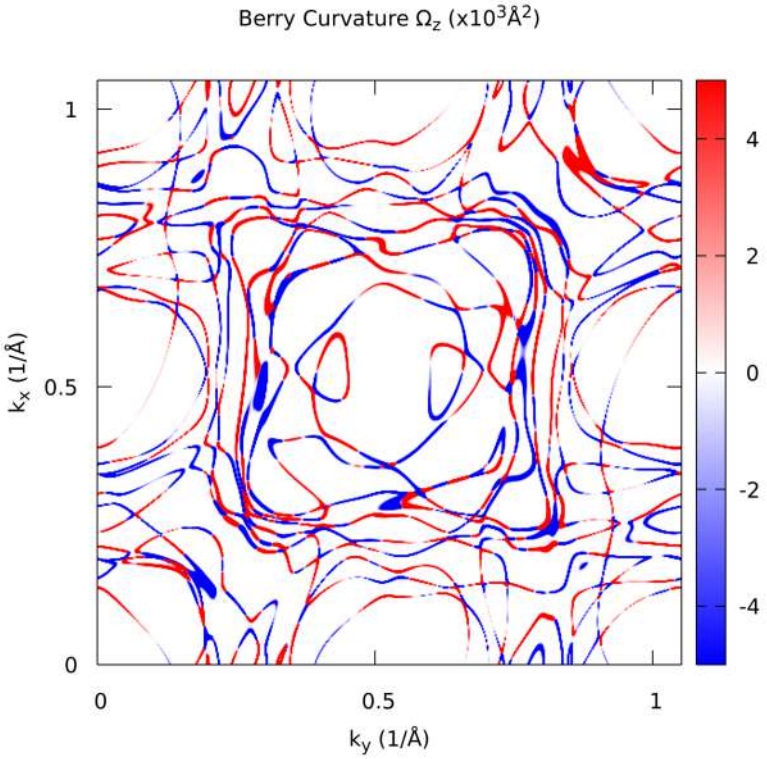

Figure 8.5: z component of Berry curvature(Ω_z) as a function of crystal momentum on a 2d slice of Brillouin zone.

shown in fig. 8.6. The peak left to the Fermi energy correspond to the Weyl nodes around Γ.

8.3.4 Domain Formation and Exchange Interactions

We have considered a homogeneous sample in our theoretical calculations to understand the anomalous Hall effect qualitatively. However, the bifurcating magnetisation curve suggests at formation of domains with different magnetic ordering. Therefore, we have determined whether the doped Mn atoms tend to cluster together. We have calculated total energy of a configuration where 4 Mn atoms occupy the neighboring sites and another configuration with 1 Mn atom in the unit cell. Then the clustering energy is defined as,

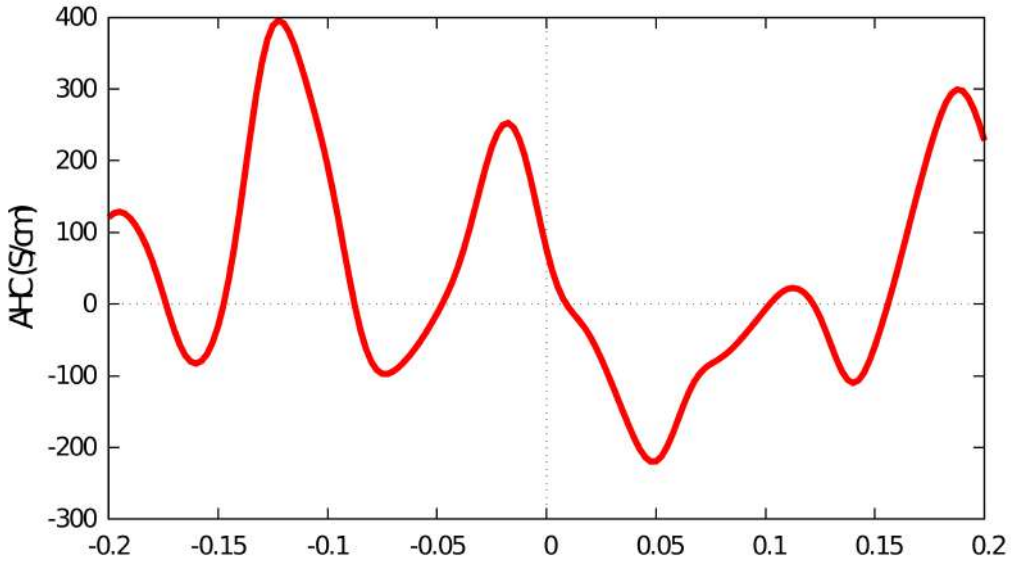

Figure 8.6: Anomalous hall conductivity as a function of Fermi energy of the material.

$E_{clustering} = [E(4Mn) - E(0)] - 4[E(Mn) - E(0)]$, where E(4Mn), E(Mn) and E(0) are respectively the energies of 4, 1 and 0 Mn atoms in the supercell considered. The clustering energy is found to be -25.8 mev/f.u. implying that separated Fe and Mn rich region tend to develop within the doped compound.

We have then calculated the exchange interactions by mapping the total energies of different magnetic configurations onto a isotropic nearest neighbor Heisenberg model,

$$\mathcal{H} = -\frac{1}{2}\sum_{\langle ij \rangle} J_{ij}\hat{e}_i \cdot \hat{e}_j \tag{8.3}$$

Where, $\hat{e}_i$ or $\hat{e}_j$ is the unit vector along the moment at site i or j and J_{ij} is the exchange interactions between them. Calculating total energy of the different collinear magnetic configurations,

we have determined nearest neighbor exchange interactions between different sites to be, $J_{Fe-Fe} = 4.8$ meV, $J_{Mn-Mn} = -5.3$ meV and $J_{Fe-Mn} = -1.78$ meV. The exchange interactions between the neighbouring Fe atoms are found to be ferromagnetic while the exchange interactions between Mn atoms are found to be antiferromagnetic. The exchange interactions between Fe and Mn atoms are found to be antiferromagnetic with a lower magnitude.

The possibility of domain formation and the determined exchange interactions give a possible explanation for the bifurcation of magnetisation and the sign change of magnetoresistance around the bifurcation temperature (T_{irr}) in the low field limit. As the exchange interactions between Fe and Mn is small, the magnetic ordering within the domains starts to get disrupted near the domain boundaries as the temperature is lowered. Consequently, the ZFC magnetisation decreases below T_{irr}. Within molecular field approximations it had been previously shown that, ferromagnetic metals are known to show negative magnetoresistance [17] and antiferromagnetic order corresponds to positive magnetoresistance [18]. As the magnetisation starts to decrease below T_{irr}, the magnetoresistance also becomes positive.

8.3.5 Half Metallicity

The parent compound, Ru_2MnGe is a known half metal. In order to probe if the doped material is also half metal, we have calculated the partial density of states contributed by Fe and Mn states as shown in fig.8.7. In both the panels, the density of states above and below the horizontal line corresponding to zero indicates contributions from majority and minority carriers respectively in the presence of spin orbit coupling. The density of states corresponding to the minority carriers from both Fe and Mn goes to zero at the Fermi energy, shown by vertical blue dashed line. This indicates that only one spin channel

contribute to the transport for the doped material.

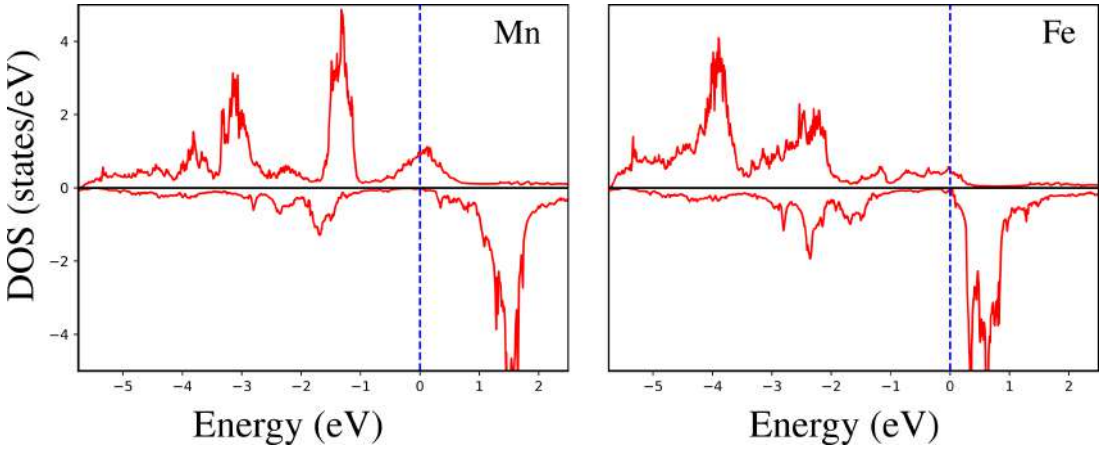

Figure 8.7: Partial density of states of majority(indicated as positive value) and minority(indicated as negative value) carriers of Mn and Fe atoms.

8.4 Conclusion

A doped Heusler compound, $Ru_2Fe_{0.5}Mg_{0.5}Ge$ have been studied to understand recent experimental results on a sample with similar Mn doping concentrations. Considering a homogeneous unit cell, we have studied the magnetic ground state and found a canted magnetic order where the Mn moments are 165° canted with respect to the Fe moments. Within the canted magnetic ground state the electronic band structure has been calculated. Weyl nodes have been found near the Fermi energy. We have then calculated the Berry curvature of the material and use it to calculate the anomalous Hall conductivity. Our calculated anomalous Hall conductivity of 76 S/cm is in good agreement with experimental results on a sample with similar doping concentration. The magnetisation curve shows bifurcation between field cooled and zero field cooled samples at small external field. Additionally, magneto-transport experiments had revealed

that the magnetoresistence shows inverted behaviour below the bifurcation temperature. Our calculation of the clustering energy shows that the real sample is not homogeneous, rather it is favorable to have Mn and Fe rich domains. The exchange interactions between Fe-Fe, Fe-Mn and Mn-Mn have been determined within a Heisenberg model. Our analysis suggests that the inverted magnetoresistance in low temperatures possibly originate from the frustration in the vicinity of domain boundaries.

Bibliography

[1] T. Jungwirth, X. Marti, P Wadley, et al. Antiferromagnetic spintronics. *Nature Nanotech*, 11:231–241, 2016.

[2] Jan Balluff, Teodor Huminiuc, Markus Meinert, Atsufumi Hirohata, and Günter Reiss. Integration of antiferromagnetic Heusler compound Ru2MnGe into spintronic devices. *Applied Physics Letters*, 111(3):032406, 07 2017.

[3] P. E. Blöchl. Projector augmented-wave method. *Phys. Rev. B*, 50:17953–17979, Dec 1994.

[4] G. Kresse and D. Joubert. From ultrasoft pseudopotentials to the projector augmented-wave method. *Phys. Rev. B*, 59:1758–1775, Jan 1999.

[5] W. Kohn. Nobel lecture: Electronic structure of matter—wave functions and density functionals. *Rev. Mod. Phys.*, 71:1253–1266, Oct 1999.

[6] G. Kresse and J. Hafner. Ab initio molecular dynamics for liquid metals. *Phys. Rev. B*, 47:558–561, Jan 1993.

[7] G. Kresse and J. Furthmüller. Efficient iterative schemes for ab initio total-energy calculations using a plane-wave basis set. *Phys. Rev. B*, 54:11169–11186, Oct 1996.

[8] G. Kresse and J. Furthmüller. Efficiency of ab-initio total energy calculations for metals and semiconductors using a plane-wave basis set. *Computational Materials Science*, 6(1):15–50, 1996.

[9] John P. Perdew, Kieron Burke, and Matthias Ernzerhof. Generalized gradient approximation made simple. *Phys. Rev. Lett.*, 77:3865–3868, Oct 1996.

[10] Hendrik J. Monkhorst and James D. Pack. Special points for brillouin-zone integrations. *Phys. Rev. B*, 13:5188–5192, Jun 1976.

[11] Nicola Marzari and David Vanderbilt. Maximally localized generalized wannier functions for composite energy bands. *Phys. Rev. B*, 56:12847–12865, Nov 1997.

[12] Ivo Souza, Nicola Marzari, and David Vanderbilt. Maximally localized wannier functions for entangled energy bands. *Phys. Rev. B*, 65:035109, Dec 2001.

[13] Arash A. Mostofi, Jonathan R. Yates, Giovanni Pizzi, Young-Su Lee, Ivo Souza, David Vanderbilt, and Nicola Marzari. An updated version of wannier90: A tool for obtaining maximally-localised wannier functions. *Computer Physics Communications*, 185(8):2309–2310, 2014.

[14] QuanSheng Wu, ShengNan Zhang, Hai-Feng Song, Matthias Troyer, and Alexey A. Soluyanov. Wanniertools: An open-source software package for novel topological materials. *Computer Physics Communications*, 224:405–416, 2018.

[15] Bhargab Deka, Rahul Das, and A. Srinivasan. Magnetic properties of ge substituted ru2fesi alloys. *Journal of Magnetism and Magnetic Materials*, 347:101–104, 2013.

[16] M. Gotoh, M. Ohashi, T. Kanomata, and Y. Yamaguchi. Spin reorientation in the new heusler alloys ru2mnsb and ru2mnge. *Physica B: Condensed Matter*, 213-214:306–308, 1995.

[17] Hiroshi Yamada and Satoshi Takada. Negative Magnetoresistance of Ferromagnetic Metals due to Spin Fluctuations. *Progress of Theoretical Physics*, 48(6):1828–1848, 12 1972.

[18] Hiroshi Yamada and Satoshi Takada. Magnetoresistance due to Electron-Spin Scattering in Antiferromagnetic Metals at Low Temperatures. *Progress of Theoretical Physics*, 49(5):1401–1419, 05 1973.

Part V

Conclusion and Outlook

CHAPTER 9

Conclusion and Outlook

"The end is where we start from"
T.S. Eliot

9.1 Summary

In this thesis, the crucial role of crystal structure in determining topologically nontrivial or magnetically ordered ground state has been investigated. We have studied various systems ranging from atomically thin 2D materials to layered quasi 2D materials to 3d perovskite oxide and Heusler compounds. The specific role of crystal structure in determining the electronic structure and magnetic ground state has been identified by performing ab-initio calculations and employing different model Hamiltonian methods. The relation between structural transitions in these systems with their different electronic, topological and magnetic ground states have been understood successfully. The key findings for various systems are discussed below.

The trivial and topological insulating phase in 2D materials have been investigated by studying the monolayer of Mo and W based

transition metal dichalcogenides (TMDCs) in different structural configurations. The most stable hexagonal polymorph (1H) is a direct bandgap semiconductor with a bandgap of 1.76 eV as found in DFT calculations using GGA approximation. Moreover, the orbital character of valence band maximum and conduction band minimum at Γ and K point reverses. This is puzzling as the gap between conduction and valence band is found to be quite large everywhere. We have shown that a tight binding model constructed with only d bands, as have been employed in previous studies [1, 2], fails to correctly describe the insulating gap everywhere in the Brillouin zone. We have identified two possible pathways for the d electrons of adjacent metal atoms to interact, one is direct hopping between d states of metal atoms and another is indirect hopping via the chalcogen p states. Including the in-plane p orbitals of the chalcogen we have successfully constructed a minimal tight binding Hamiltonian with 7 basis states that captures both the band gap everywhere in the Brillouin zone and the orbital character reversal at Γ and K and thus providing a better understanding of the low energy excitation in these systems.

We have then studied the 1T and 1T' polymorph of these monolayer TMDCs. The 1T polymoprh is found to be metallic and unstable. Since the bond length between metal and chalcogen has been found to be similar in 1H and 1T polymorph, the change in electronic properties arise from the different crystal field effects arises from different chalcogen environments in these polymorphs. In the 1T phase, octahedral crystal field effects makes the t_{2g} orbitals partially filled and thereby makes this polymorph a metal. We have also found that the inverted bandgap between chalcogen p states and transition metal d states at Γ is present in both 1H and 1T polymorph. The orbital energy difference $\Delta = \epsilon_d - \epsilon_p$ is shown to acquire a k dependence due to significant interactions between adjacent transition metals as well

as interactions between neighboring chalcogen atoms. Consequently, Δ becomes effectively negative at Γ making the inverted bandgap possible. However, the 1H structure has band extrema at K point and therefore the inverted gap at Γ does not make it a suitable candidate for QSH insulator. The 1T phase is also not a topological insulator due to several other trivial bands crossing the Fermi energy across the Brillouin zone.

The origin of the structural instability in 1T polymorph has been understood by analysing the band dispersions near Fermi energy. The in-plane d states have been found to have marginal dispersional width along the Γ-K direction. Our analysis shows that the two possible pathways of hopping of d electrons compete with each other leading to the smaller bandwidth. Consequently, the system distorts by forming dimers between metal atom enhancing the direct hopping of d electrons between adjacent transition metals. Studying the distorted phase, namely 1T', we have shown that the enhanced interaction between d electrons resulting from the dimer formation opens up a gap everywhere in the Brillouin zone except for a small portion in the vicinity of the Γ point. The structural distortions also produce linear sulfur chains, isolated from the transition metals ions. These isolated sulfur chains have been found to contribute to the CBM at Γ. The interactions between p orbitals of these isolated chalcogen chains have shown to be determining the QSH insulating phase in 1T' TMDCs by systematically reducing the $p-p$ interactions within the fitted tight binding model.

Moving onto quasi 2D material $LaAgSb_2$, we have examined the electronic and topological properties at high and low temperatures. In addition to the multiple Dirac cones near the Fermi energy, this material is also known to host two different charge density waves

(CDW), one at 210 K along a direction and another along c direction at 186 K. Although both the CDW states are incommensurate, the second CDW undergoes a transition at 164 K to a commensurate state with a periodicity of 6 unit cells along the c direction. The structure has been optimized within first-principle calculations and an unusual chiral metallic phase have been found at low temperatures. This is because as the temperature is lowered, the electrons on the Ag atoms get more localized, leading to stronger repulsion between electrons associated with atoms on different layers. This leads to successive layers sliding with respect to each other, thereby stabilising a chiral structure in which inversion symmetry is also broken. The large Berry curvature associated with the low temperature structure explains the low temperature planar hall signal in this material. At high temperatures the planar hall signal arises from the anisotropic response of the Dirac cones in the presence of an in-plane magnetic field. These different mechanism at play in high and low temperatures have been found to cause the sign reversal of the planar hall amplitude around the CDW transitions.

In Slater insulators, the insulating state appears when long range antiferromagnetic ordering sets in [3]. A smaller onsite Coulomb interaction strength as well as weaker electron-phonon effects, makes $NaOsO_3$ a rare example of a Slater insulator[4, 5]. $NaOsO_3$ is known to be an insulator with a small band gap of 0.1 eV [6], favoring a G-type antiferromagnetic state below 410 K. The reason for such an unusually high ordering temperature for a $5d$ oxide has been previously traced to the half filling of the t_{2g} bands[7]. In our study, we have examined the pressure dependence of the electronic structure, as well its evolution under pressure both in the presence and absence of spin-orbit interactions within ab-initio electronic structure calculations. The pressure coefficient of the band gap has been

found to be unusually small. This is because of the robustness of the antiferromagnetic ordering under pressure. The structural parameters at various pressure have been analysed and it is found that the competition between Os-O bond length shortening and Os-O-Os angle reducing is responsible for the sluggish suppression of the superexchange. Consequently, we have found an unusual metallic antiferromagnet at half filling under high pressure. We have also determined the magnetic exchange interactions by mapping the energies onto a Heisenberg Model. Using these parameters, the Neel temperature had been calculated for different pressures and we have found that the metallic antiferromagnet at 40 GPa pressure still has high ordering temperatures.

Unusual magneto transport properties in a doped Heusler compound, $Ru_2Fe_xMg_{1-x}Ge$, specifically focusing on the material with $x = 0.5$ have also been investigated. Weyl nodes have been found to exit in the electronic band structure near the Fermi energy. Moreover, broken time reversal symmetry also suggested possibility of anomalous Hall conductivity in this material. Our calculations have predicted an intrinsic anomalous Hall conductivity of 76 S/cm for the mentioned doping level, which is in excellent agreement with experimental results. Further, for this specific doping ($x = 0.5$), a canted antiferromagnetic structure with a canting angle of 165° was identified as the ground state magnetic configuration. Additionally, magneto-transport experiments had revealed that the magnetoresistence show inverted behaviour below 175 K. Our calculation of the clustering energy shows that Mn cluster formation is favoured within the system suggesting existence of isolated Fe and Mn rich domains within the material. The exchange interaction between Fe-Fe, Fe-Mn and Mn-Mn has been determined within a Heisenberg model. Our analysis suggested that the inverted magnetoresistance in low temperatures

originate from the domain switching in this material.

9.2 Outlook and Future Steps

While enriching the understanding of how different exotic topological and magnetic ground states are related with the crystal structure, the work carried out in this thesis has also paved way for many interesting ideas to be investigated in future works both in the domain of the theoretical and experimental material science.

For example, as we have successfully found a minimal model within realistic physical limits for low energy bands in hexagonal TMDCs, (see chapter 3). It would be interesting to employ this minimal tight-binding model in order to study orbital physics in these materials, an emerging field that may provide promising results for futuristic electronics devices.

The chiral metallic structure we have found as the CDW modulated structure for $LaAgSb_2$ (see chapter 5) could provide another platform to study orbital angular momentum physics. Generally, in bulk solids orbital degrees of freedom get quenched. However, due to the chirality of the crystal structure at low temperatures, the local environment to different atoms changes in successive layers making finite orbital angular momentum plausible in this material.

In chapter 7 while studying the robust antiferromagnetic ordering of $NaOsO_3$ under pressure, we have found that at high pressure one have a metallic antiferromagnet which is unusual at the half filling limit of the t_{2g} orbitals. Since our calculation have also found that the ordering temperature is above room temperature, this metallic antiferromagnetic state could have great potential for experimental

studies, spintronics, magnetic spin valve devices and tunnel junction based devices.

Bibliography

[1] Gui-Bin Liu et al. Three-band tight-binding model for monolayers of group-vib transition metal dichalcogenides. *Phys. Rev. B*, 88:085433, Aug 2013.

[2] Sayantika Bhowal and S. Satpathy. Intrinsic orbital moment and prediction of a large orbital hall effect in two-dimensional transition metal dichalcogenides. *Phys. Rev. B*, 101:121112, Mar 2020.

[3] J. C. Slater. Magnetic effects and the hartree-fock equation. *Phys. Rev.*, 82:538–541, May 1951.

[4] Y. G. Shi, Y. F. Guo, S. Yu, M. Arai, A. A. Belik, A. Sato, K. Yamaura, E. Takayama-Muromachi, H. F. Tian, H. X. Yang, J. Q. Li, T. Varga, J. F. Mitchell, and S. Okamoto. Continuous metal-insulator transition of the antiferromagnetic perovskite $naoso_3$. *Phys. Rev. B*, 80:161104, Oct 2009.

[5] S. Calder, V. O. Garlea, D. F. McMorrow, M. D. Lumsden, M. B. Stone, J. C. Lang, J.-W. Kim, J. A. Schlueter, Y. G. Shi, K. Yamaura, Y. S. Sun, Y. Tsujimoto, and A. D. Christianson. Magnetically driven metal-insulator transition in $naoso_3$. *Phys. Rev. Lett.*, 108:257209, Jun 2012.

[6] A. Vecchio, I.and Perucchi, Di Pietro P., et al. Magnetically driven metal-insulator transition in $naoso_3$. *Sci. Rep.*, 3:2990, Oct 2013.

[7] S. Middey et al. $NaOso_3$: A high neel temperature $5d$ oxide. *Phys. Rev. B*, 89:134416, Apr 2014.

Part VI

Appendices

APPENDIX A

Tight Binding Hamiltonian Matrix of Monolayer 1H MoS_2

The tight binding Hamiltonian have been constructed for monolayer 1H MoS_2 with the unit cell defined by the in-plane lattice vectors given by,

$$\begin{aligned} \vec{a}_1 &= a\hat{i} \\ \vec{a}_2 &= -\frac{a}{2}\hat{i} + \frac{\sqrt{3}a}{2}\hat{i} \end{aligned} \tag{A.1}$$

where, a is the lattice parameter having an experimental value of 3.16Å. The unit cell contains one Mo and two S atoms. The position of the Mo atom is considered to be the origin of the coordinate system. The position vectors of the sulfur atoms belonging to the top and bottom layer are,

$$\begin{aligned} \vec{R}_{S_{top}} &= \frac{\sqrt{3}d}{2}\cos\theta\hat{i} + \frac{d}{2}\cos\theta\hat{i} + d\sin\theta\hat{k} \\ \vec{R}_{S_{top}} &= \frac{\sqrt{3}d}{2}\cos\theta\hat{i} + \frac{d}{2}\cos\theta\hat{i} - d\sin\theta\hat{k} \end{aligned} \tag{A.2}$$

where, $d = 2.41$ Å is the nearest neighbor Mo-S distance and $\theta = 40.76°$ is the angle made by the Mo-S bond with the central Mo plane. In the following we first construct the tight binding Hamiltonian considering only d orbitals of Mo atom in the basis and then include the p_x and p_y orbitals of Sulfur atoms.

A.1 d-only model

The basis is taken to be $\{d_{xy}, d_{x^2-y^2}, d_{z^2}\}$. The k dependent Hamiltonian is given by,

$$H_{ij}(\boldsymbol{k}) = \sum_{\boldsymbol{R}} e^{i\boldsymbol{k}\cdot\boldsymbol{R}} E_{ij}(\boldsymbol{R}) \tag{A.3}$$

Where, $E_{ij}(\boldsymbol{R}) = \langle i(\boldsymbol{r})|\hat{H}|j(\boldsymbol{r}-\boldsymbol{R})\rangle$ is the hopping energy between basis $|i\rangle$ at home unit cell and $|j\rangle$ at lattice vector $\boldsymbol{R}$. These hopping energy term can be written in terms of the two-centre bond integrals following the formulation of Slater and Koster.

Atom number	Lattice vector	Direction cosine (l,m,n)
1	$\boldsymbol{R_1} = \langle a, 0, 0\rangle$	$(1, 0, 0)$
2	$\boldsymbol{R_2} = \langle \frac{a}{2}, \frac{\sqrt{3}a}{2}, 0\rangle$	$(\frac{1}{2}, \frac{\sqrt{3}}{2}, 0)$
3	$\boldsymbol{R_3} = \langle -\frac{a}{2}, \frac{\sqrt{3}a}{2}, 0\rangle$	$(-\frac{1}{2}, \frac{\sqrt{3}}{2}, 0)$
4	$\boldsymbol{R_4} = \langle -a, 0, 0\rangle$	$(-1, 0, 0)$
5	$\boldsymbol{R_5} = \langle -\frac{a}{2}, -\frac{\sqrt{3}a}{2}, 0\rangle$	$(-\frac{1}{2}, -\frac{\sqrt{3}}{2}, 0)$
6	$\boldsymbol{R_6} = \langle \frac{a}{2}, -\frac{\sqrt{3}a}{2}, 0\rangle$	$(\frac{1}{2}, -\frac{\sqrt{3}}{2}, 0)$

Table A.1: Lattice vector corresponding to the neighboring Mo atoms shown in Fig. 3.3

.

Restricting the sum to the first neighbor Mo atoms to the central Mo atom in the home unit cell, The 3×3 Hamiltonian matrix elements can be calculated explicitly using the direction cosines of the neighboring atoms listed in table A.1 . Since, neighboring Mo network possess inversion symmetry implying, $E_{ij}(-\boldsymbol{R}) = E_{ij}(\boldsymbol{R})$ all the Hamiltonian matrix elements within d-only model in equation (3.1) are real for all $\boldsymbol{k}$. Therefore, the 3×3 Hamiltonian matrix has

six independent matrix elements.

$$h_{dd}(\boldsymbol{k}) = \begin{pmatrix} h_{11} & h_{12} & h_{13} \\ h_{12} & h_{22} & h_{23} \\ h_{13} & h_{23} & h_{33} \end{pmatrix} \tag{A.4}$$

The matrix elements are given as,

$$\begin{aligned}
h_{11} =& 2V_{dd\pi}\cos 2\alpha + \Big(\frac{9}{4}V_{dd\sigma} + V_{dd\pi} + \frac{3}{4}V_{dd\delta}\Big)\cos\alpha\cos\beta + \epsilon_1 \\
h_{12} =& \Big(\frac{3\sqrt{3}}{4}V_{dd\sigma} - \sqrt{3}V_{dd\pi} + \frac{\sqrt{3}}{4}V_{dd\delta}\Big)\sin\alpha\sin\beta \\
h_{13} =& \Big(\frac{3}{2}V_{dd\sigma} - \frac{\sqrt{3}}{2}V_{dd\delta}\Big)\sin\alpha\sin\beta \\
h_{22} =& \Big(\frac{3}{2}V_{dd\sigma} + \frac{1}{2}V_{dd\delta}\Big)\cos 2\alpha + \\
& \Big(\frac{3}{4}V_{dd\sigma} + 3V_{dd\pi} + \frac{1}{4}V_{dd\delta}\Big)\cos\alpha\cos\beta + \epsilon_1 \\
h_{23} =& \Big(-\frac{\sqrt{3}}{2}V_{dd\sigma} + \frac{\sqrt{3}}{2}V_{dd\delta}\Big)\Big[\cos 2\alpha - \cos\alpha\cos\beta\Big] \\
h_{33} =& \Big(V_{dd\sigma} + 3V_{dd\delta}\Big)\Big[\cos 2\alpha + \cos\alpha\cos\beta\Big] + \epsilon_2
\end{aligned} \tag{A.5}$$

where $\alpha = ak_x$ and $\beta = a\sqrt{3}k_y$. The Slater Koster parameters are $V_{dd\sigma}, V_{dd\pi}$ and $V_{dd\delta}$ and the orbital energies are ϵ_1 for d_{xy} and $d_{x^2-y^2}$ and ϵ_2 for d_{z^2}. As the basis states are orthogonal, the overlap matrix is not required to be calculated.

A.2 7 Band TB Model With S p States

The p_x and p_y orbitals of sulfur atoms have been added to the basis. Therefore the basis now becomes $\{d_{xy}, d_{x^2-y^2}, d_{z^2}, p_x^t, p_y^t, p_x^b, p_y^b\}$. The superscript t and b indicates that the orbital belongs to the Sulfur atom in the top and bottom layer respectively. The 7×7 Hamiltonian can be divided as,

$$\mathcal{H}_{7\text{-band}} = \begin{pmatrix} h_{dd} & h_{dp} \\ h_{dp}^{*} & h_{pp} \end{pmatrix} \tag{A.6}$$

where, h_{dd} is the 3×3 block as defined in the previous section. h_{dp} is the 3×4 block describing hopping between $Mo - d$ orbitals and $S - p$ orbitals and h_{pp} is the 4×4 block describing the interactions between p orbitals of neighboring Sulfur atoms.